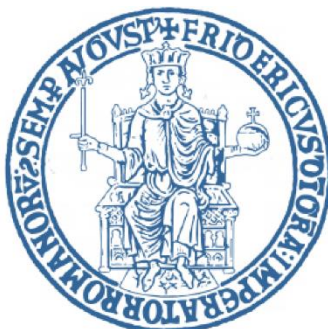


**Università degli Studi di Napoli Federico II**



## **Interactive Biohybrid Synapses**

**Ph.D. Program in Industrial product and Process Engineering  
XXXIV - cycle**

**Claudia Lubrano, M. Sc.**

**Supervisor:** Prof. Francesca Santoro

**Tutor:** Prof. Paolo Antonio Netti

**Coordinator:** Prof. Andrea D'Anna

*To Vincenzo and Sara, my brother and sister,  
because family is where your heart is,  
and no matter how far we live,  
my heart will always be with you*

## Table of contents

<b>List of Figures.....</b>	<b>3</b>
<b>List of Tables .....</b>	<b>5</b>
<b>List of Abbreviations .....</b>	<b>7</b>
<b>Chapter 1: Introduction. ....</b>	<b>11</b>
1.1 The nervous system.....	11
1.2 Neurodegeneration and aging. ....	12
1.2.1 Alzheimer’s disease. ....	13
1.2.2 Parkinson’s disease. ....	13
1.2.3 Multiple sclerosis. ....	13
1.3 Pathophysiological mechanisms underlying neurodegeneration. ....	15
1.3.1 Synapse structure and action potentials propagation. ....	15
1.3.1.1 Neurotransmitters and post-synaptic receptors. ....	18
1.3.2 Synaptic dysfunction in neurodegeneration .....	19
1.3.3 Cell membrane role in neurodegeneration .....	22
1.4 Biomimetic approaches in neuronal-chip coupling.....	25
1.4.1 Conductive polymers. ....	25
1.4.2 Functional biomembranes. ....	29
1.4.3 Mimicking the synapse architecture to enhance cell-chip coupling.....	34
1.5 Neuromorphic devices to mimic electrical neuronal functionalities.....	37
1.5.1 Two-terminal neuromorphic devices. ....	37
1.5.2 Three-terminal neuromorphic devices. ....	39
1.5.3 Towards biohybrid neurointerfaces.....	43
1.6 Our study.....	45
<b>Chapter 2: Materials and Methods. ....</b>	<b>46</b>
2.1 Fabrication of the artificial synapse for the dopamine-mediated biohybrid interface. ....	46
2.2 Fabrication of the artificial synapse for the lipid bilayer- based biomimetic platform. ....	48
2.3 Electrical characterization of the organic neuromorphic device.....	49
2.4 Calibration with dopamine of the artificial post-synaptic device.....	50
2.4.1 Characterization of the electrochemical oxidation of dopamine.....	50
2.4.2 Investigation of the dopamine-mediated neuromorphic behavior.....	50
2.5 Characterization of the cell-material interface in the dopamine-mediated biohybrid synapse. ....	51

2.5.1	Preparation of PEDOT:PSS films as control substrate for cell culture.....	51
2.5.2	Substrate sterilization and coating for cell culture.....	51
2.6	Cell culture.....	52
2.7	Biocompatibility assay.....	53
2.8	Immunohistochemistry.....	54
2.9	Ultra-thin resin embedding procedure for SEM and SEM/FIB.....	56
2.10	Focused ion beam sectioning/scanning electron microscopy of cross sections.....	58
2.11	Dopamine detection measurements with PC-12 cells.....	60
2.12	Supported lipid bilayer assembly and characterization.....	61
2.12.1	Lipids vesicles preparation.....	61
2.12.2	Lipid bilayer formation.....	61
2.12.3	SLB characterization with fluorescence recovery after photobleaching.....	62
2.12.4	SLB characterization with atomic force microscopy.....	64
2.13	Frequency response characterization of the lipid bilayer-based biomimetic synapse.....	66
2.14	Image processing and data analysis.....	68
2.14.1	Live/dead cell populations analysis.....	68
2.14.2	Data processing and analysis.....	68
<b>Chapter 3:</b>	<b>Results and discussion.....</b>	<b>70</b>
3.1	Engineering a dopamine-mediated biohybrid synapse.....	70
3.1.1	Characterization of the organic neuromorphic device artificial synapse.....	70
3.1.2	Characterization of the electrochemical oxidation of dopamine.....	71
3.1.3	Calibration of the organic neuromorphic device with increasing dopamine concentration (steady-state measurements.....)	72
3.1.4	Dopamine-mediated synaptic plasticity.....	74
3.1.5	Characterization of PC-12 cells-OECT interface.....	75
3.1.6	Detection of dopamine release from PC-12 cells.....	77
3.1.7	Dynamic response of the biohybrid synapse.....	80
3.1.8	Characterization of the lower limit response of the biohybrid synapse.....	81
3.2	Engineering a lipid bilayer-based biomimetic synapse.....	84
3.2.1	Investigation of the gate role on OECT short-term potentiation.....	84
3.2.2	Investigation of pulse delays to enhance short-term potentiation.....	87
3.2.3	Formation and characterization of the supported lipid bilayer.....	89
3.2.4	Investigation of the gate role on the short-term potentiation in the biomimetic synapse.....	93
3.2.5	Frequency response characterization of the biomimetic synapse.....	95
3.2.6	Investigation of pulse delays to enhance short-term potentiation in the biomimetic synapse.....	97

<b>Chapter 4: Conclusions.</b> .....	<b>101</b>
<b>References</b> .....	<b>104</b>
<b>List of Publications</b> .....	<b>117</b>
<b>Annex A</b> .....	<b>118</b>
<b>Annex B</b> .....	<b>119</b>
<b><u>Annex C</u></b> .....	<b>121</b>
<b><u>Annex D</u></b> .....	<b>123</b>
<b><u>Annex E</u></b> .....	<b>127</b>
<b><u>Annex F</u></b> .....	<b>131</b>
<b>Acknowledgements</b> .....	<b>134</b>

## List of Figures

**Figure 1.1.** Neuronal structure.

**Figure 1.2.** Signal propagation in biological synapses.

**Figure 1.3.** Dendritic spines morphology.

**Figure 1.4.** Neurotransmitter receptors.

**Figure 1.5.** Synaptic plasticity.

**Figure 1.6.** Neuronal cell membrane composition.

**Figure 1.7.** CP-based bioelectronic platforms.

**Figure 1.8.** Conductive polymers-based biosensors.

**Figure 1.9.** Chemical functionalization strategies of conductive polymers.

**Figure 1.10.** Supported lipid bilayers formation strategies.

**Figure 1.7.** Biomembrane-based OECT.

**Figure 1.8.** Dendritic spines-inspired 3D structures.

**Figure 1.9.** Conductive polymer-based 3D electrodes.

**Figure 1.10.** Synaptic plasticity in organic memristors.

**Figure 1.11.** Short-term plasticity in PEDOT:PSS-based OECT.

**Figure 1.12.** Long-term plasticity in PEDOT:PSS-based OECT.

**Figure 1.13.** Hybrid neuronal networks.

**Figure 2.1.** OECT architecture for the biohybrid synapse.

**Figure 2.2.** OECT architecture for the biomimetic synapse.

**Figure 2.3.** Live/dead cells labelling.

**Figure 2.4.** Exemplary images of PC-12 cells immunohistochemistry.

**Figure 2.5.** Ultra-thin plasticization method.

**Figure 2.6.** FIB/SEM cross-sectioning and imaging procedure.

**Figure 2.7.** FRAP images and data analysis.

**Figure 2.8.** AFM images analysis.

**Figure 2.9.** Frequency response analysis and measurement setup.

**Figure 2.10.** Live/dead image analysis.

**Figure 3.1.** Characterization of the organic neuromorphic device.

**Figure 3.2.** Characterization of dopamine electrochemical oxidation.

**Figure 3.3.** Calibration of the OECT response varying dopamine concentration.

**Figure 3.4.** Dopamine-mediated synaptic plasticity in artificial synapse.

**Figure 3.5.** Characterization of the biohybrid interface.

**Figure 3.6.** Dopamine-mediated plasticity in the biohybrid synapse.

**Figure 3.7.** Long-term stability of the biohybrid synapse.

**Figure 3.8.** Dynamic response of the biohybrid synapse.

**Figure 3.9.** Lower limit response of the biohybrid synapse.

**Figure 3.10.** Short-term potentiation of planar and top-gate unfunctionalized OECT.

**Figure 3.11.** Gate current integration.

**Figure 3.12.** Ionic charge analysis in the unfunctionalized OECT.

**Figure 3.13.** Electrical modelling and time response of the unfunctionalized OECT.

**Figure 3.14.** Short-term potentiation of the unfunctionalized OECT in response to gate voltage pulses with  $\Delta t$  set as multiple values of  $\tau_{\text{OECT}}$ .

**Figure 3.15.** FRAP characterization of POPC SLB on OECT surface.

**Figure 3.16.** AFM characterization of POPC SLB on OECT surface.

**Figure 3.17.** Schematics of biomimetic synapse configurations.

**Figure 3.18.** Short-term potentiation for planar and top-gate biomimetic synapse.

**Figure 3.19.** Ionic charge analysis in the biomimetic synapse.

**Figure 3.20.** Frequency response characterization of the biomembrane-based OECT.

**Figure 3.21.** Time response of the biomimetic synapse.

**Figure 3.22.** Short-term potentiation of the biomimetic synapse in response to gate voltage pulses with  $\Delta t$  set as multiple values of  $\tau_{\text{OECT-SLB}}$ .

**Figure 3.23.** Comparison of the short-term potentiation elicited in the unfunctionalized OECT and biomimetic synapse.

## List of Tables

**Table 3.1.** Diffusion coefficients of POPC bilayer on PEDOT:PSS and glass.

**Table 3.2.** Roughness values of POPC bilayer on PEDOT:PSS and glass.

**Table 3.3.** Numerical data of frequency response measurements obtained through circuital fitting.

## Abstract

Synaptic plasticity is at the base of learning and memory capabilities of the human brain and lately recent studies reported a strong correlation between synaptic dysfunction and neurodegenerative diseases. Unfortunately, the complexity of the brain and the nervous system prevents the investigation of mechanisms underlying cognitive impairment, and for this reason the possibility to inhibit neurodegeneration at the early stage of disease is still far from being concrete. The impossibility to study neuronal cells in their native environment pushed the neuroelectronic field towards the implementation of biomimetic *in vitro* platforms which could resemble the main features of biological synapses, like geometrical shape, structure and functionalities. At this purpose, in recent years supported lipid bilayers and 3D patterned electrodes emerged as promising strategies to mimic neuronal membrane composition and dendritic spines shapes. Additionally, the advent of neuromorphic devices based on conductive polymers provided artificial synapses exhibiting short and long-term plasticity, while being able to transduce biological ionic signals into electrical currents. In this thesis, we present the implementation of biohybrid biomimetic synapses which could pave the way for a new class of adaptable *in vitro* platforms able to trick cells to recognize electronic devices as part of their native environment. The first part of the project was focused on engineering a biohybrid synapse where a PEDOT:PSS-based OECT acts as artificial post-synaptic neuron while cells directly interfaced with the device represent the biological pre-synaptic end. Of note, the OECT conductance can be modulated by the oxidation of dopamine directly secreted from cells, demonstrating neurotransmitter-mediated short and long-term plasticity. In the second part of the project, the OECT was coupled with a synthetic phospholipid bilayer to implement an artificial synapse with biomimetic features. Finally, the role of the biomembrane on the short-term plasticity of the OECT was evaluated varying also the position of the gate electrode in respect to the neuromorphic channel. Here, the SLB behaving as an ionic barrier amplifies the short-term potentiation of the artificial synapse, especially when the top gate electrode forces ions to cross the double layer. In light of the results presented in this thesis, biomembrane-based organic neuromorphic transistor could represent a first step towards the implementation of fully biomimetic *in vitro* systems, which resemble composition and functionalities of neuronal networks and as such, could contribute to unwind the complex mechanisms underlying neurodegeneration and synaptic plasticity loss.

## List of abbreviations

- 3D** Three-dimensional
- AA** Arachidonic acid
- A $\beta$**  Amyloid  $\beta$
- Ab I** Primary antibody
- Ab II** Secondary antibody
- AD** Alzheimer's Disease
- AFM** Atomic Force microscopy
- AMPA**  $\alpha$ -amino-3-hydroxy-5-methylisoxazole-4-propionate
- ANN** Artificial neural network
- APP** Amyloid precursor protein
- ATP** Adenosine triphosphate
- Au** Gold
- BSA** Bovine Serum Albumin
- Ca<sup>2+</sup>** Calcium ions
- Calcein-AM** Calcein acetoxymethyl
- C<sub>DA</sub>** Dopamine concentration
- C<sub>F</sub>** Final concentration
- Cl<sup>-</sup>** Chloride ions
- CNS** Central Nervous System
- CP** Conductive polymers
- CV** Cyclic voltammetry
- DBS** Deep Brain Stimulation
- DIV** Day/s in vitro
- DBSA** Dodecylbenzene sulfonic acid
- DI water** Deionized water
- DMSO** Dimethyl sulfoxide
- DMEM** Dulbecco's Modified Eagle's Medium
- ECM** Extracellular matrix
- ECT** Electrochemical transistor
- EDL** Electric double layer
- EGT** Electrolyte-gated organic transistor
- EIS** Electrochemical impedance spectroscopy
- EOFAD** Early-onset familial Alzheimer's disease

**FA** Fatty acyl  
**F-actin** Filamentous actin  
**FEG** Field emission gun  
**FIB** Focused ion beam  
**F<sub>max</sub>** Maximum fluorescence intensity  
**FRAP** Fluorescence recovery after photobleaching  
**GABA**  $\gamma$  amino butyric acid  
**g<sub>m</sub>** Transconductance  
**GOPS** (3-glycidyloxypropyl)trimethoxysilane  
**G<sub>post</sub>** OEET channel conductance  
**G-protein** Guanine nucleotide-binding proteins  
**HEK** Human embryonic kidney 293 cells  
**ITO** Indium tin oxide  
**I<sub>post</sub>** OEET channel current  
**K<sup>+</sup>** Potassium ions  
**LOAD** Late-onset Alzheimer's disease  
**LTD** Long-term depression  
**LTP** Long-term potentiation  
**MS** Multiple Sclerosis  
**Na<sup>+</sup>** Sodium ions  
**N-cadherin** Neural cadherin  
**NMDA** N-methyl-D-aspartate  
**OEET** Organic electrochemical transistor  
**OMIEC** Organic mixed ionic-electronic conductor  
**Pa** Pascal  
**Parylene-C** Poly(para-chloroxylylene)  
**PBS** Phosphate buffer saline  
**PC-12** Rat pheochromocytoma cells  
**PD** Parkinson's Disease  
**PDMS** Polydimethylsiloxane  
**PEDOT:PSS** Poly(3,4-ethylenedioxythiophene) polystyrene sulfonate  
**PEDOT:Tos** Poly(3,4-ethylenedioxythiophene):tosylate  
**PEG** Poly-ethylene glycol  
**PEI** Poly(ethylenimine)

**PFA** Paraformaldehyde

**PLL** Poly-l-lysine

**PM** Plasma membrane

**PNS** Peripheral Nervous System

**POPC** Palmitoyl-2-Oleoyl-*sn*-Glycero-3-phosphocholine

**PSD** Post-Synaptic Density

**PSEN1** Presenilin 1

**PSEN 2** Presenilin 2

**Pt** Platinum

**PTHF** Polytetrahydrofuran

**PUFA** Poly-unsaturated fatty acid

**PW** Pulse width

**RMS** Root mean-square

**RRMS** Relapsing-remitting Multiple Sclerosis

**ROI** Region of Interest

**Rpm** Rotation per minute

**SALB** Solvent-assisted lipid bilayer

**SEM** Scanning electron microscopy

**SLB** Supported lipid bilayers

**SNARE** Soluble NSF Attachment Protein Receptors

**SPMS** Secondary progressive Multiple Sclerosis

**STDP** Spike-timing dependent plasticity

**STP** Short-term potentiation

**TCH** Thiocarbohydrazide

**Texas Red** 1,2-Dihexadecanoyl-*sn*-Glycero-3-Phosphoethanolamine, Triethylammonium salt

**Ti** Titanium

**T<sub>m</sub>** Melting temperature

**TMS** Transcranial magnetic stimulation

**TRIS** Tris(hydroxymethyl)aminomethane buffer

**UTP** Ultrathin plasticization

**UV** Ultraviolet

**VF** Vesicle fusion

**V<sub>ch</sub>** OECT channel voltage

**V<sub>g</sub>, V<sub>post</sub>** OECT gate voltage

**$V_T$**  OECT threshold voltage

**WE** Working electrode

**$\lambda_{EX/EM}$**  Excitation/emission wavelength

**$\Delta t$**  Time interval between pulses

**$\tau$**  OECT time response

**$\tau_{1/2}$**  Half time of fluorescence recovery

# 1 Introduction

## 1.1 The nervous system.

The brain is the central control system of the body and is responsible for movement, memory formation and behavior. In particular the exchange of information from the brain to different parts of the body and *vice versa* takes place through the nervous system, an intricate and complex network of nerves and cells, which is usually divided in the central nervous system (CNS) and the peripheral nervous system (PNS): here, the CNS is formed by the brain and the spinal cord, while the PNS consists of nerves and other cell types branching throughout the rest of the body and communicating with the CNS <sup>[1]</sup>.

The nervous system is made of two different types of cells: neurons and glia cells. The latter, playing a supporting role to the activity of neurons, can be divided in astrocytes, oligodendrocytes and microglia found in the CNS, and Schwann cells located in the PNS <sup>[2]</sup>. Although glia cells represent the major fraction of the human brain, the fundamental unit of the nervous system are actually neuronal cells, responsible for sending information to other nerve cells, muscle, or gland cells.

The brain present different types of neurons (*i.e.*, motor, sensory and interneurons), all exhibiting the same basic structure with a cell body, called soma, several branches called dendrites and an extra-long branch called axon (**Figure 1.1**). Here, the soma contains the nucleus where neuronal proteins are synthesized, while the elongated protrusions are responsible for neuron-to-neuron communication which occurs at synapses, the site of transmission between two nerve cells, called pre and post-synaptic terminals. In particular, the axon is usually covered with a discontinuous insulating layer called myelin sheet which guarantee the rapid transmission of the electrical signal <sup>[3]</sup>. As ‘command’ center of the human body, dysfunction and disease condition in the brain affects the whole body: brain damage indeed can be caused by psychiatric conditions, strokes or external trauma caused by accidents or neurotoxic chemicals, all resulting in brain cells degeneration and ultimately neuronal death. In general, human brain disorders can be divided in two categories: neurodegenerative diseases and neuropsychiatric disorders, both highly challenging to understand and incurable, although some medicines, surgery and physical therapies are currently available to reduce the progression of the disease and suppress the symptoms <sup>[4]</sup>. Here, the following paragraphs will be focused on neurodegenerative disorders, their pathological causes and potential strategies to develop therapeutic treatments able to inhibit neurodegeneration at the early stage of disease.

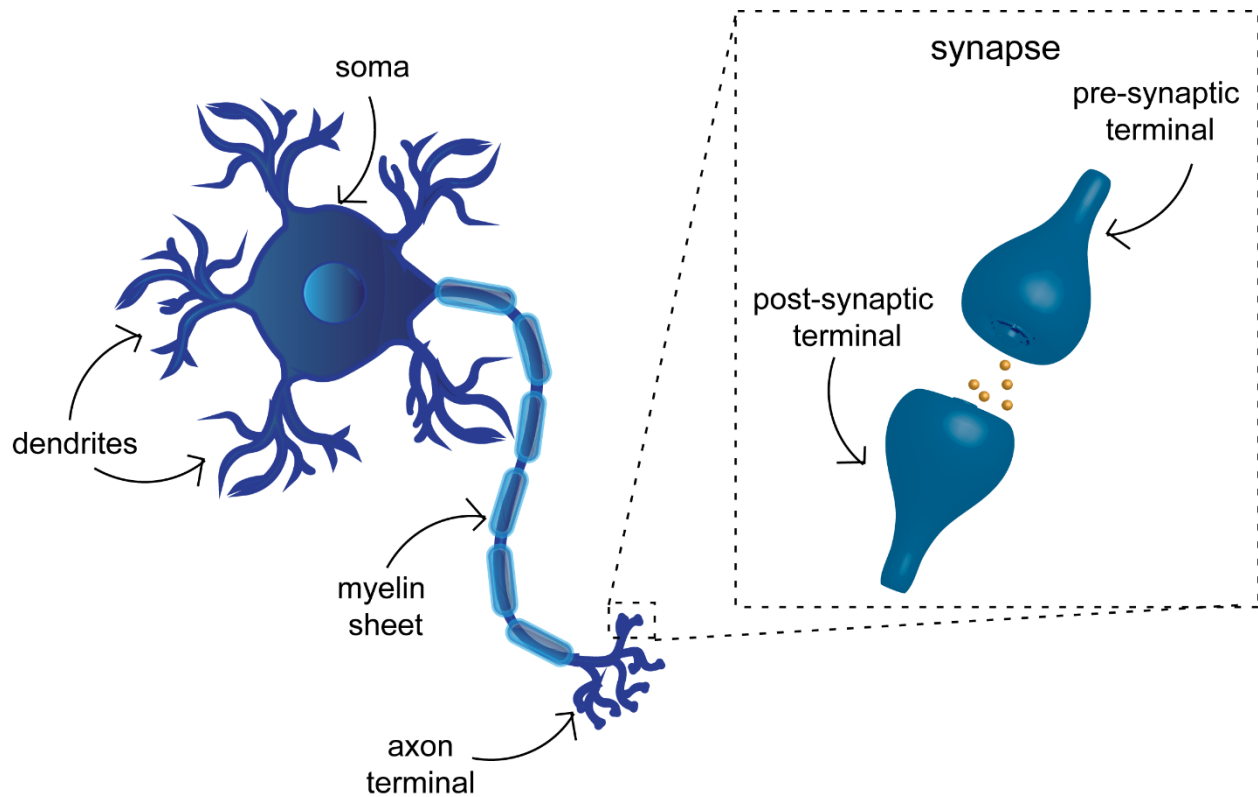


**Figure 1.1. Neuronal structure.** Schematics depicts the main components of biological neurons: cell body or soma containing the nucleus, branched dendrites and the axon covered by the myelin sheet. The inset shows the synapse structure located at the axon terminal where the communication between the pre- and post-synaptic neuron occurs.

## 1.2 Neurodegeneration and aging.

Neurodegenerative diseases, *i.e.*, Parkinson’s (PD), Alzheimer’s (AD) and multiple sclerosis (MS), are age-related conditions that nowadays affect millions of people worldwide and this number is expected to increase: according to the annual report of the Alzheimer’s Disease Association, in 2021 the number of the American’s with AD is around 6.2 million and is expected that by 2030 1.2 million people in the United States could be living with PD <sup>[5]</sup>. These debilitating pathologies, associated with cognitive deficit and/or loss of locomotor functions, are characterized by a progressive decline in brain functions, due to degeneration and/or death of nerve cells <sup>[6]</sup>. Neurodegenerative diseases are strictly related to aging, even though multiple risk factors as environmental triggers and genetic components can contribute: however, as neurodegeneration involves complex cellular and molecular processes, the isolation and characterization of mechanisms underlying cognitive impairment, are highly challenging <sup>[7]</sup>.

### 1.2.1 Alzheimer's disease.

Alzheimer's disease is a neurodegenerative disorder whose causes are still incompletely understood: it is characterized by the loss of cognitive functions and behavioral abilities <sup>[8]</sup>. AD can exhibit two different forms: early-onset familial Alzheimer's disease (EOFAD) and late-onset Alzheimer's disease (LOAD). The latter is the most common form of AD and usually occurs in people of age 65 or older without a family history of dementia; EOFAD, instead can appear even in younger people with genetic mutations in the genes of amyloid precursor protein (APP), presenilin 1 (PSEN1), and presenilin 2 (PSEN2) <sup>[9,10]</sup>. Historically, the accumulation of amyloid  $\beta$  (A $\beta$ ) protein has been recognized as the main cause of neuronal cell death and dementia in AD's patients; however, the unsuccessful trial based on anti-A $\beta$  therapy contributed to redefine AD as a multifactorial disorder and highlighted also the limitations of animal diseases models: here, indeed, mouse models failed in mimicking human AD pathology lacking neuronal loss and proteins tangles <sup>[11]</sup>.

### 1.2.2 Parkinson's disease.

Parkinson's disease affects 1–2% of individuals above the age of 65, and is the second most common age-related neurodegenerative disorder after AD <sup>[12]</sup>. Patients with PD present deep grey matter volume loss due to progressive death of dopaminergic neurons: this leads to multiple motor-symptoms like rigidity and tremors, but also to dementia and cognitive decline <sup>[13]</sup>. At neuropathological level, PD is characterized by the accumulation of protein inclusions within neuronal cell body: these aggregates, known as Lewy bodies, are usually made of insoluble misfolded presynaptic neuronal protein,  $\alpha$ -synuclein <sup>[14]</sup>. Such dysfunction might be related to genetic causes, but only in the 5-10% of cases, while other neuropathological mechanisms are still unknown: therefore, current treatments, based on chemical drugs (*i.e.*, levodopa) <sup>[15]</sup>, or surgical procedures (*i.e.*, deep brain stimulation, DBS) <sup>[16]</sup>, are limited to attenuating motor symptoms.

### 1.2.3 Multiple sclerosis.

Multiple sclerosis is an inflammatory disease that usually affects people, and in particular women, between 20-40 years old <sup>[17]</sup>. MS is characterized by motor dysfunction, tremors, paralysis, loss of coordination and balance, associated to the appearance of demyelinating axons and a reduced population of oligodendrocytes. Usually the symptoms are intermittent in the primary relapsing-remitting MS (RRMS) phase of disease, with increasing deterioration in the patient's quality of life during the secondary progressive MS (SPMS) phase <sup>[18]</sup>. Among multiple factors related to the rise of MS, the activation of T cells has been proposed as possible mechanism responsible for the inflammation and brain tissue damage <sup>[19]</sup>. Another hypothesis instead identifies a genetic mutation as the primary cause of the disease which leads to the death of

oligodendrocytes <sup>[20]</sup>. Also in this case, due to unclear pathogenic mechanisms, current treatments are focused on remyelinating damaged axons to reduce and limit nerve damage, but no drug is able to provide a permanent cure <sup>[21]</sup>.

### 1.3 Pathophysiological mechanisms underlying neurodegeneration.

Lately, increasing evidence identified synaptopathy, (*i.e.*, synaptic dysfunction), and aberration in neuronal membrane as common pathogenic background of several neurodegenerative disorders. Of note, such alteration in neuronal structure and functionalities appear at early or initiating stage of disease, and degenerate along the clinical-pathological course <sup>[22–24]</sup>. For this, the investigation of physiological mechanisms underlying functional impairment could contribute to implement *ad hoc* treatments able to inhibit neurodegeneration prior the appearance of the symptoms.

#### 1.3.1 Synapse structure and action potentials propagation.

Synapses, as the basic information transfer units in the nervous system, are involved in all aspects of neuronal physiology; for this, even slight perturbations of synaptic function can lead to brain disorders <sup>[25]</sup>. Nowadays, two main modalities of synaptic transmission are recognized: electrical and chemical. In general, neurons have a resting potential (*i.e.*, potential across the membrane) of ~60-70 mV, meaning that the inner part of the cell is negatively charged compared to the outer part. However, the opening of ion channels might cause either a depolarization or hyperpolarization of the membrane, depending whether cations (*e.g.*, Na<sup>+</sup>, Ca<sup>2+</sup>, K<sup>+</sup>) or anions (*e.g.*, Cl<sup>-</sup>) enter the cell.

During a depolarization event, if the membrane voltage crosses a threshold value (~ 55 mV), voltage-gated Na<sup>+</sup> ion channels sequentially open and induce the generation of a depolarization wave along the axon, known as action potential <sup>[26]</sup> (**Figure 1.2 A**). In electrical synapses, mostly found in glial cells, when an action potential arrives at the distal end of the pre-synaptic neuron, charged ions or small molecules (*e.g.*, ATP) are transferred to the post-synaptic terminal crossing small pores known as gap junctions <sup>[27]</sup>. Unlike chemical synapses, in electrical synapses, the neurotransmission can be bidirectional, meaning that the ions can flow in either direction across the gap junction (**Figure 1.2 B**), depending whether the action potential is propagated along the pre or post-synaptic neuron. Furthermore, another interesting feature of electrical synapses is the fast transmission as the passage of ions across the gap junctions is instantaneous <sup>[28]</sup>.

The activity of chemical synapses, instead, is based on chemical mediators which enable the transport of information from the pre to the post-synaptic neuron. Chemical synapses transduce either excitatory or inhibitory signals that increase or decrease the action potentials firing in the target cells, respectively <sup>[29]</sup>. In detail, an action potential at the pre-synaptic neuron (usually located at the axons) causes the depolarization of the pre-synaptic membrane and the aperture of voltage-dependent calcium channels with consequent rise of intracellular Ca<sup>2+</sup> levels <sup>[30]</sup>. Increased Ca<sup>2+</sup> concentration activates the synaptic vesicles protein synaptotagmin I which induces the conformational change of the protein complex Soluble NSF Attachment Protein Receptors (SNARE), triggering the fusion of vesicles with the plasma membrane and release of

neurotransmitters (*i.e.*, dopamine, glutamate, serotonin) at the synaptic cleft, a  $\sim 20$  nm space separating the pre- and the post-synaptic components [31]. Here, the activation of specific receptors placed at the post-synaptic membrane allows the influx of ions within the post-synaptic cell and enables the transduction and transmission of the electrical signal (**Figure 1.2 C**): according to the type of neurotransmitters and receptor, either the excitatory or inhibitory pathway will be promoted [29].

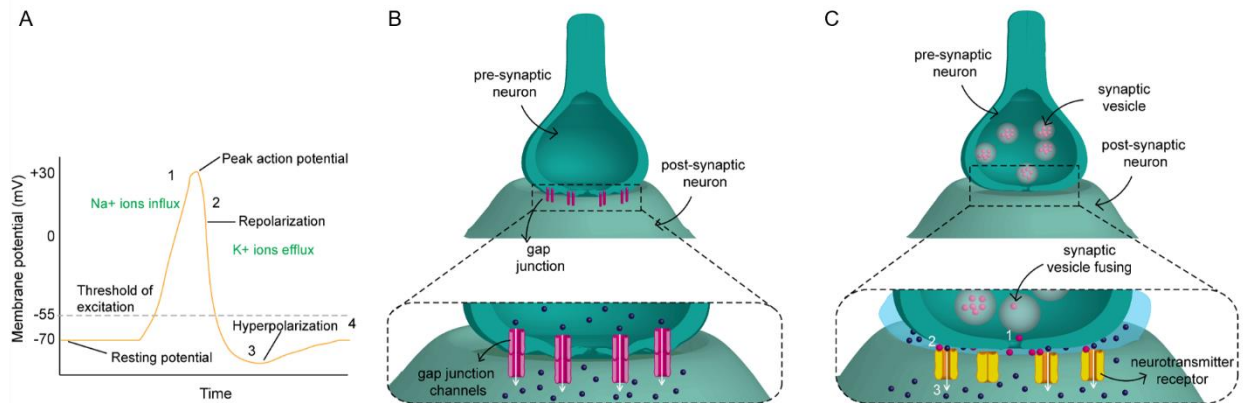


**Figure 1.2. Signal propagation in biological synapses.** A) Action potential signal: the influx of sodium ions causes membrane depolarization with rise of membrane potential (1); the inactivation of sodium channels and activation of potassium channels induces membrane repolarization (2). The subsequent closing of potassium channels and efflux of  $K^+$  ions leads to the hyperpolarization of neuronal membrane (3) until it returns to its resting state 4). B) Schematics reporting the signal propagation mechanism of electrical synapses where gap junction pores guarantee the sealing between pre- and post-synaptic neurons and the passage of ions from one cell to the other. C) Schematics depicting the functioning of chemical synapses: here neurotransmitters released at the synaptic cleft (1) bind to their receptors placed at the post-synaptic membrane (2); the subsequent apertures of ion channels enables the influx of ions and depolarization of the post-synaptic neuron (3).

Excitatory and inhibitory post-synaptic terminals present also different morphology: excitatory post-synapses, generally located on dendritic spines, *i.e.*, small protrusions from dendrites, are usually asymmetrical displaying a protruding electron-dense structure called post-synaptic density (PSD); on the other hand, inhibitory post-synapses, usually formed directly at the soma or dendritic shaft, present a symmetrical synaptic junction with a smoother PSD [32]. Furthermore, the shape of dendritic spines is highly variable depending on different brain areas, cell type and animal species [33].

Traditionally, dendritic spines, characterized by a thin neck attached to the dendrite and a head bearing the PSD domain, have been classified in four groups according to their morphology: mushroom, thin, stubby, and filopodia [34] (**Figure 1.3**). Mushroom spines present a large head and a small neck (**Figure 1.3**, blue spine), and have been defined as the storage sites of long-term memory since they form strong synaptic connections and have the longest lifetime [35]. Thin spines have a structure similar to the mushroom spines,

but display a smaller head (**Figure 1.3**, yellow spine): these spines, called also learning spines, are in charge of creating new memories during the synaptic plasticity process <sup>[36]</sup>. Stubby spines typically do not have a neck (**Figure 1.3**, green spine) and can be usually found in the early stages of postnatal development <sup>[37]</sup>. Finally, filopodia, very mobile and flexible structures, are thin membrane protrusions without a defined head (**Figure 1.3**, red spine): indeed, in most cases these spines do not have PSD which suggests that they do not form functional synapses. However, under certain conditions like brain injury, filopodia can be found also in mature neurons at the early stage of synaptogenesis <sup>[38]</sup>. Nonetheless, under physiological conditions, the four morphological shapes of dendritic structures are just transitory due to the plasticity of spines which constantly undergo reshaping in response to neuronal activity <sup>[39]</sup>. In particular, filopodia are the most dynamic dendritic protrusions as they can appear and disappear within 10 minutes, but can also evolve into spines <sup>[40]</sup>. In contrast, stubby and thin spines are less dynamic than filopodia and can display head enlargement and persist over several days <sup>[41]</sup>. Finally, the least dynamic structures are the mushroom-like spines as they can be stable over several months <sup>[42]</sup>. Spines' remodeling is associated to brain development, but also to learning and experience: for instance, motor learning promotes the growth of new spines and the subsequent elimination of the ones existing before training <sup>[43]</sup>; furthermore, various stimuli like fear or stress can cause spines turnover (*i.e.*, formation and elimination) <sup>[44,45]</sup>. Lately, morphologic abnormalities of dendritic spines have been observed in various neurologic diseases <sup>[46]</sup>: for instance, the hippocampal and cortexes areas of AD's patients revealed spine shrinkage during the early stage of disease, prior the appearance of clinical symptoms <sup>[47]</sup>; similarly, remodeling of glutamatergic synapses has been correlated to  $\alpha$ -synuclein deposits in Parkinson's disease <sup>[48]</sup>. This suggests that balance between spine appearance, maturation, elimination, and plasticity is crucial to preserve proper brain function.

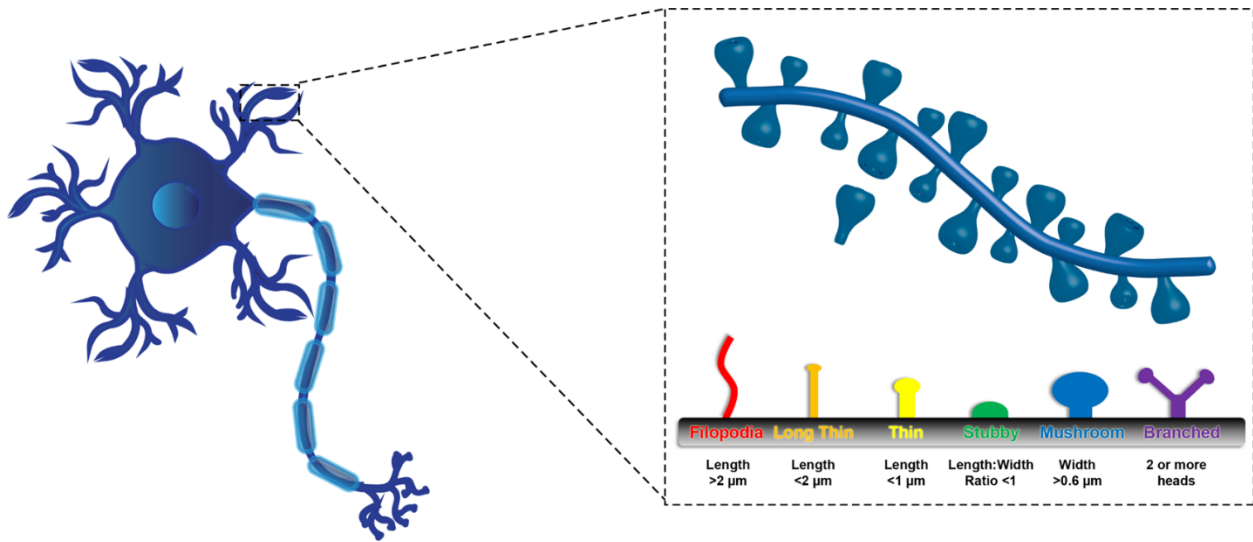


**Figure 1.3. Dendritic spines morphology.** Schematics depicting the geometrical features of dendritic spines from long, thin filopodia type structures (red) to wide-headed mushroom spines (blue) and the occasional branched spine (purple). Adapted from ref. [34].

#### 1.3.1.1 Neurotransmitters and post-synaptic receptors.

The signal transmission along chemical synapses involves neurotransmitters and post-synaptic receptors, which ensure the transduction of pre-synaptic firing into an ionic signal, and then again into an electrical post-synaptic action potential. As they play such a crucial role in the brain, neurotransmitters and receptors represent critical targets for developing therapeutic drugs to treat psychiatric and neurological disorders <sup>[49]</sup>. As described in the previous paragraph, neurotransmitters are stored within pre-synaptic vesicles until the propagation of an action potential induces their release at the synaptic cleft. Here, neurotransmitters that activate cationic channels (*i.e.*, acetylcholine, glutamate), and therefore induce depolarization of the post-synaptic neuron, are classified as excitatory, while neurotransmitters activating anionic channels (*i.e.*,  $\gamma$  amino butyric acid, GABA) can be defined as inhibitory <sup>[50]</sup>. Of note, the excess of released neurotransmitters that did not bind to any receptor, is promptly removed from the synaptic cleft to avoid their diffusion towards inappropriate synapses. In particular, neurotransmitters inactivation can involve specific transporters, as in the case of dopamine, serotonin and glutamate, which mediate the recycling and reuptake of the neurotransmitter at the pre-synaptic neuron, or enzymatic degradation, as in the case of acetylcholine which is degraded by acetylcholinesterase into acetate molecules and choline; the latter, is then reabsorbed into the presynaptic terminal and used in the synthesis of new acetylcholine <sup>[51]</sup>. Furthermore, neurotransmitters like acetylcholine, glutamate and GABA can bind both ionotropic receptors and metabotropic ones <sup>[52]</sup>. These two families of receptors exploit different signal transduction pathways:

ionotropic receptors (*i.e.*,  $\alpha$ -amino-3-hydroxy-5-methylisoxazole-4-propionate (AMPA) and N-methyl-D-aspartate (NMDA)) known also as ligand-gated ion channels, combine receptor and channel functions in a single protein complex (**Figure 1.4 A**), while metabotropic ones (*i.e.*, serotonin, dopamine and epinephrine receptors), require a multistep process involving the activation of guanine nucleotide-binding proteins (G-proteins) which modulate ion channels directly or indirectly through intracellular enzymes and second messengers <sup>[53]</sup> (**Figure 1.4 B**). Unlike ionotropic receptors, in some cases the activation of metabotropic ones do not induce variation in membrane potential, but rather activates protein kinases that, phosphorylating ion channels, elicit excitatory or inhibitory neurotransmission <sup>[54]</sup>. Due to their working mechanism, ionotropic and metabotropic receptors require different times to elicit a post-synaptic potential: ligand-gated ion channel generally mediate rapid post-synaptic effects (within few milliseconds), while G-protein coupled receptors usually produce slower physiological responses (hundreds of milliseconds to minutes) <sup>[53]</sup>.

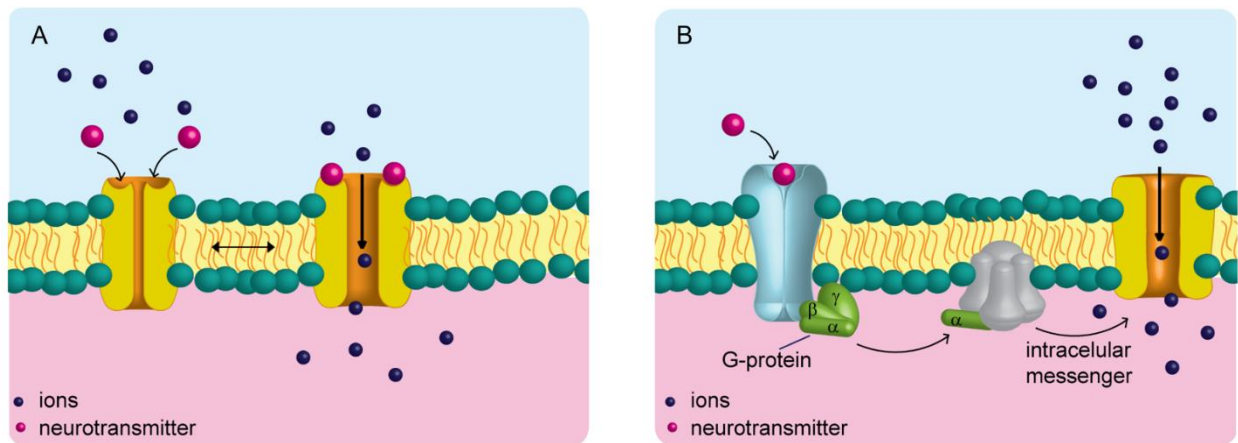


**Figure 1.4. Neurotransmitter receptors.** A) Schematics of ligand-gated neurotransmitter receptors: the combination of the neurotransmitter binding site and ionic channel in a single protein complex enables the direct influx of ions upon the aperture of the ion channel. B) Functioning of metabotropic receptors where the neurotransmitter-mediated signal transmission requires the activation of the G-protein complex and intracellular messenger in order to trigger the aperture of ion channels. Adapted from ref. [53].

### 1.3.2 Synaptic dysfunction in neurodegeneration.

One of the most fascinating properties of the brain is its plasticity, referring to the ability of synapses to modify the strength and efficacy of signal transmission according to external stimuli: in particular, the potentiation (excitatory pathway) or depression (inhibitory pathway) of the synaptic strength can occur on different temporal domains ranging from milliseconds-seconds (short-term plasticity) to hours-days or even longer (long-term plasticity) <sup>[55]</sup>. Furthermore, according to the Hebbian learning principle, the strength of synaptic connection is strengthened if the pre-synaptic spike occurs right before the post-synaptic one, while

in the reverse timing synaptic connection is weakened: this phenomenon is known as spike-timing dependent plasticity (STDP) and can be nicely described as “*neurons that wire together, fire together*”<sup>[56]</sup>. Of note, while early studies identified synaptic plasticity as a post-synaptic mechanisms, nowadays it is clear that modification in synaptic strength involves both pre and post-synaptic terminals, modifying either post-synaptic receptors (post-synaptic plasticity) or the concentration of neurotransmitters released (pre-synaptic plasticity)<sup>[57]</sup>. Short-term plasticity, involved in short-term adaptation and short-lasting forms of memory, is initiated by short bursts of activity which cause a transient accumulation of  $\text{Ca}^{2+}$  at the pre-synaptic neuron, enhancing neurotransmitters releasing. In particular, when two stimuli are delivered within few milliseconds (paired-pulse stimulation), the synaptic connection can be either enhanced or depressed: paired-pulse depression is usually observed within 20 ms and is probably related to the inactivation of voltage-dependent sodium or calcium channels. On the other side, paired-pulsed facilitation occurs in response to longer interstimulus intervals (20-500 ms) and perhaps involves the activation of protein kinases that modulate the activity of presynaptic phosphoproteins<sup>[58]</sup>. Additionally, trains of stimulation (~ 200 ms – 5 s) results in prolonged facilitation/depression of synaptic strength, as the concentration of calcium in the pre-synaptic terminal continues to build up upon subsequent action potentials, enhancing directly the release of neurotransmitters or triggering modifications of pre-synaptic proteins<sup>[59]</sup>.

Short-term plasticity is involved in multiple fundamental processes, as short-term and working memory and decision making, all operations based on the temporary storage and management of information: here, neurotransmitters released upon stimulation act as memory trace, which decays over time due to the reuptake of neurotransmitters<sup>[60]</sup>. Long-term plasticity is identified as one of the primary mechanisms for learning and memory, as it implies long-lasting modification of synaptic efficacy<sup>[61]</sup>. Also in this case synaptic strength can be either enhanced (long-term potentiation, LTP) or depressed (long-term depression, LTD). Usually long-term plasticity is elicited by high-frequency stimulation of the neural pathway or repeated pairings of pre and post-synaptic cell firing: here, if pre-synaptic burst occurs before post-synaptic one, LTP is generated (**Figure 1.5 A**), while reversed firing generates LTD<sup>[62]</sup>. LTP and LTD can be generated by both ionotropic and metabotropic receptor activation. In particular, in case of LTP most synapses involve glutamate as excitatory neurotransmitter and depend on the activation of NMDA receptors. In detail, the increase of  $\text{Ca}^{2+}$  concentration triggers intracellular signaling cascades involving protein kinases; consequently, new AMPA receptors are incorporated within the PSD domain of the dendritic spines. Such mechanism induce structural changes within the synapse as PSD and dendritic spines are permanently enlarged<sup>[63]</sup>. Conversely, in NMDA-mediated inhibitory synapses responsible for LTD, the rise of  $\text{Ca}^{2+}$  levels triggers protein phosphatases which cause the dissociation and consequent endocytosis of AMPA receptors from the PSD: such loss results in shrinkage in size of dendritic spines<sup>[64]</sup> (**Figure 1.5 B**). Lately, synaptic plasticity alterations have been observed in the early asymptomatic phase

of many neurological disorders as AD and PD <sup>[65]</sup>. For example in case of AD, the accumulation of A $\beta$  oligomers causes the anomalous activation of NMDA receptors, Ca<sup>2+</sup> dysregulation and cellular stress <sup>[66-68]</sup>; furthermore, soluble A $\beta$  affects also the release of neurotransmitters at excitatory synapses causing synaptic dysfunction <sup>[69]</sup>. Interestingly, synaptic alterations seem occur prior extensive neuronal degeneration, and therefore are likely responsible for cognitive impairment and memory loss in AD's patients <sup>[70]</sup>. Similarly, dystrophy of dopaminergic synapses characterizes the early stages of PD: indeed, aggregation of  $\alpha$ -synuclein causes misfolding of the SNARE protein complex reducing dopamine released at the synaptic cleft and inducing neurodegeneration <sup>[71]</sup>. As synaptic plasticity alterations appear in the early asymptomatic phase of neurological diseases, strategies aimed at preventing synapse failure might provide great benefits for cognitive decline and motor deficits. In this context, in order to improve neuroplasticity, some innovative therapeutic methods like neuropharmacological interventions or brain stimulation have been implemented. The latter in particular, exploits bioelectronic devices directly interfaced with the brain to alleviate/delay the progressive of clinical deterioration: for example, transcranial magnetic stimulation (TMS) exploits brief electrical current produced by a coil placed on the surface of the skull, while in case of DBS the electrical current is delivered by an electrode implanted within the brain structure <sup>[72]</sup>. Although these research developments and technological innovations represent a promising therapeutic approach to inhibit the progression of the disease, further work is required to identify molecular mechanisms underlying neurodegenerative disorders.

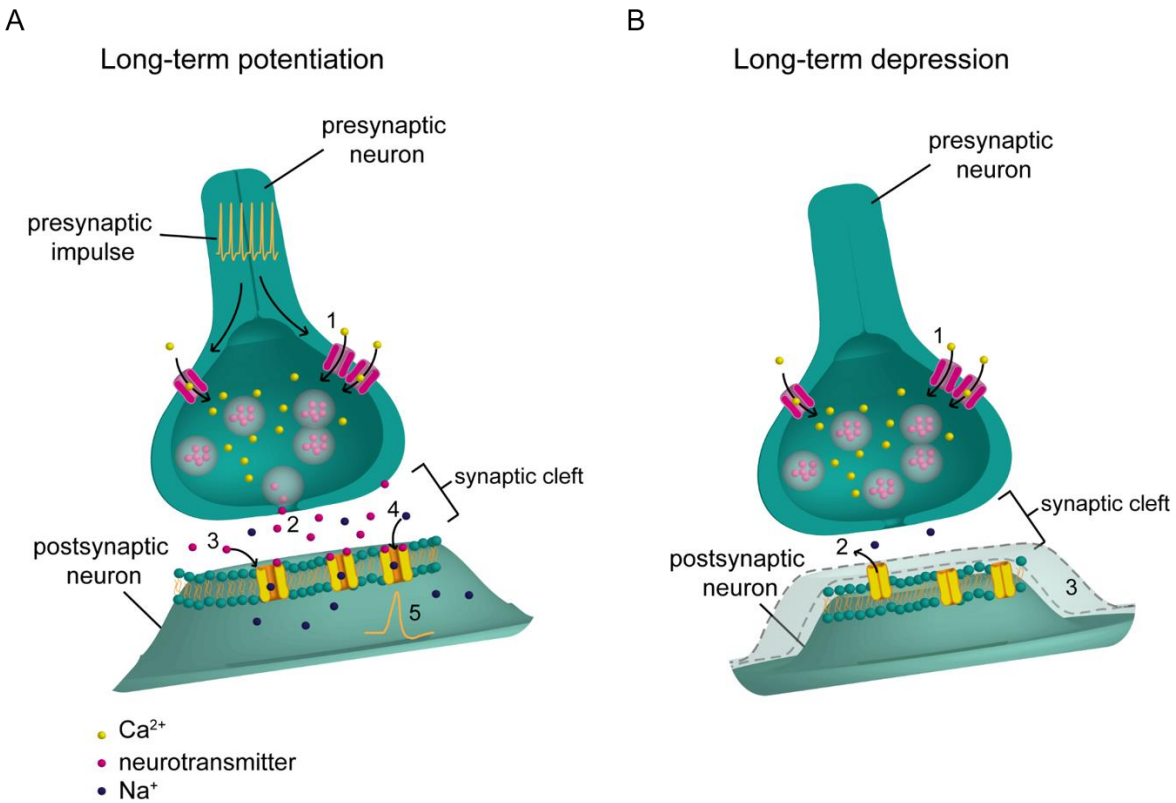


**Figure 1.4. Synaptic plasticity.** The schematics depict the mechanisms underlying the plastic behavior of biological synapses. A) Long-term potentiation of synaptic connection, triggered by the repeated stimulation of the pre-synaptic neurons: high frequency action potentials induce the continuous influx of  $\text{Ca}^{2+}$  ions at the pre-synaptic terminal (1) and the progressive accumulation of neurotransmitters at the synaptic cleft (2), with consequent enhancement of post-synaptic receptors activity (3). The major influx of ions within the post-synaptic neuron (4) therefore results in the generation of multiple post-synaptic signals strengthening the synaptic connection between the two nerve cells (5). B) Depression of synaptic strength following the activation of phosphatases in response to calcium influx (1), which induces the withdrawing of post-synaptic receptors (2) with consequent reduction of dendritic spines size (3).

### 1.3.3 Cell membrane role in neurodegeneration.

The cell membrane, as the cell first outpost at the interface with the extracellular world, acts as a mechano-chemical transducer, mediating cell communication with its microenvironment and with neighboring cells: indeed, besides merely acting as a physical barrier, the plasma membrane (PM) is a highly dynamic structure that can stretch, bend and bud coordinating several processes as the cell interfaces with the extracellular matrix (ECM) [73]. PM has a peculiar structure constituted of an asymmetric bilayer where the inner and the outer leaflets are made of different lipid molecules [74], while sterols and proteins are distributed within the membrane according to their hydrophilic/hydrophobic domains [75] (**Figure 1.6**).

Here, the lipid composition defines also the fluidity, thickness and curvature of PM, crucial parameters to enable PM activity.

Synaptic membranes, for instance, are enriched of poly-unsaturated fatty acids (PUFA) and cholesterol which allow the extensive restructure of the membrane required during neurotransmission [76–78]. For instance, in the pre-synaptic membrane, the fatty acyl (FA) chain length determines membrane deforming ability, as cone-shaped lipids (*i.e.*, lipids with a small head) induce a positive curvature in PM destabilizing the bilayer and promoting vesicles fusion. Additionally, even the lipid polar head plays a crucial role in signal transmission, as negatively charged lipids as phosphatidylserine present in the pre-synaptic membrane mediate the fusion and exocytosis of pre-synaptic vesicles [79,80]. Furthermore, the saturation state of FA chains and the percentage of cholesterol regulate the dynamicity of the membrane and therefore control proteins activity: PUFA indeed have higher conformational flexibility compared to rigid saturated fatty acids, and therefore can better accommodate conformational changes in transmembrane proteins [81]. On the other hand, cholesterol reducing membrane fluidity and thanks to its ability to translocate between lipid leaflets, is able to release PM stress in the expanded curved leaflet by packing between lipid head groups and inducing the formation of lipid rafts, *i.e.*, microdomains rich of cholesterol and sphingomyelin involved in the clustering and trafficking of receptors [82,83].

At the same time, the structure of the post-synaptic membrane is specialized to receive the neurotransmitter signal and transduce it into electrical and biochemical changes in the post-synaptic cell. Here, as described in **Paragraph 1.3.1**, PSD domain is the active region containing neurotransmitter receptors, cytoplasmic signaling molecules as phosphatases and kinases, and cell adhesion molecules like neural cadherin (N-cadherin), which guarantee the initial contact and alignment between the pre and the post-synaptic cell [84]. Similarly to the pre-synaptic membrane, even PSD present a dynamic structure able to rearrange during neurotransmission, to enable for instance the incorporation and removal of the AMPA receptor during LTP and LTD: however, the mechanism underlying PSD remodeling is still unclear. As pre- and post-synaptic membrane play a crucial role in synaptic transmission, it is not surprisingly that the altered neuronal functionalities found in neurodegenerative disorders might be a consequence of membrane dysfunction [85]: for instance, seems that aggregates of  $\alpha$ -synuclein may form pores at the neuronal membrane leading to membrane disruption and neuronal impairments [86]. Additionally, AD patients have shown alterations in cholesterol synthesis, transport and uptake and even though the exact mechanism is yet to be defined, seems that imbalances in cholesterol levels promote APP accumulation in lipid rafts and the formation of amyloid plaques [87,88].

Considering how much is still unknown and unexplored of mechanisms underlying neurodegeneration, and taking into account also the recent failure of clinical trials which has highlighted the limitations of using animal disease models in the earliest phases of drug screening, there is a growing interest for implementing

*in vitro* models able to recapitulate all the key aspects of neurodegenerative diseases, and therefore allowing the detailed investigation of their pathophysiology, bridging also the gap between current pre-clinical animal models and humans [89].

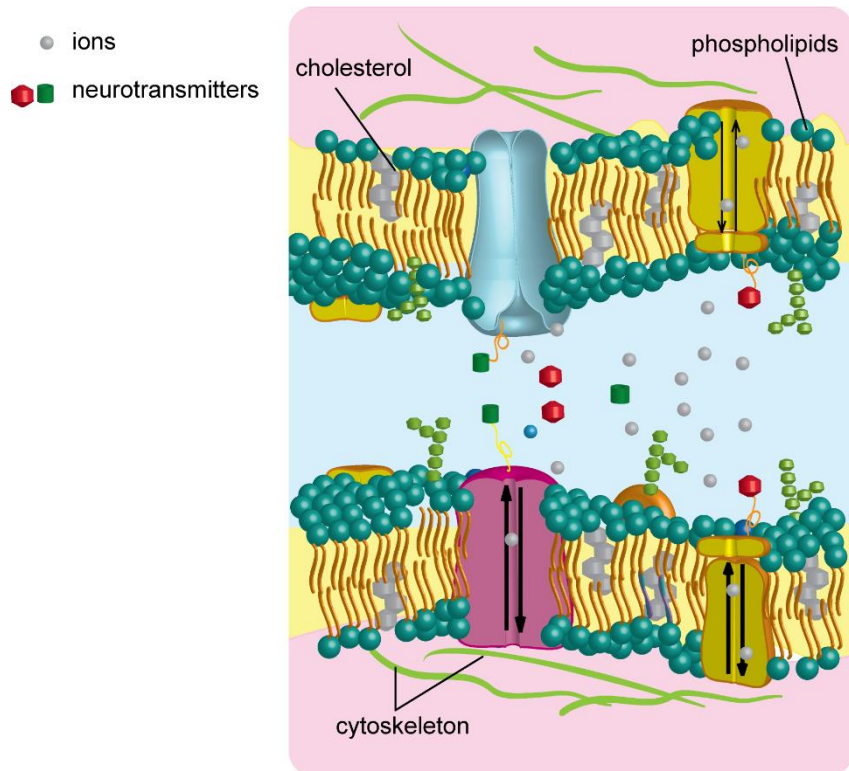


**Figure 1.5. Neuronal cell membrane composition.** The schematics highlights the complex structure of neuronal membranes with proteins and biomolecules embedded within the phospholipids-cholesterol double layer.

## 1.4 Biomimetic approaches in neuronal-chip coupling

Neuroelectronics, a broad discipline of bioelectronics, is an interdisciplinary field which aims to establish a synergy between electronics and the neural tissue, from individual neurons to large neural networks, implementing *in vitro* platforms and implantable devices which exploit electromagnetic fields at the interface with biological systems. therefore here the physical coupling between the electrogenic neuronal cells and external devices is essential to enable the recording and stimulation of biological electrical signals. As described in **Paragraph 1.3.2**, neuroengineered implantable devices can be very efficient to treat the consequences of neurodegenerative diseases, as in the case of electrical and DBS where artificial devices connected with the brain can initiate/inhibit neuronal activity<sup>[90]</sup>. However, prior to engineering devices for *in vivo* applications, it is crucial implementing *in vitro* platforms able to transduce, modulate, and decode neural signals: such neural interfaces could indeed provide a better knowledge of mechanisms underlying neurodegenerative diseases, allowing the development of *ad hoc* therapeutic treatments<sup>[89,91]</sup>. Currently, different methods are available for recording and stimulating neuronal activity, where patch clamp electrophysiology and multi-electrode arrays play the major role for the investigation of intracellular and extracellular signals, respectively<sup>[92,93]</sup>. In detail, patch clamp, the gold standard technique for recording action potentials of excitable cells, exploits the suction of the cell membrane into a pipette enabling the recording of currents flowing across the membrane<sup>[94]</sup>.

The monitoring of extracellular signals, instead rely mainly on planar electrodes directly in contact with cells, therefore great effort has been deployed to optimize the physical coupling between cells plasma membrane and the device surface to reduce the signal-to-noise ratio during stimulation/recording. At this purpose, in recent years, the attention of neuroelectronics field has shifted towards biomimetic approaches focused on designing components and structures inspired to biological systems<sup>[95,96]</sup>: indeed, functionalizing bioelectronic devices with chemical and physical cues that resemble physiological conditions of cell-cell and cell- ECM interactions can effectively disguise conductive materials to ‘trick’ cells to recognize artificial platforms as part of their biological environment, thus maximizing cellular interactions at the interface<sup>[97]</sup>.

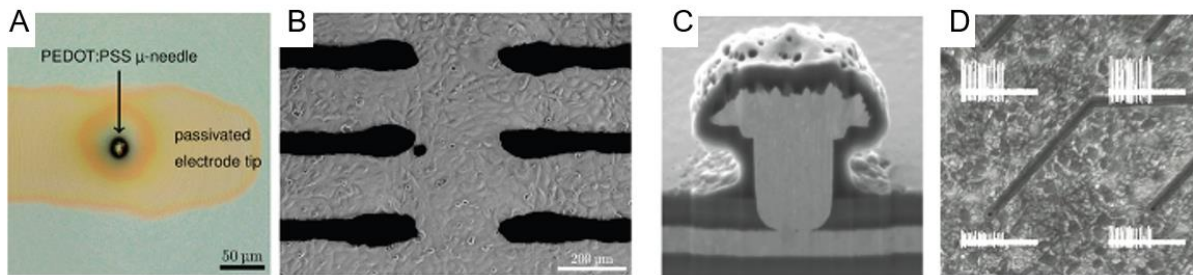
In this way, artificial electrical components might be seamlessly integrated within biological systems leading to the development of biohybrid devices.

### 1.4.1 Conductive polymers.

Cells in contact with electronic materials suffer the mechanical mismatch due to the hardness of the device and the cellular/ECM component Young’s modulus (~ 100 Pa-10 kPa). In fact, recently organic materials like conductive polymers (CPs) (Young’s modulus ~ 20 kPa-3 GPa) have become one of the most popular

choices for bioelectronic devices (**Figure 1.7**), overcoming for some applications, the traditional inorganic conductors like metals and silicon (Young’s modulus  $\sim 45\text{-}500$  GPa), which have always played a leading role in the field [98–100]. In addition to their low modulus, CPs exhibit a peculiar conduction mechanism based on ionic-to-electronic current transduction, as such materials have the intrinsic ability to convert an ion flow to different electronic conduction states, unlike inorganic materials which are not permeable to ions [101,102].

### In vitro applications



### In vivo applications

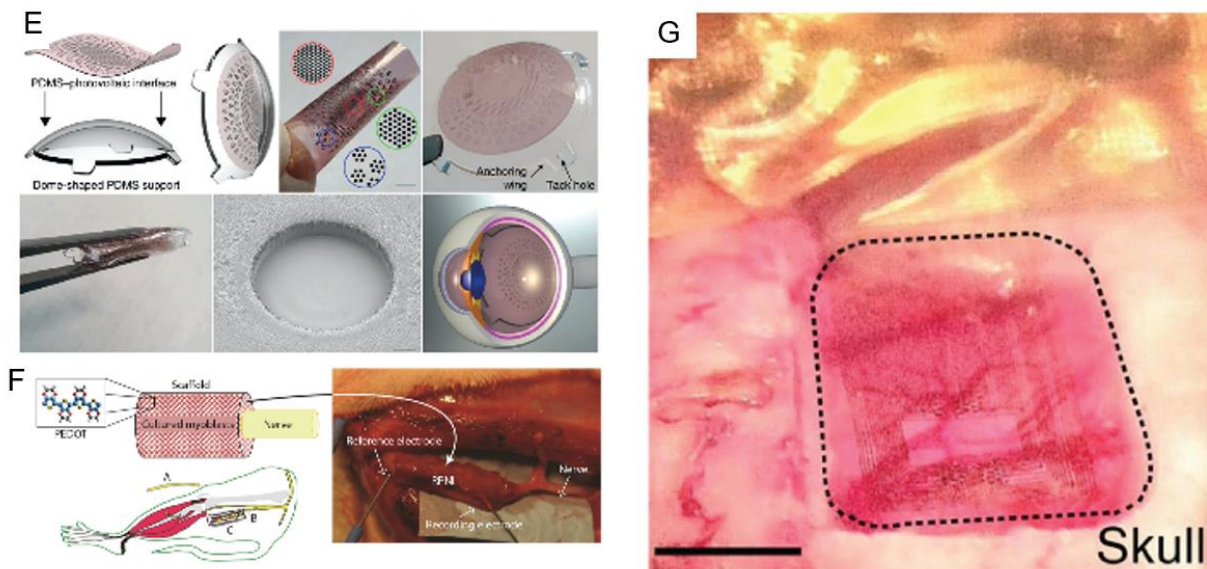


**Figure 1.6. CP-based bioelectronic platforms.** A) Microscopic image of a PEDOT:PSS-coated microneedle electrode and (B) HL-1 cardiomyocytes plated on the microneedle MEA. Adapted from ref. [103]. C) SEM cross-section (focused ion beam) of PEDOT:PSS-coated electrode and (D) Microscopic image of rat cortical cells grown on PEDOT:PSS-coated electrodes. Adapted from ref. [104]. E) P3HT-based photovoltaic pixels integrated into a foldable prosthetic implant for minimally invasive implantation into the eye. Adapted from ref. [105]. F) Regenerative peripheral nerve interface (RPNI) based on a scaffold of a cellular muscle coated with PEDOT that contains myoblasts and is wrapped around the end of the peripheral nerve. Adapted from ref. [106]. G) Optical micrograph of a PEDOT:PSS-based electrocorticography (ECoG) probe placed over the somatosensory cortex, with the craniotomy surrounded by dashed lines. Scale bar, 1 mm. Adapted from ref. [107].

As shown in **Paragraph 1.3.1** also the nervous system operates transducing electrical currents (*i.e.*, action potentials) into ionic signals, therefore organics, matching the conduction properties of living systems, ensure a straightforward and high-efficient signal transduction at the interface <sup>[108]</sup>. In detail, the electrical conductivity of CPs is attributable to the high conjugation of the polymer backbone: electrons are delocalized along the whole chemical structure due to the presence of chemical double bonds which allow the free movement of electrons among atoms <sup>[109,110]</sup>. The electrical conductivity of organic CPs can be easily controlled by the addition of chemicals (usually anions) able to dope the polymer as p-type or n-type <sup>[99]</sup>.

Because of their ionic-to-electronic current transduction, organic CPs can be defined as organic mixed ionic-electronic conductors (OMIECs), which identify a class of soft electrical (semi-) conductors, often polymers, able to transport ionic species under an applied potential <sup>[111]</sup>. Thanks to their conductive features, lately CPs emerged as leading materials in the design of organic electrochemical transistors (OECTs), three-terminal devices whose electrical operation depends on the injection of ions from an electrolyte into the bulk of an organic semiconductor channel <sup>[112]</sup>. These CP-based OECTs found extensive application as biosensors to continuously monitor biological processes at the interface <sup>[99]</sup>. For instance, the OECT *in situ* signal amplification, improving signal-to-noise ratio, enables fast and precise recordings from electrogenic cells <sup>[113–115]</sup> (**Figure 1.8**), or the detection of biological molecules, including neurotransmitters <sup>[116]</sup>.

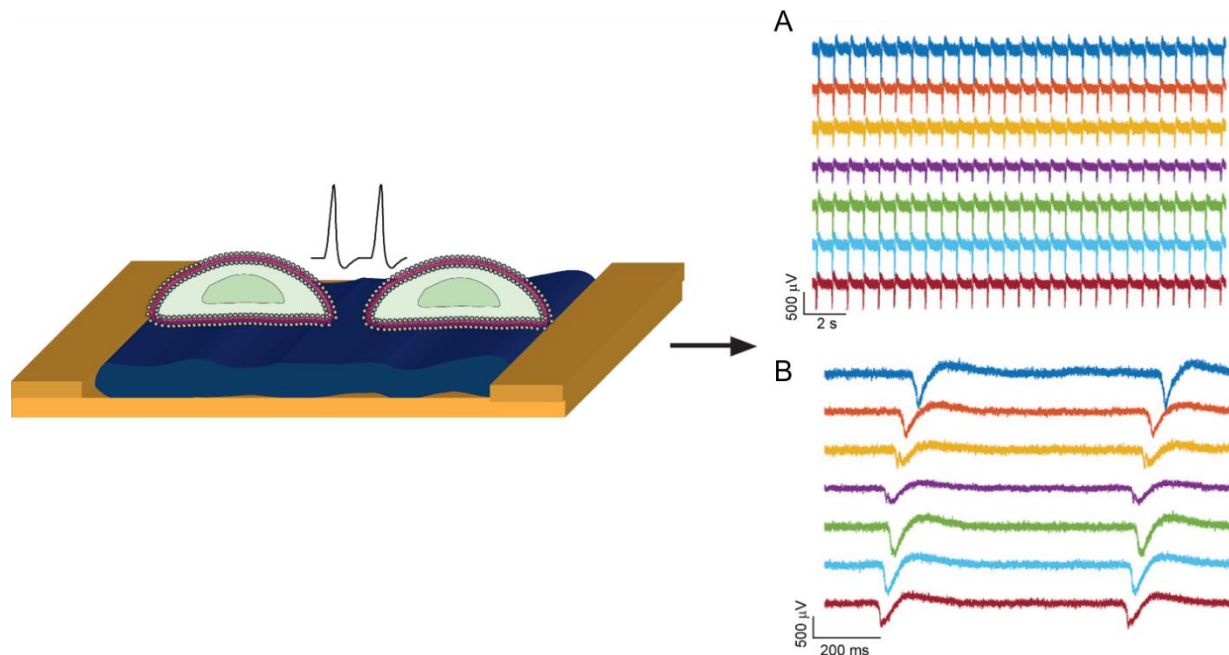


**Figure 1.7. Conductive polymers-based biosensors.** A) Action potentials signals recorded from cardiomyocytes (HL-1) cells interfaced with an organic electrochemical transistors. B) Shapes of individual action potentials displayed in (A). Adapted from ref. [115].

Additionally, CPs offer also the possibility of being functionalized with biomimetic cell-adhesive molecules to gain a tighter apposition of cells onto planar substrates<sup>[117]</sup>. CPs indeed can undergo multiple functionalization strategies where proteins like collagen or laminin-derived peptide, can be physically adsorbed (**Figure 1.9 A**) or covalently bound (**Figure 1.9 B**) on the polymer surface<sup>[118,119]</sup>. Another route to CPs functionalization for biointerface applications is through the incorporation of bio-adhesive molecules in the polymer matrix<sup>[120,121]</sup> (**Figure 1.9 C**). When polymers are synthesized by oxidation of the monomer, the concomitant incorporation of a negatively charged dopant is used to neutralize the positively charged polymer, stabilizing its backbone<sup>[99,122]</sup>. Therefore, biomolecules bearing negative charges like ECM-derived glycosaminoglycans, can act as biodopants when embedded into the polymer matrix<sup>[123]</sup>.

Although the recent development of CP-based neuroelectronic platforms allowed to reduce the mechanical mismatch with neuronal interface and improved cell-chip coupling by means of surface functionalization strategies, such platforms still lack biomimetic features which could actually recapitulate the complexity of cells native environment. Furthermore, functional neural interfaces require a bidirectional communication between biological cells and their artificial counterpart: however, currently available neuroelectronic systems act mainly like “passive” devices, able to monitor/stimulate cells, but without providing any feedback<sup>[124–126]</sup>. Here, the following paragraphs present biomimicry strategies exploited to engineer *in vitro* platforms emulating synaptic functionalities, *i.e.*, synaptic plasticity, and resembling neuronal

architecture, in terms of geometry and cell membrane composition, in order to achieve an intimate coupling between neurons and electrical components.

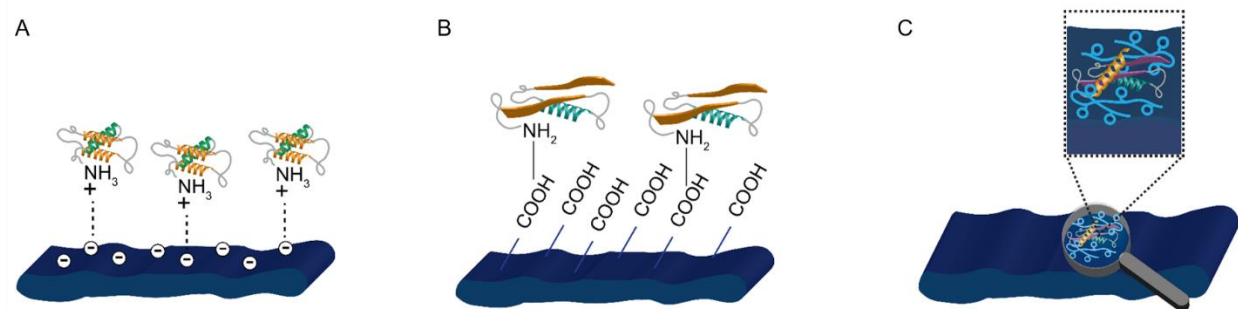


**Figure 1.8. Chemical functionalization strategies of conductive polymers.** Schematics depicts the multiple approaches to functionalize conductive polymers surface with extracellular matrix proteins exploiting either A) electrostatic interactions, B) covalent bindings or C) employing biomolecules as doping agents within the polymeric structure. Adapted from ref. [127].

#### 1.4.2 Functional biomembranes.

Considering these recent highlights concerning the role of cell membranes in early stages of synaptic degeneration, the implementation of lipid-modifying drugs appears as a promising approach to inhibit the progression of neurodegenerative disorders <sup>[128,129]</sup>. However, in order to develop target-specific drugs it is crucial clarify mechanisms underlying cell membrane disruption: for this, *in vitro* biomimetic platforms which present the same PM structure and dynamics represent an optimal strategy to replicate some of the complexity of the *in vivo* environment and investigate the role of cholesterol and synaptic proteins in neurodegeneration. At this purpose, supported lipid bilayers (SLBs) found widespread use to mimic cell membrane structure and to study the physicochemical properties of lipids and the interaction with proteins <sup>[130]</sup>. SLBs are synthetic biomembranes made of lipid molecules assembled on solid supports with a thin hydration layer separating polar heads from the substrate surface: as planar two dimensional structure, SLB can recapitulate the lateral diffusivity of native membranes. The main advantage of these artificial bilayers is that their composition can be easily modified choosing among a multitude of commercially available lipids and functionalizing the double layer with analytes and proteins of interest <sup>[131]</sup>. Among multiple techniques available to assemble SLBs on rigid supports, vesicle fusion (VF) is the one that finds major application due to its simplicity and versatility. In detail, VF is a two-step process based on membrane tension, vesicle-vesicle and vesicle-substrate interactions <sup>[132]</sup>: here, vesicles are first adsorbed on the substrate surface, then once a critical concentration of surface-adhered vesicles is reached, the rupture and fusion of the vesicles lead to the formation of a complete SLB (**Figure 1.10 A**). VF is highly-dependent on the lipid composition of the vesicles as lipid polarity, acyl chain length and degree of unsaturation all

contribute to ease vesicle rupture <sup>[131]</sup>. Furthermore, vesicle rupture is a thermally activated process <sup>[133]</sup>. Lipid molecules, characterized by a melting temperature ( $T_m$ ), can undergo a transition phase passing from a liquid disordered state ( $T > T_m$ ) to a gel ordered phase ( $T < T_m$ ): the latter, presenting lower lipid mobility, impede VF unless the operating temperature is raised above  $T_m$  <sup>[134]</sup>. Similarly, SLB including sphingolipids and high percentage of cholesterol (above 33 mol %) present tightly packed liquid ordered domains (*i.e.*, lipid rafts) with decreased mobility, therefore a heating step is required to induce vesicles rupture <sup>[135,136]</sup>. However, increasing temperature may not be always an option as in presence of membrane embedded proteins. Besides the lipid composition, even vesicles-substrate interactions could be a limiting factor for the successful formation of SLB: here, the electrostatic attraction between vesicles and the substrate can be enhanced adjusting the buffer pH to modify the lipid charge <sup>[137]</sup>. At the same time hydrophilic substrates, like silica, glass, mica, and quartz, provide the adhesion and hydration forces necessary to promote vesicles rupture as well as the formation of a hydration layer fundamental to mimic lipid lateral mobility of native cell membranes <sup>[138]</sup>. Furthermore, the water cushion ( $\sim 1-3$  nm) separating the SLB from the solid support, is often insufficient when studying lipid bilayers with transmembrane proteins, as the cytosolic domain of the protein might be altered from the contact with the substrate leading to protein denaturation <sup>[139]</sup>. At this purpose, additional methods which enable SLB formation on various supports as well as the insertion of membrane proteins, is the use of anchor spacers to form tethered bilayers, as in the case of thiol groups on gold surfaces <sup>[140]</sup>, or alternatively the use of polymeric supports, like poly-ethylene glycol (PEG), whose softness is able to reduce the frictional coupling with proteins protruding domain <sup>[141]</sup>. To overcome the limitations of VF method, lately a solvent-assisted lipid bilayer (SALB) technique has been implemented. Here, vesicles in a water-miscible organic solvent (usually isopropanol) are incubated into a microfluidic channel placed on the substrate. Later, upon the gradual solvent exchange with an aqueous buffer, phospholipids undergo a series of phase transitions leading to the formation of micelles, monomers, and vesicles in the bulk solution, and the rearrangement of deposited lipid molecules to form the lipid bilayer <sup>[142,143]</sup> (**Figure 1.10 B**). The SLB assembly depend on lipid vesicles concentration, where low concentration leads to the formation of SLB islands, while high concentration induce the formation of additional lipid structures protruding from the bilayer surface <sup>[144]</sup>. Furthermore, even the rate of solvent exchange is crucial to guarantee a high-quality bilayer, as high flow rates result in the formation of incomplete SLB because the lipid supply is insufficient.

Of note, SALB technique enable the formation of lipid bilayer on a wide variety of substrates, as graphene <sup>[145]</sup> or gold surfaces where VF failed in assembling SLB with zwitterionic composition <sup>[146]</sup>; additionally, the solvent-exchange procedure allows also the formation of cholesterol-rich bilayers, highly challenging with VF <sup>[147,148]</sup>. Furthermore, the implementation of SALB technique introduced also CPs among possible supports for SLB assembly, where VF presented severe limitations due to the hydrophobic nature of CPs

and the presence of negatively charged dopants <sup>[142,149]</sup>. Such biomembrane-based platforms gained particular attention in bioelectronics as they are able to promote cell-chip interactions, as cells would ideally recognize SLB as part of their native environment ultimately achieving a spontaneous fusion with the synthetic membrane <sup>[97]</sup>. At this purpose, indeed, both VF and SALB are suitable techniques for the functionalization of the bilayer with ECM proteins and biomolecules either embedded within the double layer <sup>[150–152]</sup> or covalently tethered to the lipid headgroups <sup>[142]</sup>. For instance, N-cadherin-functionalized SLB was interfaced with primary neuronal cells to evaluate the role of the synaptic modulator on neurite extension and synaptogenesis <sup>[151]</sup>. However, while embedding single proteins within a SLB is a powerful tool to investigate specific interactions at the interface, this approach is far from replicating the complex structure of actual cell membranes. In this scenario, SLBs can be engineered also with blebs obtained from living cells by chemical treatment <sup>[153]</sup>. The blebbing mechanism is regulated by the mechanical properties of the actin cytoskeleton, whose local contraction leads to the formation, growing and detachment of these quasi-hemispherical protrusions <sup>[154]</sup> (**Figure 1.10 C**). Here, blebs-based SLB enriched with biochemical cues, are able to engage tight contact with living systems as recently proven for cardiomyocytes cells, where the presence of the biomimetic membrane preserves cell-cell interactions and cardiac cell contraction ultimately promoting the formation of a beating tissue <sup>[155]</sup>.

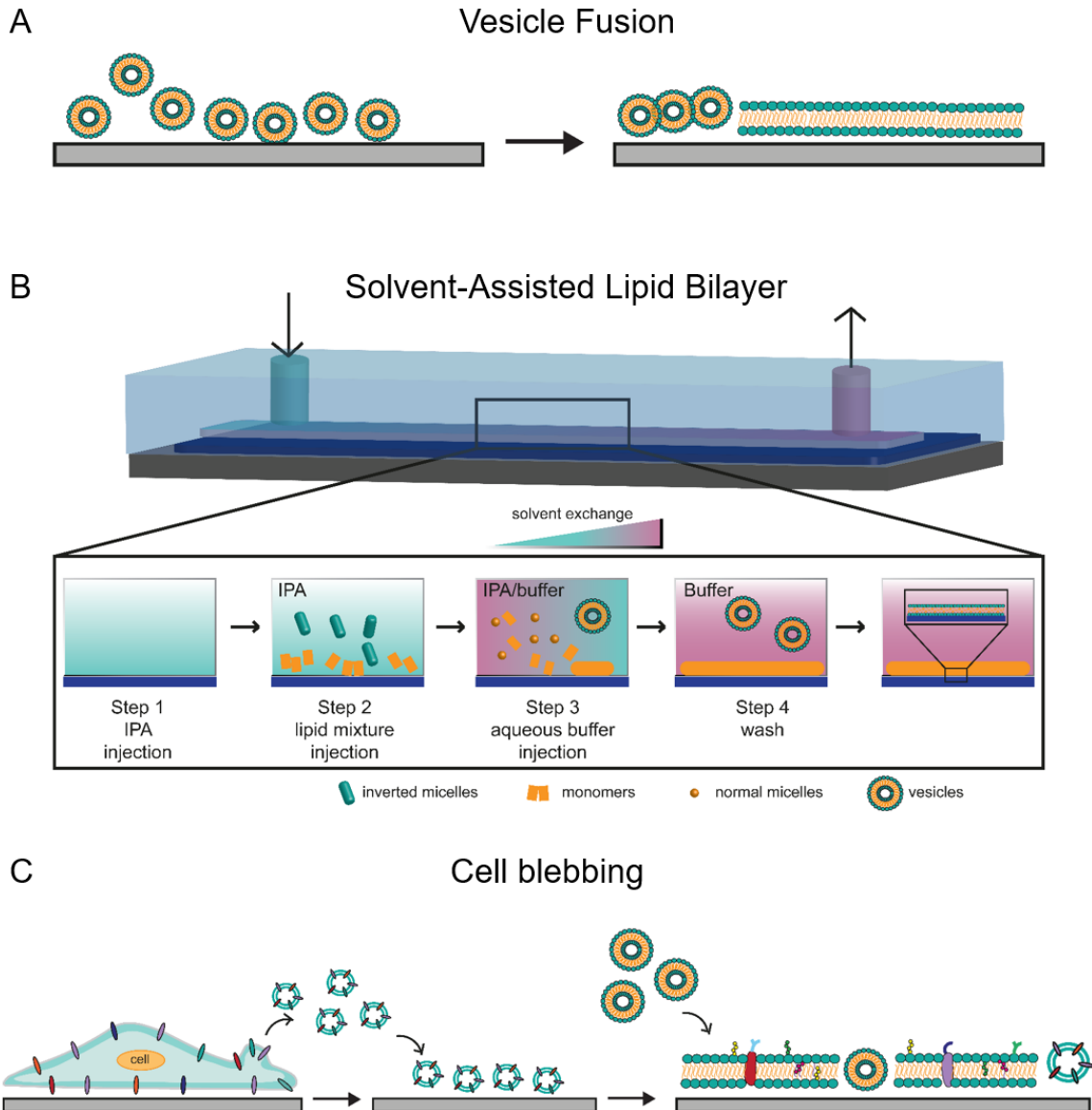


**Figure 1.9. Supported lipid bilayers formation strategies.** Schematic diagrams depicting the possible approaches to obtain artificial membranes. A) vesicle fusion, with vesicles spontaneously fusing on solid supports. B) solvent-assisted lipid bilayer, depicting vesicles rupture induced by solvent exchange within the microfluidic channel: (1) introduction of water-miscible organic solvent. (2) Addition of lipids dissolved in a water-miscible organic solvent (isopropanol). (3) Exchange of the bulk solution with aqueous buffer. (4) Measurement after wash with aqueous buffer to remove excess lipid molecules, resulting in the formation of a single SLB on the underlying solid support. C) Blebbing, illustrating blebs collection from cell plasma membrane and consequent bilayer formation. Adapted from ref. [127].

The possibility to engineer biomembranes on conductive platforms, like gold or CPs, opened up a new scenario in the field of biosensing as these substrates, besides acting as mere support for the SLB, enable the direct monitoring of PM-proteins interactions <sup>[156–158]</sup> and the investigation of pathological mechanisms

impairing lipid membrane integrity <sup>[159]</sup>. Following this approach, recently CPs have been engineered with different models of cell membranes as bacterial and mammalian membranes to investigate the effects of pore forming toxins and antibiotic compounds <sup>[157]</sup>. Furthermore, CP-biomembranes exploiting the mixed ionic electronic conduction of CPs, enable the direct monitoring of embedded proteins activity, as ionotropic receptors, either in their native conformation or upon drug treatments <sup>[160]</sup>. Recently, the possibility to integrate SLBs with OECTs has significantly contributed to the characterization of the behavior of membranes and embedded proteins. Such biomimetic transducer has been employed to study the activity of the TREK-1 ion channel, (*i.e.*,  $K^+$  channel responsible for controlling cell excitability) embedded in a SLB <sup>[161]</sup> (**Figure 1.11**): in presence of a  $K^+$  blocker, the ion channels have a closed conformation that inhibits the passage of ions through the artificial bilayer. The different rate of crossing ions results in a different modulation of the carrier mobility in the CP channel of the transistor <sup>[112]</sup>. This effect is confirmed by the increased  $\tau$  of the OECT. On the other hand, by opening the channels with a TREK-1 activator (arachidonic acid), the ions can freely diffuse through the SLB thus modulating the conductance of the OECT and restoring the initial response time of the device.

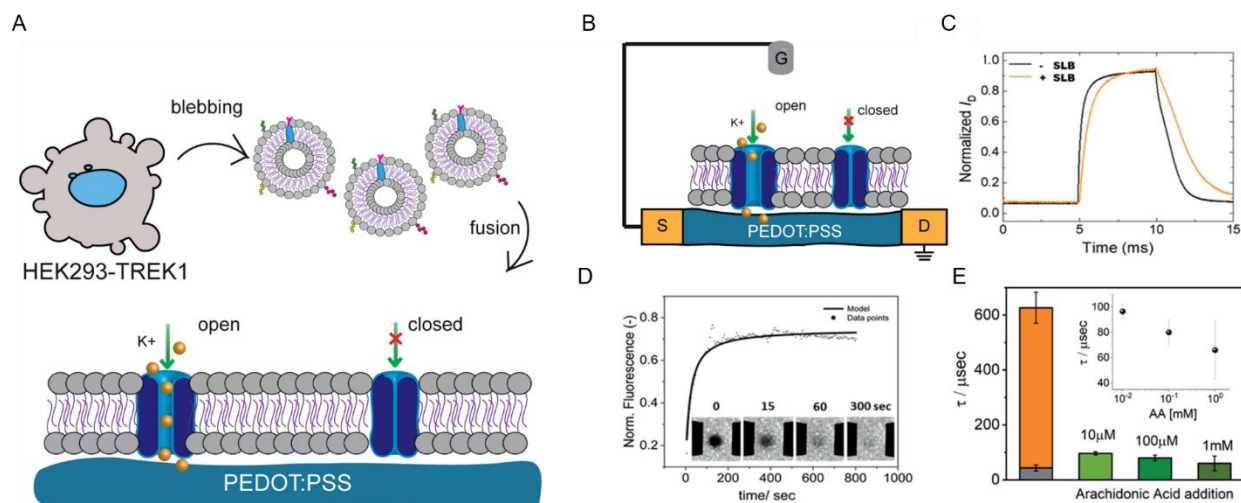


**Figure 1.10. Biomembrane-based OECT.** A) Schematics of vesicle fusion process on PEDOT:PSS using blebs from the HEK-TREK-1 cell line (TREK-1 ion channels are shown in blue). B) Schematics of an OECT device bearing the HEKTREK- 1 membrane. C) Temporal response of the drain current with and without the biomembrane. D) FRAP characterization performed simultaneously with the electrical measurements from the same OECT channel shown in (B). E) Device response time after application of a square gate bias before and after addition of the TREK-1 activator (arachidonic acid, AA). The initial device response is shown in gray, and the bilayer with general  $K^+$  blocker is shown in orange. Green bars corresponds to the addition of AA at 10  $\mu$ M, 100  $\mu$ M, and 1 mM. Inset shows the calibration curve of the device response to different AA concentrations. Adapted from ref. [161].

### 1.4.3 Mimicking the synapse architecture to enhance cell-chip coupling.

Inspired by the shape and geometries found in the ECM with its fibrils, pits and posts, engineered micro- and nanoelectrodes, such as nanoholes, grooves and pillars, have recently emerged as promising candidates for designing biomimetic neurointerfaces <sup>[162–164]</sup>. Indeed, the dynamic behavior of synaptic structures like dendritic spines and filopodia can be exploited to promote engulfment-like events at the cell-material interface, allowing neurons to wrap around purposely designed pseudo-3D electrodes <sup>[165–167]</sup>.

In this context, one of the first attempt to improve cell-chip coupling tuning substrate topography was indeed inspired by dendritic shape and dimensions, leading to the engineering of mushroom-like electrodes: here, the stabilization of the cell-electrode interface is guaranteed by the topography-induced reshaping of the actin cytoskeleton around the stalk of the engulfed microstructure <sup>[162,168–170]</sup>. Furthermore, such tight interface enabled the recording of “intracellular-like” signal, like those achieved with the patch clamp technique <sup>[171–173]</sup> (**Figure 1.12 A**). Similarly, also nanoedges and nanovolcano electrodes, recalling the peculiar morphology of the synaptic cleft where the pre- and post- synaptic terminals are juxtaposed, resulted in a significantly improved electrical seal between neurons and the device itself, also enabling long-term recordings at single neuron resolution <sup>[163,174]</sup> (**Figure 1.12 B**).

Additionally, chemical functionalization with engulfment promoting peptides, such as the fibronectin or laminin-derived peptides, can be used to promote engulfment-like events and induce stronger connection between cells and pseudo-3D electrodes <sup>[167,175,176]</sup>. Besides providing high-resolution neuroelectronic interfaces, engineering the electrode topography has emerged also as valuable strategy to tune neuronal processes at the interface promoting for instance neurite outgrowth, synaptogenesis and network formation <sup>[177]</sup>. Here, for instance grooves and fibers, mimicking the native neuronal ECM structure, can be sensed by filopodia and provide contact guidance for neurite alignment <sup>[178–181]</sup>; similarly, even vertical structures with an interpillar distance equal to 3  $\mu\text{m}$ , have demonstrated the ability to control neurite directionality <sup>[182]</sup>. Interestingly, the efficiency of guidance appeared to be related to the diameter of the axons; axons with 1  $\mu\text{m}$  diameters or more exhibited minor alignment than those with smaller diameters, probably due to mechanical properties and tensile forces that increase with diameter <sup>[183,184]</sup>. However, the neurite response to grooved patterns does not seem to be uniform, as some studies reported neurite elongation in grooves, while others demonstrated neurons affinity for atop ridges <sup>[185,186]</sup>. On the other hand, vertical structures like nanowires and pillars presenting “interrupted” topographical features, have revealed the ability to accelerate neuronal network formation eliciting neuritogenesis, neurite elongation and branching <sup>[187,188]</sup>. Sub-micrometer beads revealed the ability to trigger synaptogenesis, *i.e.*, formation of synapses: here, hippocampal neurons interfaced with the substrate exhibited molecular features that usually exist in pre-synapses like pre-synaptic vesicles and microtubular structures <sup>[189]</sup>.

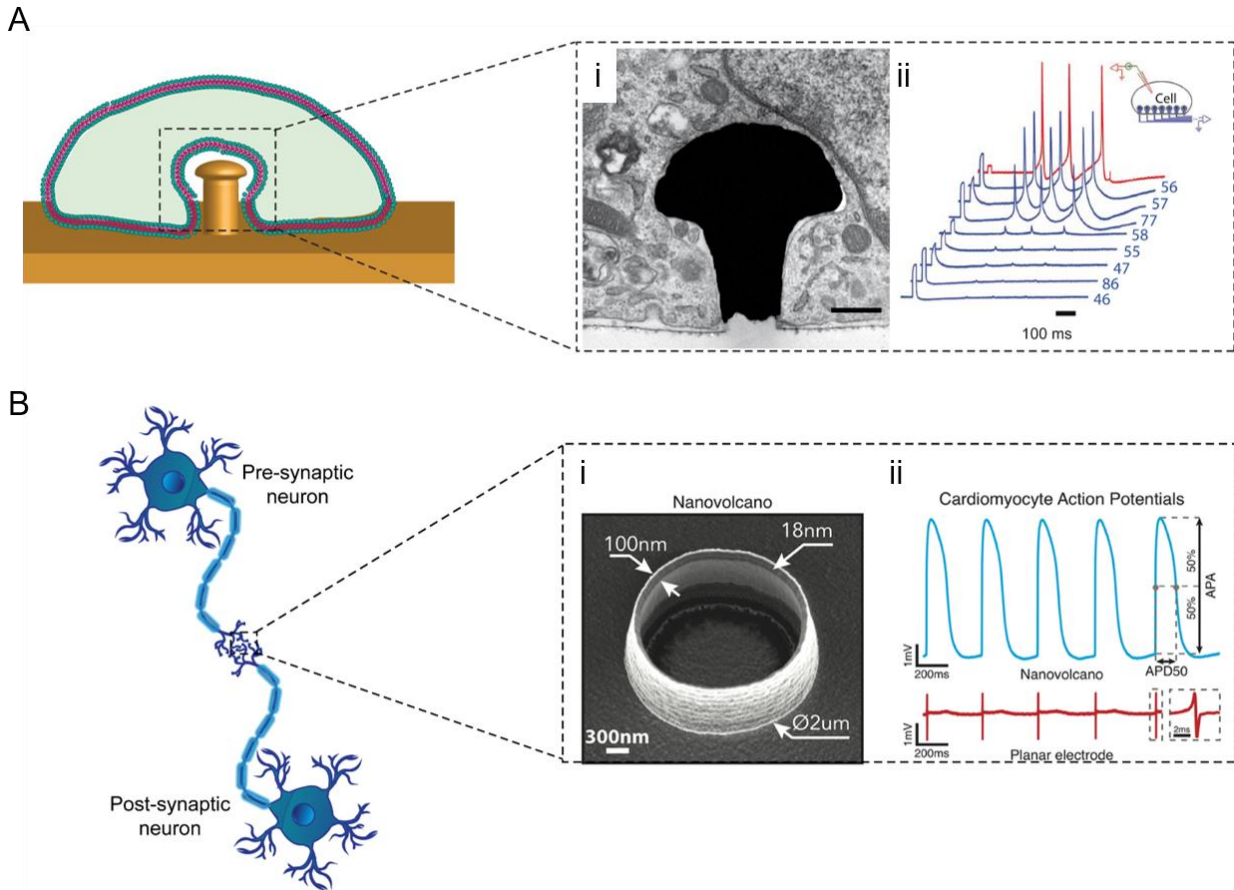


**Figure 1.11. Dendritic spines-inspired 3D structures.** A) Schematic representations of a neuron engulfing a gold-spine electrode. (i) Electron microscopy cross-section of a gold spine engulfed by a PC-12 cell. Scale bar: 500 nm (ii) Simultaneous action potential recordings (blue) from 8 gold-spine electrodes in response to intracellular stimulation of the neuron by a conventional sharp microelectrode (red). Inset, schematic of the experimental setup. Adapted from ref. [173]. B-i) SEM image of nanovolcano microelectrode inspired by the synaptic cleft geometry. B-ii) Comparison between intracellular recording of cardiomyocytes action potentials with a nanovolcano (upper trace) and a planar electrode (lower trace) during spontaneous electrical activity. Adapted from ref. [174].

Although the interface of neuronal cells with micro and nano topographies has been extensively investigated using inorganic platforms, recently, significant efforts were devoted in engineering CPs with pseudo-3D structures to get organic bioelectronics platforms able to combine topographical cues with the intrinsic properties of CPs. Taking advantage of the material composition, CPs can be patterned at the micro and nanoscale as similarly achieved with other polymer-based materials <sup>[190,191]</sup>. In this scenario, diverse patterning approaches (*i.e.*, 3D additive manufacturing <sup>[103,192]</sup>, selective etching <sup>[193]</sup>, femtosecond laser patterning <sup>[194]</sup>, replica molding <sup>[195]</sup>) have been proposed to enhance the cell-chip coupling aiming to create out-of-plane topographies to effectively pin cell membrane domain (**Figure 1.13 A**). Furthermore, a pioneer

work reported the use of CPs to engineer an innovative platform where the polymer is directly polymerized around a living neural tissue [196]: here, the polymer is grown along the ECM structure creating an artificial network tightly interconnected with the biological one (**Figure 1.13 B**). The extensive studies conducted on 3D electrodes for neuroelectronics demonstrated how ‘neuromimetic’ topographies can engage an intimate contact with neuronal tissues, as well as elicit cell processes at the interface enhancing neuritogenesis and synaptogenesis. Such platforms therefore appear as ideal candidates both for *in vivo* applications providing structural support for neuronal cell growth and guiding nerve regeneration during the repair of nerve injuries, but also for *in vitro* systems enabling the investigation of mechanisms underlying the formation of functional neuronal networks.

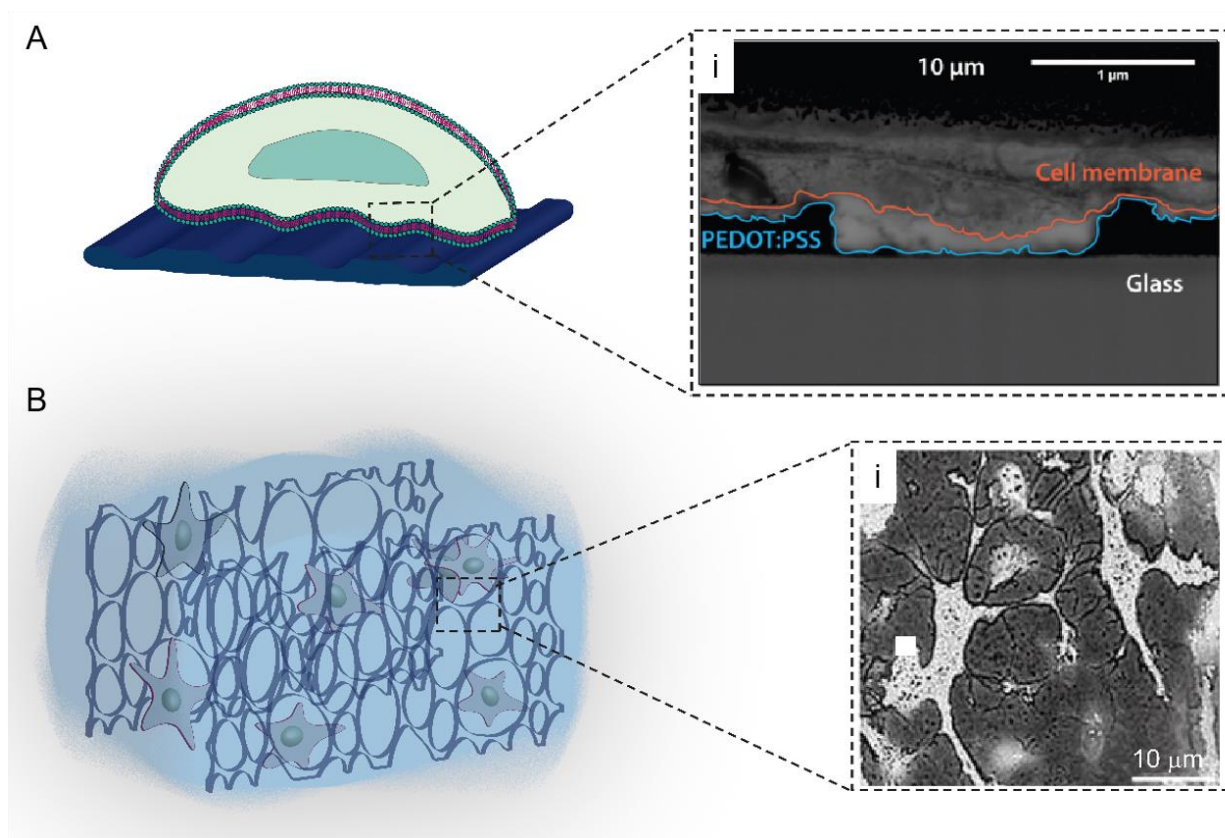


**Figure 1.12. Conductive polymer-based 3D electrodes.** A) Schematics of cell membrane reshaping and local ruffling induced by the grooved PEDOT:PSS substrate: the FIB-SEM cross section highlights the tight interface between HL-1 cell membrane (orange line) and the PEDOT:PSS substrate (blue line). Scale bar: 1 μm. Adapted from ref. (REF). B) Schematics depicting PEDOT:PSS directly electropolymerized around living neurons. i) Optical images of neuron templated PEDOT on Au/Pd electrodes where the tight interface between PEDOT and cells enables the visualization of micro and nano-filopodia. Scale bar: 10 μm. Adapted from ref. [196].

## 1.5 Neuromorphic devices to mimic electrical neuronal functionalities.

As most bioelectronic platforms act as “passive” devices limited to stimulate and record cells activity but without providing any feedback, in the last decade, many researchers have attempted to implement adaptive neuronal interfaces which could represent a tremendous breakthrough in neuroscience field and also in the treatment of neurodegenerative diseases: therefore taking inspiration from the brain, neuromorphic devices were engineered to mimic neuronal functionalities and brain information processing <sup>[197]</sup>. Furthermore, besides biomedical applications, neuromorphic devices found extensive use in brain-inspired computing and contributed to the development of artificial neural networks (ANNs) <sup>[198]</sup>: however, this paragraph will mainly describe the use of neuromorphics as biomimetic *in vitro* platforms which, besides merely monitoring biological signals, are able to provide a bidirectional communication with living systems. Furthermore, particular attention will be addressed on CP-based neuromorphic devices, as they present unique features in terms of Young’s modulus and conduction mechanism (**Paragraph 1.4.1**) which enable efficient biological signal transduction. At this purpose, although different types of artificial neurons were developed with silicon technology, nowadays organic materials gained the leading role in the neuromorphic field, as they offer many advantages compared to inorganic-based devices, especially when it comes to neuroprosthetics and implantable applications <sup>[199–202]</sup>: indeed, organic synapses present high biocompatibility, excellent mechanical flexibility, and small energy consumption, comparable to that of a biological synapse ( $\sim 1\text{--}10$  fJ/synaptic event) <sup>[203]</sup>. Such artificial synapses can be classified as two-terminal devices like organic memristors <sup>[204]</sup>, and three-terminal devices, like electrolyte-gated organic transistors (EGTs) <sup>[205]</sup>. Both categories have proven excellent abilities in mimicking synaptic functionalities such as long and short-term plasticity as well as STDP: just like biological synapses, neuromorphic devices have the ability to modify their conductive state upon an external stimulation, and retained this altered state over long time according to the history of the applied stimulation <sup>[206]</sup>.

### 1.5.1 Two-terminal neuromorphic devices.

Memristors, resistive-switching devices consisting of two metal electrodes and a switching layer in between, exhibit continuously adjustable resistive states: therefore, unlike other devices displaying only a bistable change between ON (high resistance) and OFF (low resistance) states, memristors can provide volatile and non-volatile memory <sup>[207]</sup>. The latter, necessary to store information, is enabled by the ability of the switching layer to retain the resistive state even after removal of the applied switching stimuli (*i.e.*, electricity, light, heat) <sup>[208]</sup>. In case of CP-based memristors, the conductivity of the organic semiconductor is tuned by an external electric field, and depends on the concentration and mobility of the charge carriers <sup>[209]</sup>: here, several mechanisms have been proposed to explain polymer conductance changes as donor-

acceptor charge transfer, charge trapping due to redox reaction, and modulation of dopant in conjugated polymer [210–212]. Furthermore, according to the chemical structure of the polymer, different memory and switching mechanisms can be achieved: for instance, in case of conjugated polymers, presenting electron donor and acceptor macromolecules, and non-conjugated polymers, displaying functional side chains, charge transfer can be induced to achieve memory effect [213]. On the other hand, polymer composite can present multiple switching mechanisms: for instance, in case of poly(3,4-ethylenedioxythiophene) polystyrene sulfonate (PEDOT:PSS), where the introduction of PSS into PEDOT matrix enhances the polymer conductivity by proton doping, the resistive change has been correlated both to the redox reaction, which reduces PEDOT<sup>0</sup> to PEDOT<sup>+</sup>, and to the phase separation of PSS regions [214]. PEDOT:PSS has been often presented as the new golden standard for neuroelectronic interfaces thanks to its biocompatibility, electronic-ionic conductivity, commercial availability, flexibility, and optical transparency, and indeed even the neuromorphic field embraced this new trend as multiple devices exhibit PEDOT:PSS as active layer [215].

For instance, an all polymer-based memristor was fabricated using PEDOT:PSS both as switching layer and electrodes [216]. In detail, commercial PEDOT:PSS film (conductivity: 1–3 S/cm) is used as active layer, while highly conductive PEDOT:PSS (conductivity > 900 S/cm), prepared by addition of dimethyl sulfoxide (DMSO), replaces the metal electrodes: here, the voltage applied triggers the accumulation of PSS-chains at the electrode/polymer interface with consequence switch from the initial low-resistance state (ON state) to the high-resistance one (OFF state); interestingly, the device exhibited long memory retention (> 10000 s) and good stability over 3 months. Furthermore, PEDOT:PSS-based neuromorphic devices were lately used to implement an artificial synapse where PEDOT:PSS, partially reduced with poly(ethylenimine) (PEI), was used as post-synaptic electrode interfaced with a PEDOT:PSS pre-synaptic terminal *via* a Nafion electrolyte [217] (**Figure 1.14**). In detail, the application of a positive voltage at the pre-synaptic electrode induces the injection of cations into the post-synaptic terminal reducing the amine: here, the protonated PEI partially compensate the negative charges of PSS<sup>-</sup>, consequently reducing PEDOT and resulting in a decreased polymer conductivity; such reaction can then be reversed applying a negative voltage at the pre-synaptic electrode (**Figure 1.14 A**). In addition, the Nafion electrolyte acts also as barrier to ensure the retention of the electrode conductance state after the pre-synaptic stimulus is applied, and indeed the device is able to emulate some of the synaptic functions like short-term potentiation (STP) and paired pulse facilitation (**Figure 1.14 B, C**).

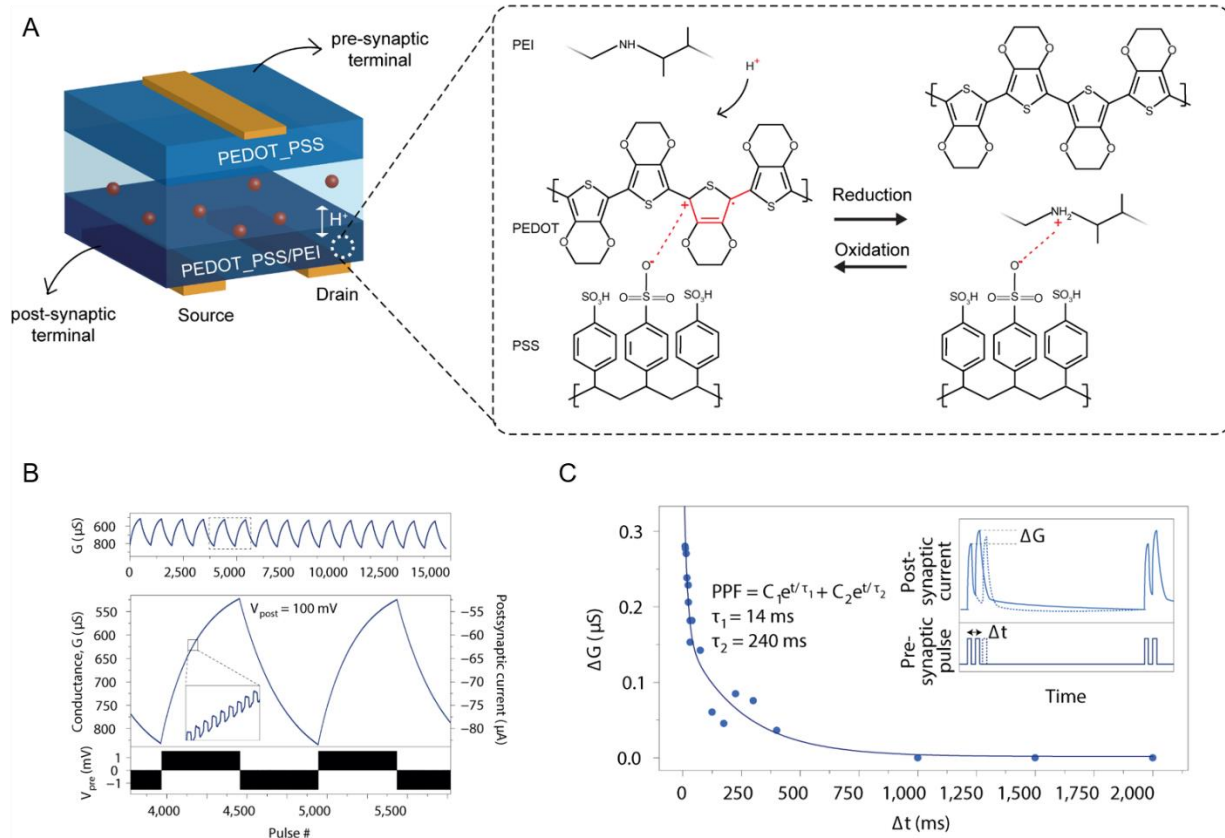


**Figure 1.13. Synaptic plasticity in organic memristors.** A) Schematics of the PEDOT:PSS-based two-terminal device where the amine (PEI)-dedoped layer acts as post-synaptic terminal while the PEDOT:PSS film emulate the pre-synaptic end; the synaptic cleft is represented by an electrolyte layer transporting ions/protons (red spheres). Here the application of a positive bias at the pre-synaptic terminal drives protons into the postsynaptic electrode, which results in the compensation of some negative charges of PSS by the protonated amine. This reaction causes the reduction of PEDOT in the same electrode due to charge neutrality, which eliminates a polaron (in red) and decreases the polymer conductivity. The reaction is reversed upon applying a negative bias at the pre-synaptic terminal. B) Long-term potentiation and depression of the organic memristor following the application of voltage pulses. The inset is a zoom-in showing the individual states. C) STP and paired pulse facilitation elicited by voltage pulses with varying time interval ( $\Delta t$ ) between two short pulses, as shown in the inset. Adapted from ref. [217].

### 1.5.2 Three-terminal neuromorphic devices.

CPs found extensive application as active layer also in EGTs, three-terminal devices where the presence of an additional third-gate electrode enables low-energy neuromorphic operations [218]. In detail, EGTs are based on a semiconducting channel connected to the gate electrode *via* an ionic conducting and electronic insulating electrolyte, which can be either liquid or solid. These devices present an architecture very similar to biological synapses, where the gate electrode resembles the pre-synaptic neuron, the electrolyte can be considered as the synaptic cleft, while the semiconductor channel acts like post-synaptic neuron: therefore

the channel conductivity can be considered as the equivalent of the biological synaptic strength. In general, EGTs use ions in the electrolyte to modulate the channel conductance, although they can exhibit two different operation mechanisms based either on electrostatic modulation or on electrochemical doping <sup>[219]</sup>. In case of electrostatic modulation, the application of a gate voltage lower than the threshold value (*i.e.*, the minimum gate voltage needed to allow a minimum flow of current inside the channel,  $V_T$ ), induces the migration and accumulation of ions at the gate/electrolyte and the semiconductor/electrolyte interfaces. For instance, upon the application of a positive gate voltage ( $V_g < V_T$ ), anions from the electrolyte migrates at the gate/electrolyte interface; at the same time, cations will accumulate at the electrolyte/semiconductor interface. The so-formed electric double layer (EDL), which acts like a capacitor, induces the accumulation of electrons inside the semiconductors at the solid part of the interface, therefore varying the voltage applied at the gate, the channel resistance can be modulated varying the number of charges accumulated at the semiconductor side of the interface <sup>[220]</sup>. However the electrostatic operation mechanism elicits only a volatile memory as the channel conductance modulation is temporary: indeed, once the gate voltage is removed the EDL will disappear in few seconds and the semiconductor recovers its initial conductive state. On the other hand, when the EGT operates in electrochemical doping mode, the channel conductance changes are non-volatile, and therefore these devices can simulate also the long-term memory of biological synapses <sup>[205]</sup>. EGT operating in electrochemical mode are called electrochemical transistor (ECT) and present a ion permeable semiconductor channel, therefore here the application of a gate voltage higher than the threshold ( $V_g > V_T$ ) induces the injection of small ions (*i.e.*  $H^+$ ,  $Li^+$ ) into the bulk of the semiconductor material changing its doping level and therefore modulating its conductance <sup>[221,222]</sup>. As the operation of ECTs involves the entire volume of the semiconductive film, here small changes in the gate voltage induce large modulation of channel current, making ECTs powerful amplifiers <sup>[223]</sup>.

Among different channel materials investigated in ECTs, organic semiconductors received increasing attention thanks to their biocompatibility, low fabrication cost, flexibility and low power consumption <sup>[217,224–228]</sup>: here, according to the type of polymer (n-type or p-type), the OEECT can operate either in accumulation or depletion mode. The latter is observed in PEDOT:PSS-based OEECTs, a p-type polymer where the PEDOT conjugated backbone represents the redox active moiety responsible for the electronic transport, while the negatively charged insulating PSS domains are responsible for the ionic conduction <sup>[229,230]</sup>. PEDOT:PSS can undergo to electrochemical redox reaction switching between the conducting (oxidized)  $PEDOT^+$  to the insulating (neutral)  $PEDOT^0$ . Here, the application of a positive bias at the gate electrode, drives cations from the electrolyte into the bulk of the organic semiconductor, neutralizing the sulfonic acid groups of PSS, while  $PEDOT^+$  is reduced to  $PEDOT^0$ : such electrochemical de-doping induces the polymer switching to a less conductive state and therefore the conductance of the OEECT channel is decreased <sup>[231]</sup>. The doped/dedoped states of PEDOT:PSS were exploited to mimic synaptic functionalities,

like STP<sup>[232]</sup> (**Figure 1.15**): indeed, applying positive pre-synaptic voltage pulses at the gate electrode, cations from the electrolyte induce the de-doping of the neuromorphic PEDOT:PSS channel inducing decrease in OECT conductance and an inhibitory post-synaptic current. Removing the bias from the gate instead, allows cations to return into the electrolyte therefore restoring the doped state of the polymer with consequence recovery of initial high conductive state: such reversible conductance modulation recalls the short-term depressive behavior of biological synapses. Furthermore, the application of two consecutive pulses at the gate emulates the paired-pulses depression: here tuning the time interval between pulses modulates the channel conductance (*i.e.*, synaptic strength) with high frequency pulses inducing higher conductance decrease (*i.e.*, enhanced depressive behavior). The neuromorphic functions of OECTs indeed depend also on its response time ( $\tau$ ), which describes the ability of the device in switching from the doped (ON-state) to the de-doped state (OFF-state) and *vice versa*<sup>[233]</sup>: therefore, if the time interval between two consecutive pulses is equal or shorter than  $\tau$ , the OECT retains memory of the first pulse for a certain period of time.

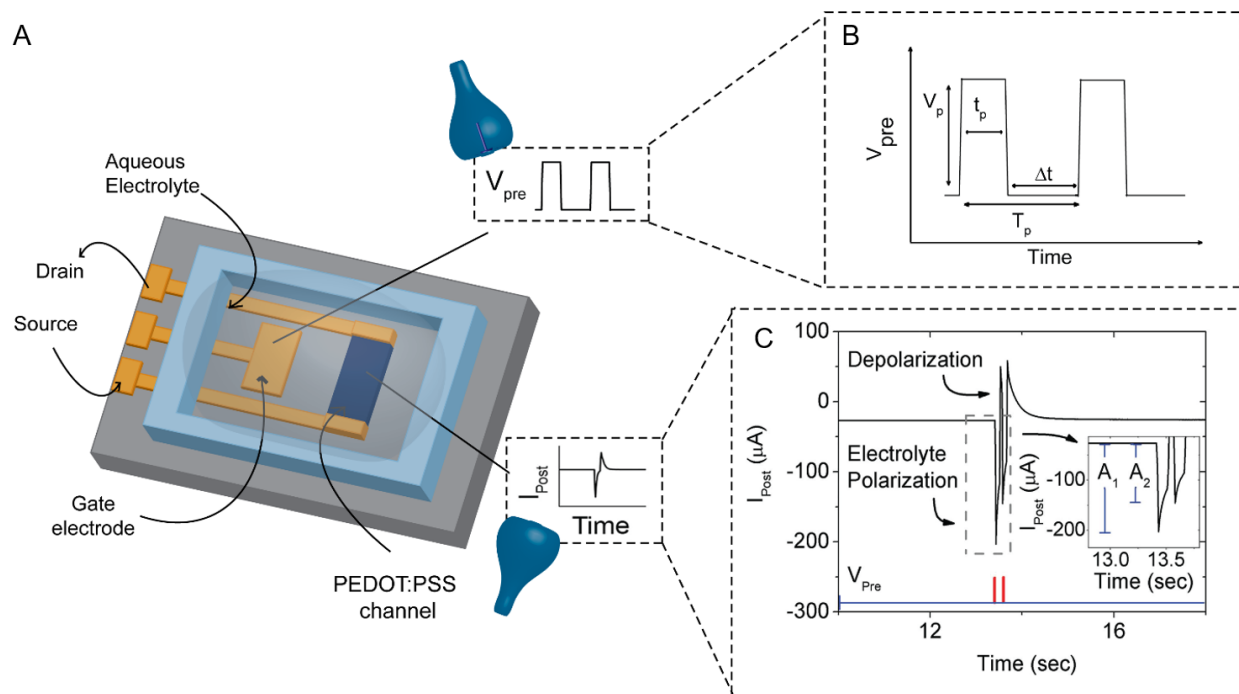


**Figure 1.14. Short-term plasticity in PEDOT:PSS-based OECT.** A) Schematics of the three-terminal OECT where the gold electrode acts as pre-synaptic neuron while the PEDOT:PSS channel emulates the post-synaptic end. Here, paired-pulses depression (PPD) can be emulated applying a pair of voltage pulses ( $V_{pre}$ ) at the gate electrode (recalling biological pre-synaptic stimuli) while monitoring the post-synaptic channel current ( $I_{post}$ ). B) Distinctive features of the pre-synaptic stimulus characterized by the pulse amplitude ( $V_p$ ), pulse duration ( $t_p$ ) and time interval between pulses ( $\Delta t$ ). C) Modulation of the post-synaptic current induced by the application of two consecutive pulses at the gate: the depressive behavior depends on the time interval between pulses. Adapted from ref. [232].

As the ions injection/extraction in the semiconductor channel is a reversible process, the emulation of the long-term plasticity with OECTs is very challenging <sup>[234]</sup>. For instance, modifying the electronic structure of the neuromorphic channel enabled the non-volatile conductance tuning <sup>[235]</sup> as observed in case of the poly(3,4-ethylenedioxythiophene):tosylate (PEDOT:Tos)/ Polytetrahydrofuran (PTHF) composite where the application of a sequence of gate voltage pulses with high amplitude ( $V_g = 0.7$  V) induced a long-term conductance modulation <sup>[236]</sup>, as the reduction process causes conformational changes in the polymeric structure and only with a reverse bias the organic semiconductor can recover its initial structure and conductivity <sup>[237]</sup>. Alternatively, even the use of physical barriers limiting the ions movement have successfully improved the long-term features of OECT synapses, as lately observed for a PEDOT:PSS-based neuromorphic device presenting a Nafion membrane between the gate and the channel: such cations exchange membrane enhances the retention of  $\text{Na}^+$  ions into the PEDOT:PSS channel therefore enabling the long-term conductance modulation <sup>[238]</sup> (**Figure 1.16**).

Furthermore, the chemical modification of PEDOT:PSS structure with additive molecules can shift the operation mode of the OECT from depletion to enhancement mode: recently indeed aliphatic polyamine have demonstrated the ability to de-dope PEDOT:PSS to a very low conductive state, due to electron and proton transfer reactions <sup>[239]</sup>: here the application of a gate voltage higher than the threshold (where  $V_T$  now is shifted towards negative values) switches the polymer from the initial low conductive state (dedoped OFF state) to a more conductive one (doped ON state) <sup>[240]</sup>. Finally, the modification of the PEDOT backbone with an alchyl side chain ending with a sulfonate group (similar to the PSS structure), provided an hybrid OECT where the active channel is able to operate both in depletion and accumulation mode as the sulfonate groups is insufficient to fully dope the polymer <sup>[241]</sup>. In fact, the application of a negative voltage at the gate induces the penetration of anions into the bulk of the channel volume and the simultaneous extraction of cations which compensate the charge on the sulfonate group: such ionic doping therefore results in increased channel conductance (accumulation mode) while the application of a positive bias causes a decrease in channel current (depletion mode). Of note, upon the application of consecutive pulses at the gate, such neuromorphic device is able to emulate both synaptic potentiation and depression depending whether anions are accumulated or depleted from the channel.

Lately, the short-term plasticity of a PEDOT:PSS-based OECT was also modulated by the addition of dopamine in the electrolyte solution: here, the neurotransmitter present in its cationic form at the operational pH (7.2), establish strong electrostatic interactions with negatively charged PSS domains placed at the surface of the PEDOT:PSS channel, therefore the ionic movement in and out PEDOT:PSS exhibits a slower dynamics and induces short-term plasticity with longer timescale compared to the one obtained in presence of other metabolites <sup>[242]</sup>.

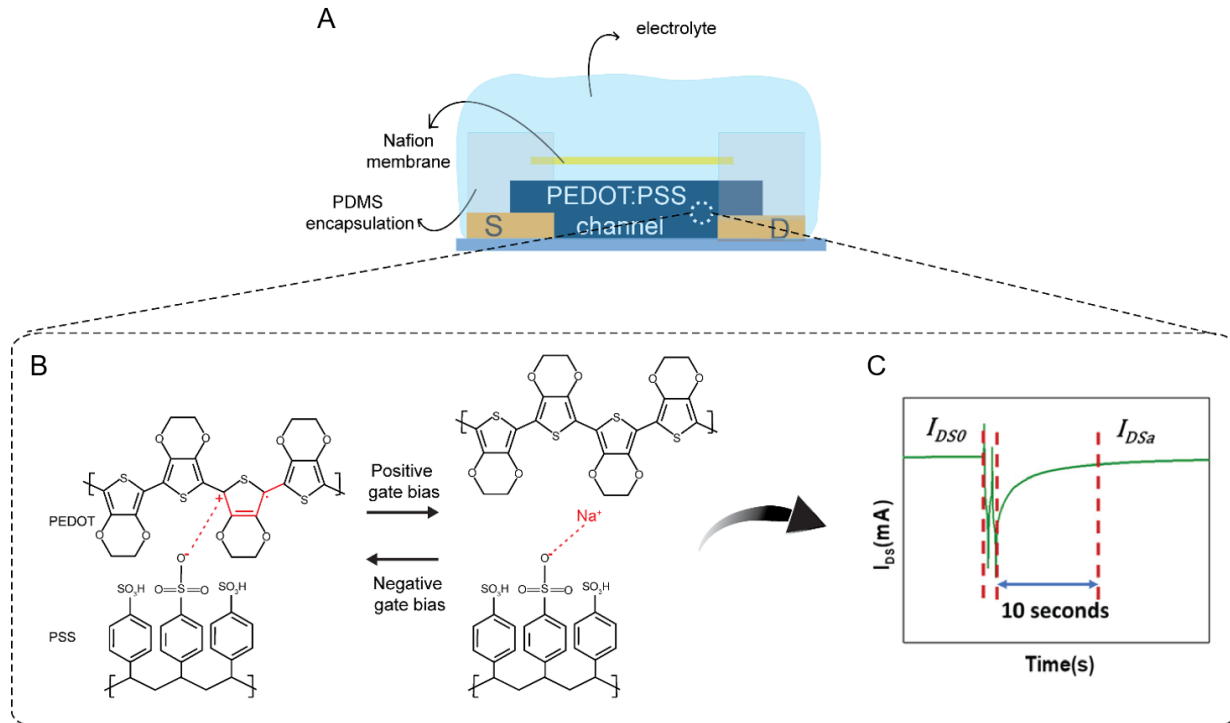


**Figure 1.15. Long-term plasticity in PEDOT:PSS-based OECT.** A) Schematics of the OECT structure with a Nafion membrane placed above the PEDOT:PSS channel by means of PDMS supports. B) Mechanism of doping/de-doping process of the neuromorphic channel: the application of a positive bias at the gate electrode pushes cations ( $\text{Na}^+$ ) from the electrolyte into the PEDOT:PSS film inducing the de-doping of the polymer and decrease of its conductivity. Such process can be reversed applying a negative voltage at the gate. Of note, the presence of the membrane makes the  $\text{Na}^+$  ions transport into and out of the channel sluggish, therefore enhancing the conductance modulation of the OECT. C) Output channel current showing the initial value  $I_{DS0}$  (before gate pulsing) and the final current  $I_{DSa}$  measured 10 s after removal of gate pulsing. Adapted from ref. [238].

### 1.5.3 Towards biohybrid neurointerfaces.

Since both memristors and EGTs proved excellent capability of mimicking synaptic plasticity, in the last decade great efforts were addressed to interface such neuromorphic devices with biological cells. To this end, an organic memristor was used as artificial synapse to connect through an electronic circuit two live neurons, where the artificial synaptic strength (*i.e.*, memristor resistance) was regulated by the neuronal activity<sup>[243]</sup> (**Figure 1.17 A-C**). On the other hand, EGTs (in particular OECTs) have been directly coupled with biological cells although the neuromorphic device was mainly used as biosensor to monitor biological processes, as cell adhesion and proliferation<sup>[244]</sup> but also more complex mechanisms as the formation and disruption of tight junctions in cell-barrier tissues<sup>[245]</sup>. Here cells seeded on the neuromorphic channel act as a barrier to the passage of ions therefore causing an increase in the OECT response time ( $\tau$ ); on the other

hand, the disruption of tight junction proteins, through the ethanol-induced poration within the cell layered, enabled the complete recovery of the initial  $\tau$  (**Figure 1.17 D**).

Although neuromorphic devices have extensively demonstrated the ability to emulate the learning process of neurons, these artificial synapses still lack biomimetic features such as neurotransmitters receptors and post-synaptic regulators which could recapitulate the same architecture of biological synapses promoting the seamless integration of organic neuromorphic devices within the neuronal network.

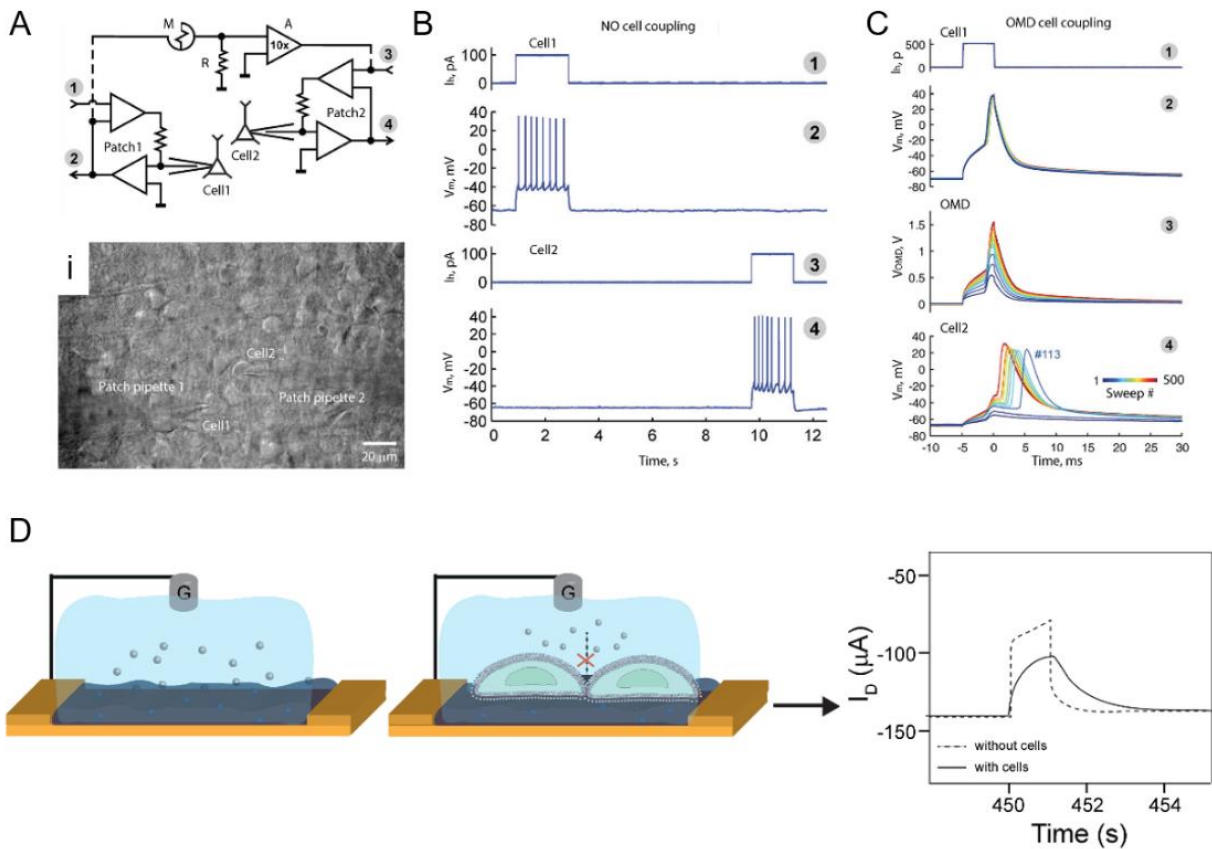


**Figure 1.16. Hybrid neuronal networks.** A) Electrical scheme of two patch-clamp amplifier headstages used to connect an organic memristor to biological neurons: 1,3—patch-clamp holding inputs; 2,4—patch-clamp primary outputs. i) Infrared differential interference contrast microphotograph of a rat brain slice with visually identified L5/6 neocortical cells (Cell1,2) recorded simultaneously. Scale bar: 20  $\mu\text{m}$ . B,C) Traces of current-clamp recordings from cells 1 and 2 before (B) and after (C) organic memristor-coupling. Adapted from ref. [243]. D) Electrical modulation of an OECT response mediated by cell monolayer formation: the presence of tight junctions inhibits ionic flow into the neuromorphic channel therefore enhancing the time response of the device. Adapted from ref [245].

## 1.6 Our study.

The aim of this PhD thesis is to engineer biohybrid biomimetic synapses to implement a new class of adaptive *in vitro* platforms for the investigation of neuronal processes. In particular, the learning core of the neuromimetic system is provided by a PEDOT:PSS-based OECT, whose neuromorphic features make it an ideal candidate to emulate neuronal functionalities. In the first part of the project the OECT was directly interfaced with biological cells to engineer a biohybrid platform where the device act as post-synaptic terminal, while cells represent the pre-synaptic end. Here, the neuromorphic device exhibited a chemically specific resistance-based adaptation mechanism that mimics the behavior of a biological synaptic cleft. In detail, in response to dopamine oxidation the device is able to modulate its conductivity and retain this altered state over time, emulating in this way the short and long-term neurotransmitter-mediated plasticity of biological neurons. The subsequent coupling of the artificial synapse with a dopaminergic cell line provided a hybrid system where cells stimuli (*i.e.*, dopamine release) modulate the synaptic strength (*i.e.*, OECT conductance) of the neuromorphic platform, demonstrating for the first time the adaptive behavior of neuroelectronic devices in response to biological signals. Although displaying the same memory capabilities of the nervous system, the biohybrid synapse still lack biomimetic feature which could resemble the same learning mechanism of neuronal cells, where chemical synapses modulation involves neurotransmitter receptors and ion channels at the post-synaptic terminal to enable the propagation of the action potential. For this reason, the second part of the project was focused on engineering a biomimetic artificial synapse coupling OECT with SLBs resembling the native composition of cell membrane. In particular, as first proof of concept a fluid homogenous bilayer was assembled on the surface of the neuromorphic device. Later, the role of the synthetic membrane on the OECT short-term plasticity was investigated, varying also the position of the gate electrode in respect to the neuromorphic channel. Here, the membrane acting as In ionic barrier hinders the passage of ions from the gate towards the channel therefore enhancing the short-term plasticity and acting as modulator of the synaptic strength in the artificial synapse. The adaptive behavior exhibited by the biomembrane-based OECT, confirms these biomimetic devices as a valuable strategy to mimic the physiological mechanisms of the nervous system in *in vitro* platforms which could contribute to unwind the complex processes underlying neurodegenerative disorders.

## 2 Materials and Methods

### 2.1 Fabrication of the artificial synapse for the dopamine-mediated biohybrid interface.

The OECT was fabricated in collaboration with the Salleo research group at the Department of Materials Science and Engineering of Stanford University (USA), by means of a photolithographic technique on a silicon wafers with 200 nm thermal oxide following a previously reported procedure <sup>[246]</sup> (**Figure 2.1 A**). First of all, the gold interconnects (contact pads, feedlines, gate, source and drain electrodes) were obtained using a standard lift-off process where 100 nm of gold (Au) were deposited on a 5 nm layer of titanium (Ti) to enhance the adhesion of Au on the silicon wafer (**Figure 2.1 A-i**). Then the substrate was coated with an insulating layer of 1.5  $\mu\text{m}$  of [poly(para-chloroxylylene)] (Parylene-C), which was chosen not only for its dielectric barrier properties but also because of its stability in physiological conditions and its biocompatibility. Parylene-C was crosslinked using 3-(trimethoxysilyl)propyl methacrylate to promote adhesion to the wafer. Following the first Parylene-C layer, a dilute soap (3% Micro-90 in deionized water) solution was spin-cast on top forming a thin layer that acts as an anti-adhesive, followed by deposition of a second Parylene-C layer, later used as a peel-off layer (**Figure 2.1 A-ii**). The wafers were then coated with 75 nm of Ti using an e-beam evaporation process, photolithographically patterned and dry etched to define the neuromorphic channel and gate areas (**Figure 2.1 A-iii**). The wafer dies were cleaned with isopropanol sonication followed by UV-ozone cleaning before spin-coating the polymer layer. PEDOT:PSS aqueous solution was prepared by adding 6 vol% ethylene glycol to increase the PEDOT:PSS conductivity <sup>[247]</sup>, 0.1 vol% dodecylbenzene sulfonic acid (DBSA) as a surfactant <sup>[248]</sup>, and 1 vol% (3-glycidyloxypropyl)trimethoxysilane (GOPS) as a crosslinking agent to improve mechanical stability <sup>[249]</sup>. PEDOT:PSS solution was spun on the wafer die at 1000 round per minute (RPM) for 2 minutes and annealed at 120 °C for 20 minutes (**Figure 2.1 A-iv**). The top Parylene-C layer was then peeled off to retain PEDOT:PSS only in the photolithographically defined neuromorphic channel and gate areas (**Figure 2.1 A-v**). The wafer dies were gently rinsed in deionized water to eliminate residual soap and were subsequently dried at 120 °C for 5 minutes. The OECT was then coupled with a PDMS microfluidic channel prepared using a photolithographically patterned mold in SU-8 (ca. 1 mm thick) on a undoped silicon wafer. PDMS is mixed with a crosslinker in a ratio of 10:1 wt./wt. and degassed in a vacuum chamber before pouring onto the wafer containing the mold and heated to 80 °C for 3 hours to cure. A 1.2 mm diameter biopsy punch is used to create the holes for the two inlets and the outlet which consist of Teflon tubing (0.813 mm outer diameter, 1.32 mm outer diameter). A small amount of uncured PDMS is used to stick the bottom surface of the PDMS microfluidic channel onto the neuromorphic device, and subsequently baked at 80°C for 1 hour (**Figure 2.1 B**).

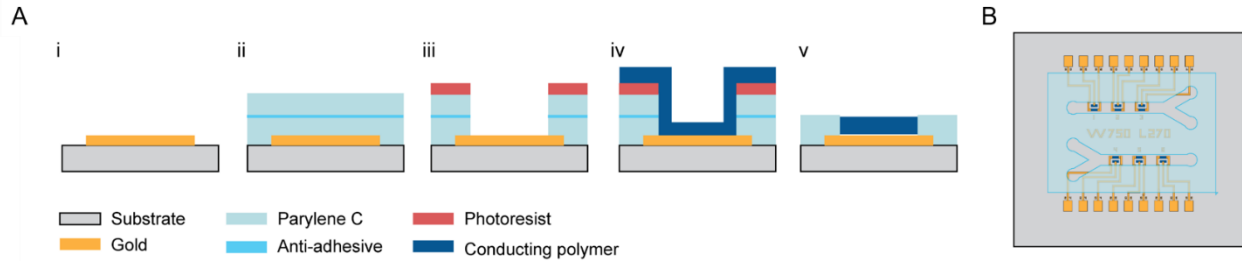


**Figure 2.1. OECT architecture for the biohybrid synapse.** A) Schematic depicting the main steps of the photolithography-based process to obtain the PEDOT:PSS based OECT. Adapted from ref. [246]. B) Layout of OECT and PDMS microfluidic channel.

## 2.2 Fabrication of the artificial synapse for the lipid bilayer-based biomimetic platform.

The organic electrochemical transistor was fabricated by means of a dry etching procedure (**Figure 2.2**) using customized glass substrates (25 x 25 mm) with four squares (10 x 10 mm) of Indium Tin Oxide (ITO) at each corner which act as contact pads for the gate and the neuromorphic channel. The substrates were treated with oxygen plasma for 2 minutes at 20 W. PEDOT:PSS aqueous solution was prepared by adding 5 vol% ethylene glycol, 0.02 vol% DBSA, and 1 vol% GOPS. Subsequently the PEDOT:PSS solution was spun on the glass substrates at 2000 RPM for 2 minutes and annealed at 140 °C for 20 minutes (**Figure 2.2 A-i**). The PEDOT:PSS gate and channel were patterned through oxygen plasma dry etching technique performed for 15 minutes at 100 W (**Figure 2.2 A-ii**): here, in order to define the gate and channel electrode area, the spin-coated PEDOT:PSS film was masked with polydimethylsiloxane (PDMS) physical masks, obtained mixing the elastomer with its curing agent in a ratio 10:1 wt./wt. and then cured at 80 °C for 3 hours. The etching procedure returns an OEECT with two symmetrical PEDOT:PSS stripes 7x17 mm wide, 2 mm apart (**Figure 2.2 A-iii**). The devices were then immersed in milli-Q water for 1 hour to allow the swelling of the PEDOT:PSS film. The OEECT was then coupled with a PDMS microfluidic channel prepared using a micro-milling patterned mold 17 mm long, 4 mm wide and 0.4 mm thick. PDMS is mixed with a crosslinker in a ratio of 10:1 wt./wt. and degassed in a vacuum chamber before pouring onto the mold and heated to 80 °C for 3 hours to cure. A 1.2 mm diameter biopsy punch was used to create the holes for the inlet and the outlet which consist of Teflon tubing (0.813 mm outer diameter, 1.32 mm outer diameter, **Figure 2.2 B**).

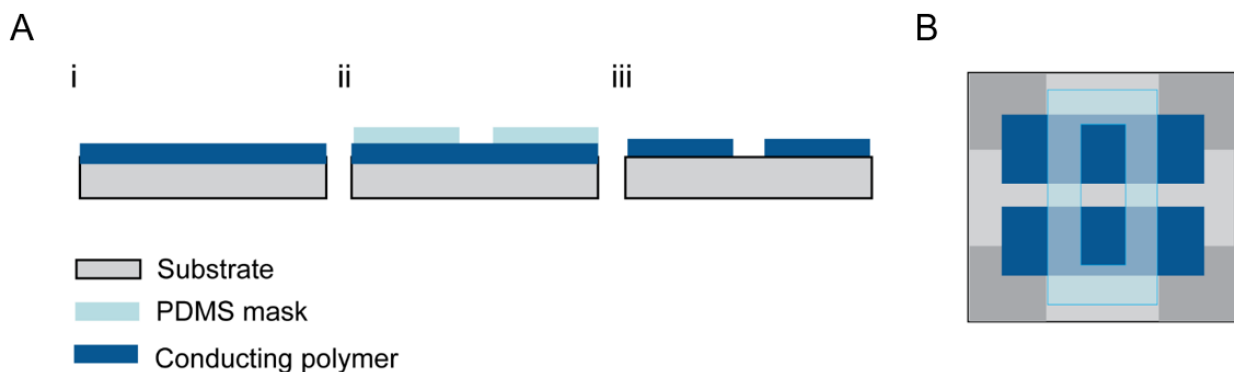


**Figure 2.2. OEECT architecture for the biomimetic synapse.** A) Fabrication process of the dry etching procedure employed to pattern the large PEDOT:PSS OEECT. B) Layout of OEECT and microfluidic channel.

### 2.3 Electrical characterization of the organic neuromorphic devices.

Neuromorphic devices were characterized using a commercial platform (ARKEO) composed by a thermal controlled stage, two-channel source meter units and two synchronized microfluidic pumps. Spring contact probes were used to access the gate and drain electrodes. Furthermore, for the implementation of the lipid bilayer-based biomimetic synapse a top gate configuration was also investigated: here, the neuromorphic device is made of two OECTs sandwiched together: the one placed on the bottom constitutes the neuromorphic channel, while the one on top, contacted with a wired probe, was used as gate electrode. The electrical measurements were performed using different electrolytes (*i.e.*, cell medium, Tris(hydroxymethyl)aminomethane buffer (TRIS)-NaCl). The characteristic curves (transfer and output) were taken by sweeping the gate voltage from 0.8 V to -0.2 V and the channel potential from -0.6 V to 0.1 V. The neuromorphic operation was investigated applying a pulsed voltage at the gate electrode ( $V_{\text{gate}} = +0.3$  V, variable PW and  $\Delta t$ ) while monitoring the output channel current at a fixed potential ( $V_{\text{ch}} = -0.2$  V).

## 2.4 Calibration with dopamine of the artificial post-synaptic device.

### 2.4.1 Characterization of the electrochemical oxidation of dopamine.

The electrochemical oxidation of dopamine on the PEDOT:PSS electrode was characterized by means of cyclic voltammetry (CV), a versatile electroanalytical technique used to study electroactive species and electrochemical reactions. Such electrochemical measurement employs a three-terminal potentiostatic setup and is based on the scan of the potential of the working electrode (WE) in cyclic phases. The potential is measured between the working and the reference electrode, while the resulting current is measured between the working and the counter electrode. One of the crucial parameter for the analysis is the scan rate (volt per second): faster scan rates result in higher and broader current peaks, whereas lower scan rates decrease the current intensity but provide well-resolved redox peaks <sup>[250]</sup>. Here, an Autolab PGSTAT302N potentiostat/galvanostat interfaced with a personal computer, equipped with the NOVA software, was used for the electrochemical characterization. The postsynaptic PEDOT:PSS electrode was used as working electrode, while a saturated Ag/AgCl and a platinum (Pt) wire were employed as reference and counter electrodes, respectively. Dopamine solutions were prepared immediately before measurements to avoid degradation due to UV exposure <sup>[251]</sup>, by dissolving dopamine hydrochloride into cell culture media (pH= 7.2-7.4, **Paragraph 2.6**) at a concentration of 1 mM; the stock solution was then diluted to obtain dopamine solutions at different concentrations (20-500  $\mu$ M). For all solutions the current of the WE was measured while scanning the potential between -0.2 V and 0.6 V at a scan rate of 10 mV/s.

### 2.4.2 Investigation of the dopamine-mediated neuromorphic behavior.

To monitor the OECT response to oxidation of increasing dopamine, the concentration of neurotransmitter in the electrolyte solution was controlled by the two inlets of the microfluidic channel, mixing a solution with no dopamine with the 1 mM stock solution (**Paragraph 2.4.1**), at a constant flow rate of 200  $\mu$ L per minute. The microfluidic fluid flow across the device was controlled using two microfluidic pumps controlled by a custom LabView software. The transfer characteristics were obtained by sweeping the gate voltage from 0.8 V to -0.2 V and the channel potential from -0.6 V to 0.1 V. The electrochemical oxidation of dopamine was performed applying a pulsed voltage at the gate electrode ( $V_{\text{post}} = +0.3$  V, PW= 2 seconds,  $\Delta t = 2$  seconds) while monitoring the post-synaptic current at a fixed potential ( $V_{\text{ch}} = -0.1$  V).

## 2.5 Characterization of the cell-material interface in the dopamine-mediated biohybrid synapse.

The biohybrid interface between dopaminergic PC-12 cells and the artificial platform was characterized by means of optical and electron microscopy techniques. First of all, the production and secretion of dopamine from cells seeded on PEDOT:PSS spin-coated films, was verified by means of immunohistochemistry and SEM/FIB imaging. Then, the cytotoxicity of the neuromorphic device was investigated performing a biocompatibility assay: here, cells confined on the gate/channel area of the OECT by means of a microfluidic channel (**Paragraph 2.1**), were directly imaged on the device.

### 2.5.1 Preparation of PEDOT:PSS films as control substrate for cell culture.

The PEDOT:PSS solution was prepared with the same formulation used for the fabrication of the neuromorphic device (**Paragraph 2.1.1**). Glass microslides (25 mm × 25 mm) were cleaned in an ultrasonic bath at 40 °C in deionized water, followed by non-ionic detergent, deionized water, acetone and ethanol. Each step had a duration of 10 minutes until a final drying under a nitrogen flow was performed. PEDOT:PSS films were deposited by spin coating technique carried at 1000 RPM for 2 minutes, followed by annealing at 120 °C for 20 minutes.

### 2.5.2 Substrate sterilization and coating for cell culture.

The PEDOT:PSS spin-coated films and the neuromorphic device were first sterilized with repeated washes of 70% ethanol (2 minutes) and sterile milli-Q water (2 minutes), and let dried under a laminar flow of a biological sterile hood. In order to enhance cell adhesion on the substrates, two different protein coatings were tested:

- an aqueous solution of 0.1% collagen-IV from human placenta. Here, as in biological environment collagen is one of the components of the ECM, the cell-substrate interaction relies on the interaction between integrins and receptors placed at the cell membrane and collagen fibers <sup>[252]</sup>.
- an aqueous solution of 0.01% Poly-L-lysine (PLL, molecular weight 70000-150000) which promotes electrostatic interactions between polycationic molecules present in PLL and the anionic sites on cell membrane <sup>[253]</sup>.

Both cell-adhesive coatings were incubated on the samples for 1 hour at 37 °C, 5% CO<sub>2</sub> and 95% humidity, and then washed with sterile milli-Q water.

## 2.6 Cell culture.

The experiments were performed using a catecholamine-containing rat pheochromocytoma cell line (PC-12). Frozen cells were thawed and plated on a collagen-IV coated T25 flask/neuromorphic device. Cells were maintained in supplemented medium containing Dulbecco's Modified Eagle's Medium (DMEM)-high glucose, 10% of fetal bovine serum, ( $C_F = 100$  units penicillin/mL and  $100 \mu\text{g}$  streptomycin/mL), 1% L-glutamine ( $C_F = 2\text{mM}$ ). During cell culture, the medium was changed approximatively every 2-3 days and cells were grown in the incubator at  $37^\circ\text{C}$ , 5%  $\text{CO}_2$  and 95% humidity. Confluent PC-12 cells were gently detached using 0.25% Trypsin-EDTA with an incubation of 5 minutes at  $37^\circ\text{C}$ , 5%  $\text{CO}_2$  and 95% humidity. Cells were observed under a microscope to ensure their detachment from the substrate. Pre-warmed complete growth media was added to the cell suspension in Trypsin with two-fold higher volumes to inactivate the enzymatic action and the whole cell suspension was then transferred into a tube for centrifugation with 1000 RPM for 5 minutes. The supernatant was then removed, and the cell pellet was resuspended in pre-warmed complete growth medium. Cell density of viable cells was determined by using Countess II Automated Cell Counter for the plating. Two different cell densities were tested: a high cell density of  $1,540,000$  cells/cm<sup>2</sup> and a low cell density of  $770,000$  cells/cm<sup>2</sup>.

## 2.7 Biocompatibility assay.

The neuromorphic device cytotoxicity and cells viability were evaluated by a live/dead assay using Calcein acetoxymethyl (Calcein-AM) and Propidium Iodide dyes after 1 day-in-vitro (DIV) and right after applying the pulsed bias at the gate. Calcein-AM is a non-fluorescent cell-permanent dye that selectively labels living cells. Here, once incubated in cell culture, the Calcein-AM is converted in green-fluorescent calcein after the hydrolysis of acetoxymethyl ester by intracellular esterases. Calcein is well-retained in the cell cytoplasm and once excited at  $\lambda_{EX}$  488 nm, it fluorescently emits in  $\lambda_{EM}$  495/515 nm wavelength range. On the contrary, propidium iodide ( $\lambda_{EX/EM} = 535/617$  nm) is a cell-impermeable dye used to detect dead or apoptotic cells as it is able to bind DNA by intercalating between the bases. After removing the culture media and wash the cells with PBS, the staining solution ( $C_F = 1 \mu\text{g/mL}$  for Calcein AM and  $10 \mu\text{g/mL}$  for Propidium Iodide) was added to the cell culture and incubated for 15 minutes at  $37^\circ\text{C}$ , 5%  $\text{CO}_2$  and 95% humidity. Afterwards, cells were rinsed in PBS for de-esterification of the intracellular AM esters and images were acquired at microscope, using an inverted microscope (Axio Vario, Zeiss) operated through epifluorescence employing a  $10\times$  dry objective. Exemplary frames of live and dead cells are shown in **Figure 2.3, A and B**, respectively.

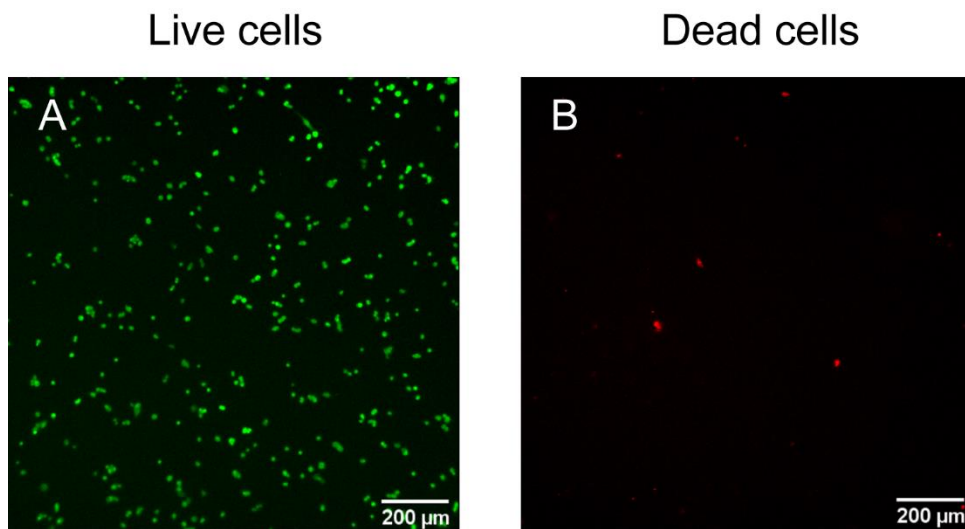


**Figure 2.3. Live/dead cells labelling.** A) Exemplary micrograph of PC-12 cells labelled with Calcein-AM where the green fluorescence denotes live cells. B) Exemplary micrograph of PC-12 cells labelled with Propidium Iodide where the red spots correspond to dead cells.

## 2.8 Immunohistochemistry.

The immunolabelling procedure allows the detection and spatial localization of a protein/molecule of interest within a cell. This targeting might occur using (1) primary and secondary antibodies (Ab I and Ab II, respectively) or (2) conjugated dyes displaying high specificity for the protein of interest. Here, dopamine secretion was verified labelling PC-12 cells (seeded on PEDOT:PSS spin-coated films, **Paragraph 2.5.1**) against dopamine primary antibody (mouse) followed by incubation with Ab II Alexa Fluor 488 anti-mouse ( $\lambda_{EX/EM} = 495/518$  nm), while cell morphology was analyzed staining actin cytoskeleton with Phalloidin-647 conjugated dye ( $\lambda_{EX/EM} = 650/668$  nm), and nuclei with nuclear marker Hoechst ( $\lambda_{EX/EM} = 350/461$ nm). In detail, for the staining procedure at the desired time point for the investigation, the cell culture media was removed and washed once with warm PBS, to remove dead cells or debris in suspension. Then, cells were fixed with pre-warmed 4% paraformaldehyde (PFA) in PBS (pH 7.2) for 15 minutes and then gently washed 2 times with PBS at room temperature. Cell membranes were permeabilized to provide antibody access to targets into the nucleus or other organelles with 0.1% Triton-X 100 in PBS for 5 minutes at room temperature and then washed 2 times with PBS. To prevent any non-specific binding of the antibody, specimens were incubated in 2% bovine serum albumin (BSA) in PBS for 45 minutes at room temperature. Substrates were then incubated for 1 hour at room temperature with dopamine primary antibody, which was diluted 1:100 in 2% BSA in PBS to get  $C_F = 0.2$   $\mu\text{g/mL}$ . After washing the samples 3 times with 2% BSA (diluted in PBS), cells were simultaneously incubated with Ab II anti-mouse diluted 1:500 in 2% BSA in PBS to get  $C_F = 0.2$   $\mu\text{g/mL}$ , and with Phalloidin-647 diluted 1:1000 in 2% BSA in PBS to get a 1x as  $C_F$ : both dyes were incubated for 30 minutes at room temperature, followed by 3 washes with 2% BSA (diluted in PBS). Finally, the nuclei staining was performed incubating the samples for 15 minutes at room temperature with Hoechst diluted 1:5000 in PBS to get a  $C_F = 2$   $\mu\text{g/mL}$ . Samples were shielded from light until imaging. The substrates were imaged with a widefield fluorescence microscope (Axio Observer Z1, Zeiss) operated through epifluorescence a 40 $\times$  oil objective. **Figure 2.4** depicts representative images of F-actin, nuclear and dopamine immunohistochemistry labelling.

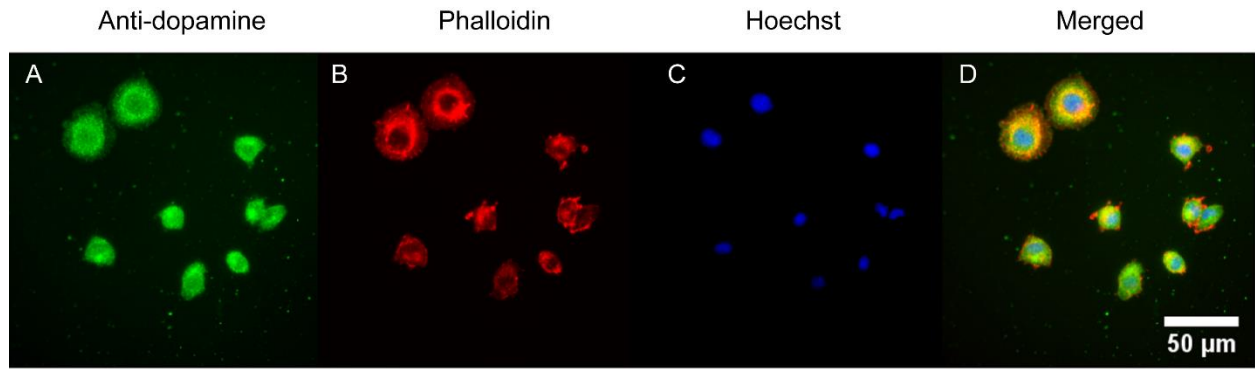


**Figure 2.4. Exemplary images of PC-12 cells immunohistochemistry.** Exemplary confocal micrographs of PC-12 cells that underwent immunohistochemistry staining: A) dopamine molecules labelled by its specific antibody (in green); B) F-actin cytoskeleton labelled with phalloidin (in red); C) cells nuclei labelled with Hoechst (in blue). D) Merged micrograph. Scale bar 50  $\mu\text{m}$ .

## 2.9 Ultra-thin resin embedding procedure for SEM and SEM/FIB.

The scanning electron microscopy technique coupled with focused ion beam requires an *ad hoc* procedure known as ultrathin plasticization method (UTP) <sup>[254,255]</sup> which allows to preserve biological samples during imaging. Cells were firstly rinsed with PBS and then washed in 0.1 M sodium cacodylate buffer ( $C_2H_6AsNaO_2$ ) at physiological pH for 5 minutes before being fixed in 2.5% glutaraldehyde diluted in the same buffer at room temperature (**Figure 2.5 A**). Fixation is performed to block any cellular degeneration processes and preserve morphological shape from shrinkage and swelling (osmotic damages). Therefore, glutaraldehyde stabilizes cellular ultrastructures *via* permanent cross-linking which occurs between its -CHO groups and any protein nitrogen <sup>[256]</sup>. However, this strong and irreversible fixative effect only involves protein structures. Lipidic structures must undergo a secondary fixation to retain their structures during the entire method. After the fixative incubation, samples were transferred on ice (4 °C) and washed 3 times for 5 minutes with buffer. Unreacted aldehyde groups, not bound to anything, were quenched with 20 mM glycine solution in 0.1 M buffer solution for 20 minutes at 4 °C. Specimens were then washed 3 times with buffer (5 minutes each) at 4 °C. To preserve lipidic membranes and fix glycogen, a second fixative step is performed by incubating cells with 2% osmium tetroxide and 2% potassium ferrocyanide for 1 hour at 4 °C. This post-fixative adds density and contrast to the cell as staining solution <sup>[255]</sup>. Samples were then washed 3 times with buffer solution at 4 °C. Prior thiocarbohydrazide (TCH) step, cells were gently washed with deionized (DI) water at room temperature (to prevent TCH salt precipitation). Afterwards, samples were immersed in 1% filtered TCH in DI water for 20 minutes at room temperature. TCH solution profoundly enhanced the contrast of the osmiophilic cell components.

Specimens were washed 3 times with DI water for 5 minutes and subsequently immersed in 2% tetroxide osmium solution for 30 minutes at room temperature (**Figure 2.5 B**). This entire procedure of staining is also known as *RO-T-O* because it includes solutions of potassium ferrocyanide-reduced osmium (RO step), TCH (T step) and osmium (O step). Afterwards, specimens were washed with DI water 3 times for 5 minutes and incubated overnight in 4% filtered uranyl acetate at 4 °C. Uranyl acetate reacts with phosphate and amino groups (*i.e.*, nucleic acid, proteins, mitochondria). Then, samples were washed 3 times with DI water and incubated with 0.15% tannic acid for 3 minutes at 4 °C and then washed 2 times with DI water. Dehydration was carried out with a series of ethanol dilutions (30, 50, 75, 95, 100% v/v ethanol in water) for 10 minutes each at 4 °C. 100% ethanol was exchanged 2 times at room temperature. Specimens were then gradually embedded in resin (25 mL of NSA, 8 mL D.E.R. 736, 10 mL of ERL 4221, 301 µL of DMAE) with an ethanol : resin ratio (1:3 for 3 hours, 1:1 overnight, absolute resin for at least other 8 hours (**Figure 2.5 C**). Minimal resin covering on the cells was achieved by upright positioning the samples and let the resin drain by gravity for 2 hours (**Figure 2.5 D**). In addition, to significantly reduce the final resin layer, samples were quickly rinsed with 100% ethanol for less than 2 minutes prior to polymerization.

However, absolute ethanol flushing step might introduce some artefacts. Indeed, longer washes cause complete exposition and potential dehydration of cellular bodies and processes. Finally, resin was polymerized in the oven at 70 °C for 12-24 hours. Samples were mounted onto aluminum pin stubs (diameter 3.2 mm) using silver conductive paste and sputtered with 5 nm-thick gold layer prior to imaging.

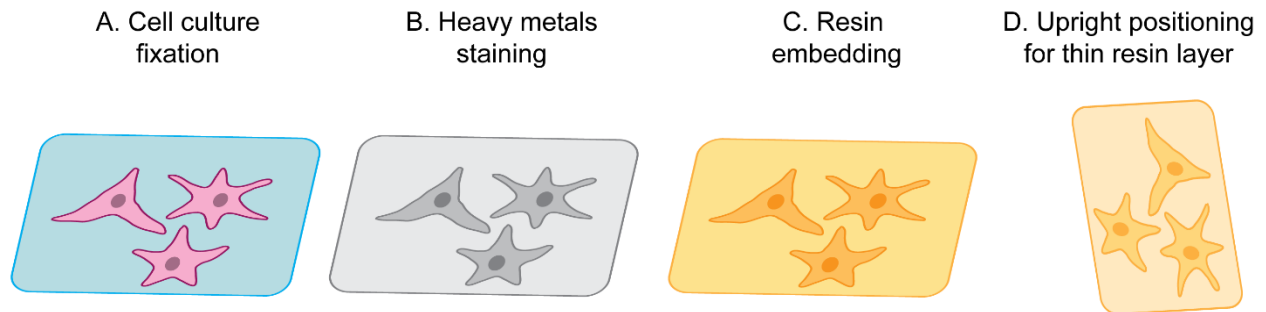


**Figure 2.5. . Ultra-thin plasticization method.** Schematic depicting the procedure of biological sample preparation for electron microscopy: A) fixation of cell culture with glutaraldehyde; B) heavy metals staining to add density and contrast to the cells; C) resin embedding; D) removal of exceeding resin by upright positioning of the sample.

## 2.10 Focused ion beam sectioning/scanning electron microscopy of cross sections.

Specimens were loaded in a dual-beam microscope which supports both an electron beam column (e-beam) and a Ga<sup>+</sup> ions focused beam column (FIB or i-beam). The cell-material contact area was exposed through FIB milling and imaging was then performed with SEM. Here, after identified a region of interest (ROI) (**Figure 2.6 A**), a double Pt layer was deposited to preserve the sample structures from the ensuing destructive cross-sectioning steps. First, a 0.5 μm-thick Pt layer was deposited by e-beam assisted deposition by fixing the voltage of the electron beam at 3 kV and the current at 0.69 – 2.7 nA (**Figure 2.6 B**). Then, a second layer (~1 μm nominal thickness) was deposited by ion beam-assisted deposition (**Figure 2.6 C**), fixing at 30.0 kV and 0.79 nA the ion beam voltage and current, respectively. Afterwards, by fixing the ion beam voltage and current at 30 kV and 0.79 nA, respectively, a large amount of material can be removed by milling, allowing precise exposition of cell-material interface (**Figure 2.6 D**). Notably, the nominal depth (as for silicon) was set to ~ 5 μm and the milling profile used was the ramp. The resulting surface was then further polished avoiding curtaining effects with the ion beam voltage and current at 30.0 kV and 80 pA, respectively. Once the cross section was created, the images were acquired with a backscattered detector <sup>[255]</sup>.

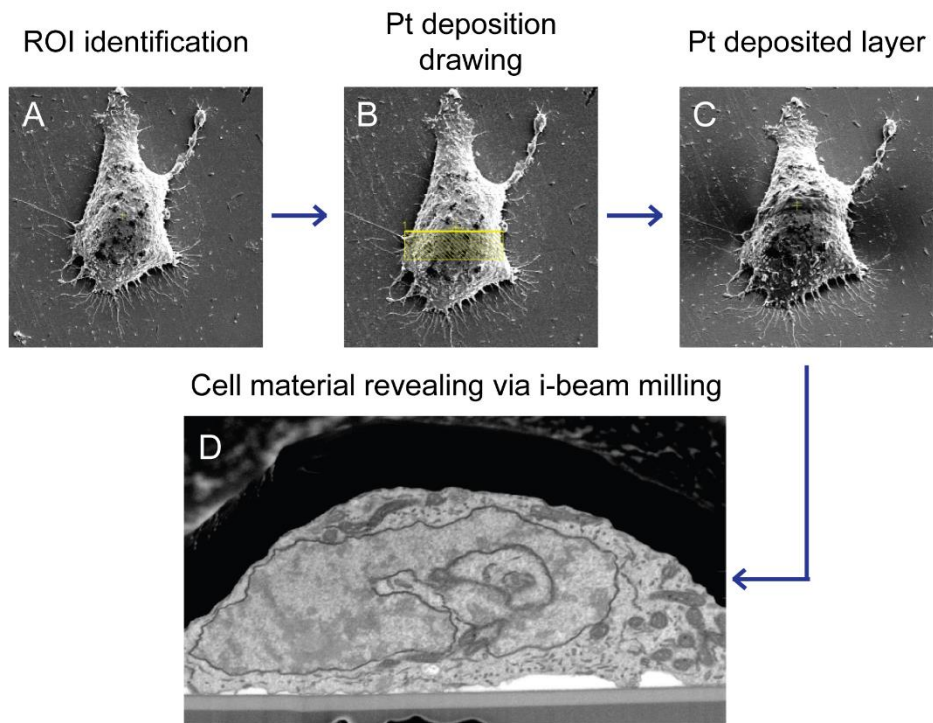


**Figure 2.6. FIB/SEM cross-sectioning and imaging procedure.** A) ROI identification; B) deposition of first layer of Pt with e-beam.-C) deposition of the second Pt layer i-beam; D) i-beam assisted milling to expose the cross section, and backscattered imaging.

### 2.11 Dopamine detection measurements with PC-12 cells.

PC-12 cells were seeded on the neuromorphic device at two different cell densities as described in **Paragraph 2.6**. The electrochemical oxidation under static conditions was performed applying a pulsed bias at the gate every 2 hours to monitor the dopamine secretion process.

For dynamic microfluidic flow measurements instead, PC-12 cells were plated with a low density (770,000 cells/cm<sup>2</sup>) and incubated at 37 °C, 5% CO<sub>2</sub> and 95% humidity for 4 hours prior performing the measurement. Microfluidic flow of warm (37 °C) complete DMEM cell medium (**Paragraph 2.6**) was controlled using custom LabView software and manually updated during the measurement.

For KCl stimulation PC-12 cells were plated at low cell density (770,000 cells/cm<sup>2</sup>) and incubated at 37 °C, 5% CO<sub>2</sub> and 95% humidity for 4 hours prior performing the stimulation: here, the cell medium in the microfluidic channel was removed and the channel was washed with fresh DMEM cell medium (**Paragraph 2.6**) before adding a stimulating solution of composition (in mM): KCl 60 or KCl 120, NaCl 50, CaCl<sub>2</sub> 2, MgCl<sub>2</sub> 0.7, NaH<sub>2</sub>PO<sub>4</sub> 1, HEPES 10 (pH 7.4). The pulsed bias was applied at the gate electrode (**Paragraph 2.3**) immediately following the addition of the KCl solution.

## 2.12 Supported lipid bilayer assembly and characterization.

### 2.12.1 Lipids vesicles preparation.

Lipid vesicles were obtained mixing 100 mol % of 1-Palmitoyl-2-Oleoyl-*sn*-Glycero-3-phosphocholine (POPC) and 0.5% (mol/mol) of 1,2-Dihexadecanoyl-*sn*-Glycero-3-Phosphoethanolamine, Triethylammonium salt (Texas Red) as a fluorescent probe ( $\lambda_{\text{EX/EM}} = 595/615$  nm). The lipids were mixed in chloroform at a desired concentration. The chloroform was firstly evaporated under a nitrogen stream, and then in a desiccator under vacuum for 2 hours to remove residual traces of solvent. The resulted lipid thin film was rehydrated with a mixture of 70% v/v of milli-Q water and 30% v/v of isopropanol to obtain a final concentration of lipid vesicles of 5 mg/mL. Here, the liposome solution was gently vortexed and sonicated on ice for 25 minutes to promote the resuspension of the lipid film. Finally, the lipid suspension was extruded 15 times through a 100 nm pore polycarbonate membrane by using a mini extruder to guarantee the formation of lipid vesicles with homogeneous size.

### 2.12.2 Lipid bilayer formation.

The assembly of lipid bilayers on soft organic polymers requires an *ad hoc* technique based on a solvent-assisted procedure (SALB), where the organic solvent mixture, in which the lipids are suspended, is slowly replaced with an aqueous buffer <sup>[142]</sup>. Prior the membrane formation, the OECT was treated with oxygen plasma for 2 minutes at 20 W to enhance the surface wettability of the PEDOT:PSS film and promote the lipid vesicles absorption. Then, to enable the subsequent solvent exchange, a PDMS microfluidic channel (**Paragraph 2.2**) was stick on the neuromorphic device to confine SLB on the gate/channel area. In particular, the microfluidic channel was attached using a two component silicone glue, which allows a fast sealing and therefore allows to preserve the surface activation obtained after oxygen plasma. The liposome solution (**Paragraph 2.12.1**) was subsequently diluted with a mixture of 70% v/v of milli-Q water and 30% v/v of isopropanol to a final concentration of 0.5 mg/mL and incubated for 30 minutes in the microfluidic chamber to enable vesicles adsorption on the PEDOT:PSS surface. Later, an aqueous buffer solution made of TRIS (10 mM) and NaCl (100 mM) at pH 7.5, was delivered into the microfluidic channel with a flow rate of 50  $\mu\text{L}/\text{min}$  for 2 hours to enable the SLB planar assembling and remove exceeding un-ruptured vesicles.

### 2.12.3 SLB characterization with fluorescence recovery after photobleaching.

Fluorescence recovery after photobleaching (FRAP) is a microscopy-based method used to study membrane dynamics, as it allows to characterize the mobility of fluorescent molecules within cell membranes. In general, a ROI is bleached by a high-intensity laser source: if the fluorescent species is mobile, the bleached molecules within the ROI will be exchanged by fluorescent molecules diffusing from surrounding regions, therefore the time required to recover the initial fluorescent intensity depends on the fluidity of the membrane. The resulting fluorescence recovery curve, fitted with an appropriate model, provides information about the fraction of mobile molecules and the half time of recovery ( $\tau_{1/2}$ ), *i.e.*, the time required to recover half of the final fluorescence intensity <sup>[257]</sup>. In case of SLBs,  $\tau_{1/2}$  can be used to calculate the diffusion coefficient of the lipid molecules providing information on the fluidity of the double layer, as lower values of  $\tau_{1/2}$  corresponds to a fluid and homogeneous bilayer. Here, the optical transparency of the neuromorphic device (**Paragraph 2.2**) enabled the direct monitoring of SLB fluorescence recovery. In particular, FRAP experiment was performed using a Leica TCS SP5 gated STED microscope equipped with a 25× water immersion objective. A 20  $\mu\text{m}$  wide circular spot was bleached by 114 mW 592 nm laser beam for 1.3 seconds (**Figure 2.7 A-i**). The recovery of the photobleached spot was then monitored for 5 minutes (**Figure 2.7 A-ii**). The fluorescence intensity of the spot was measured and normalized to a reference spot (**Figure 2.7 B, inset**). The normalized fluorescence intensity is fit with a Bessel function of the first order <sup>[258]</sup> (**Figure 2.7 B**). The images were analyzed with ImageJ Radial profile tool which allows the quantification of the fluorescence intensity along the radius of a selected area. The fluorescence intensity profiles at three different time points after bleaching (0 second, 60 seconds and 5 minutes), were obtained by drawing a circle around the bleached area (**Figure 2.7 C**). The diffusion coefficient was obtained from the following equation:

$$D = \frac{\omega^2}{4\tau_{1/2}}$$

where  $\omega$  is the radius of the bleached spot.

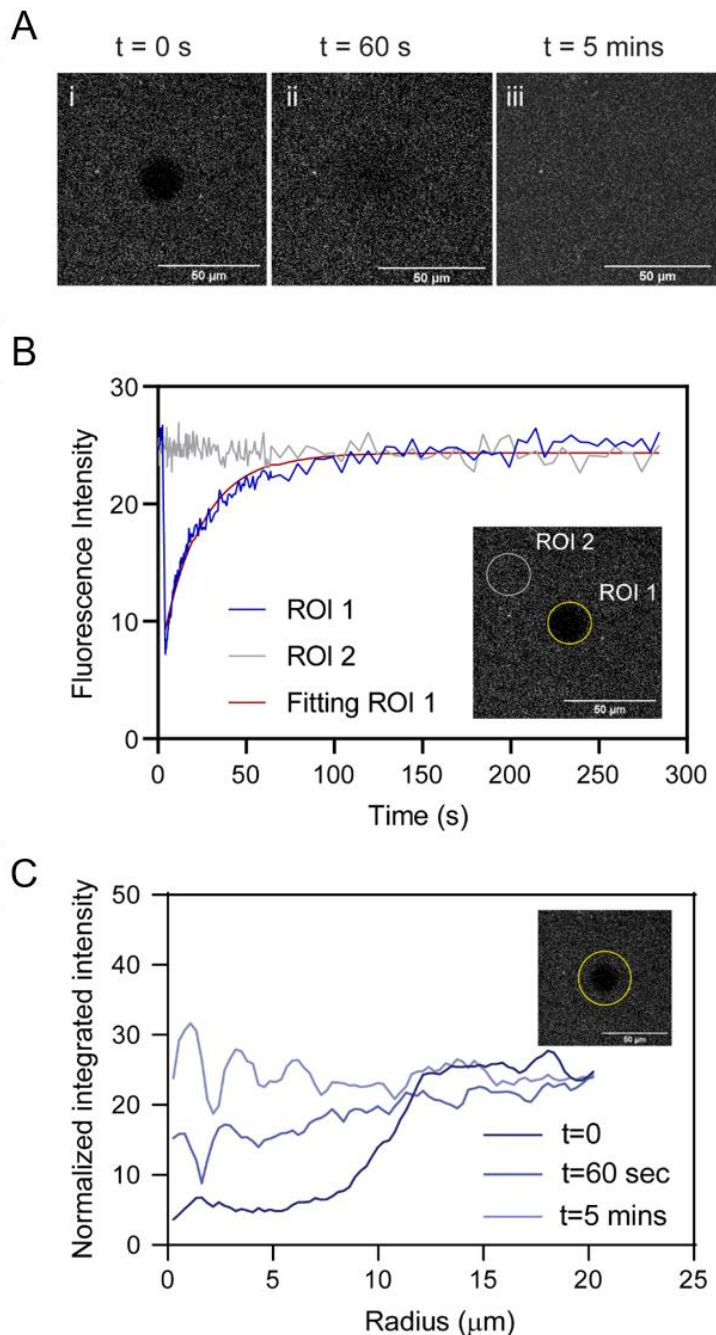


**Figure 2.7. FRAP images and data analysis.** A) Exemplary micrographs of the photobleached area in the POPC lipid bilayer showing the progressive recovery of fluorescence at fixed time points (i-iii). B) Graph reporting the fluorescence intensity of the bleached ROI (ROI 1) and the reference ROI (ROI 2) as function of time. C) Fluorescence intensity profiles obtained from the Radial profile analysis of the FRAP micrographs taken at  $t=0$ , 60 s and 5 minutes after bleaching.

#### 2.12.4 SLB characterization with atomic force microscopy.

Atomic Force microscopy is a high-resolution (order of fractions of a nanometer) non-optical imaging technique based on a scanning-probe microscope which allows accurate and non-destructive measurements of the topographical, optical and mechanical properties of a sample surface in air, liquids or ultrahigh vacuum <sup>[259]</sup>. AFM consists of a sharp tip with a diameter approximately around 10-20 nm which is attached to a cantilever. The tip moves in response to tip–surface interactions, and this movement is measured by focusing a laser beam with a photodiode. AFM can be operated in two basic modes: in the contact mode the tip is in continuous contact with the surface applying a constant force on the sample, while the tapping mode is based on the vibration of the cantilever above the sample surface so that the tip is only in intermittent contact with the surface <sup>[260]</sup>. The latter is preferred when scanning soft materials like polymers and biological samples as it prevents possible damages of the sample <sup>[261]</sup>, therefore here the surface profile of the bilayer and of the OECT (prior SLB assembly) were investigated using the tapping mode technique in liquid (**Figure 2.8 A**): the hydrated condition indeed is essential to preserve the structure of the double layer and the correct assembly of the amphiphilic lipid molecules. In particular, AFM measurements were carried out on Bruker Dimension Icon microscope employing a ScanAsyst-Fluid probe, with a spring constant of 0.7 N/m, a tip radius of 5–20 nm, and resonance frequency of about 150 kHz. The scan rate was set at 2 Hz for 256×256 pixels images and the gain was optimized to reduce the noise. The root mean-square (RMS) roughness (Rq) was determined using the provided analysis software Nanoscope Analysis 2.0. The images were plane fitted at order 0 and flattened at order 2 (**Figure 2.8 B**). The average roughness parameters were calculated over 2 μm x 2 μm areas.

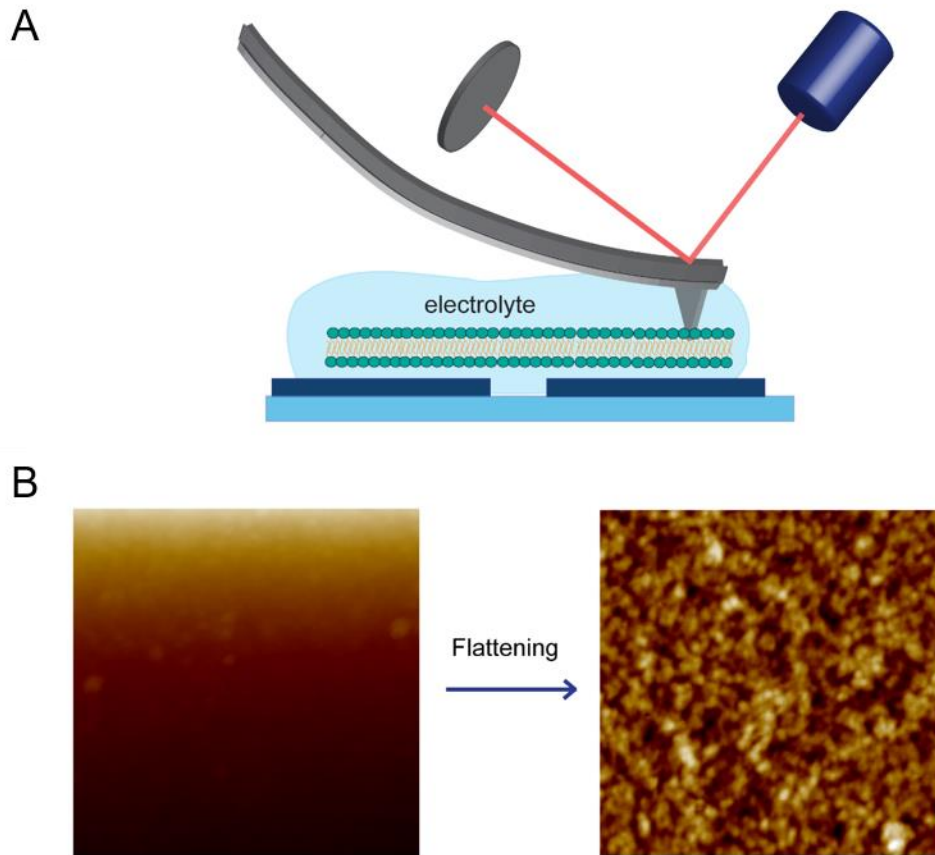


**Figure 2.8. AFM images analysis.** A) Schematics depicting the AFM setup used to perform the SLB scan in aqueous environment. B) Processing of AFM images to obtain a flattened image which allows the quantification of surface roughness.

### 2.13 Frequency response characterization of the lipid bilayer-based biomimetic synapse.

Impedance spectroscopy is a powerful technique used to measure the frequency response and surface-dependent properties of a system upon the application of alternate potentials <sup>[262]</sup>. In particular, electrochemical impedance spectroscopy (EIS), performed in aqueous environment and with a two-electrode configuration, allows to investigate diffusion, electron transfer rate or absorption mechanisms at the working electrode/electrolyte interface. EIS found extensive application in investigating biological processes, as cell adhesion and proliferation <sup>[263,264]</sup>: indeed, cell membranes and more in general biological tissues, consist of insulating layers that behaves like leaky capacitors, *i.e.*, devices that accumulate charges on the surface, while still allowing for a leakage current to cross the layer itself <sup>[265]</sup>, therefore any variation in the cell monolayer (due to cell-cell or cell-substrate interactions) influence the number of ions that freely reach the electrode surface, modulating the resistive component of EIS <sup>[263]</sup>. Similarly, the formation of lipid bilayers on conductive substrates (*i.e.*, conductive polymers) can be validated by monitoring variations in impedance components <sup>[157,158,160,161]</sup>. Usually, impedance data can be visualized either as Nyquist plot, where the real part of the impedance is plotted on the X-axis and the imaginary part is plotted on the Y-axis of a chart (**Figure 2.9 A**), or as Bode plot where the impedance is plotted with log frequency on the X-axis and both the absolute values of the impedance and the phase-shift are displayed on the Y-axis (**Figure 2.9 B**). Impedance data can then be analyzed by fitting the Nyquist or Bode curves with an equivalent electrical circuit model where each component (*i.e.*, resistors, capacitors and inductors) describe a physical process happening in the electrochemical cell. For instance, phenomena of ionic (or molecular) diffusion, which cause the appearance of a diagonal line with a slope of 45° in the Nyquist plot, can be modelled introducing a Warburg element in the modeling circuit <sup>[262]</sup>. Furthermore, the electrolyte resistance, depending on the ionic concentration, type of ions, temperature, and the geometry of the area in which the current is measured, can be expressed as a resistor, while the electrical double layer formed at the interface between the electrode and its surrounding electrolyte can be described as a capacitor where the adsorbed charged ions are separated from the electrode surface by an insulating space <sup>[262]</sup>. Here, the frequency response of the biomembrane-based OECT was characterized performing EIS and a planar frequency measurement: the use of these two configurations enables the investigation of the biomembrane electrical behavior in response to a longitudinal (planar measurement) or transverse (EIS) ionic current. Both measurements were carried out using an Autolab PGSTAT302N potentiostat/galvanostat interfaced with a personal computer, equipped with NOVA software; the impedance was recorded in the range 10-1-106 Hz, using a sinusoidal input voltage with amplitude of 50 mV, with 0 V offset. EIS was performed using a saturated silver/silver chloride (sat'd Ag/AgCl) as reference electrode while the PEDOT:PSS neuromorphic channel was used as working electrode (**Figure 2.9 C**). A buffer solution made of TRIS (10 mM) and NaCl (100 mM) at pH 7.5 (same buffer used to form lipid bilayer, **Paragraph 2.12.2**) was used as electrolyte. In the planar frequency

response measurement instead the PEDOT:PSS gate and channel were used as reference and working electrodes, using two wired measurements probes to connect the device without the electrolyte (**Figure 2.9 D**).

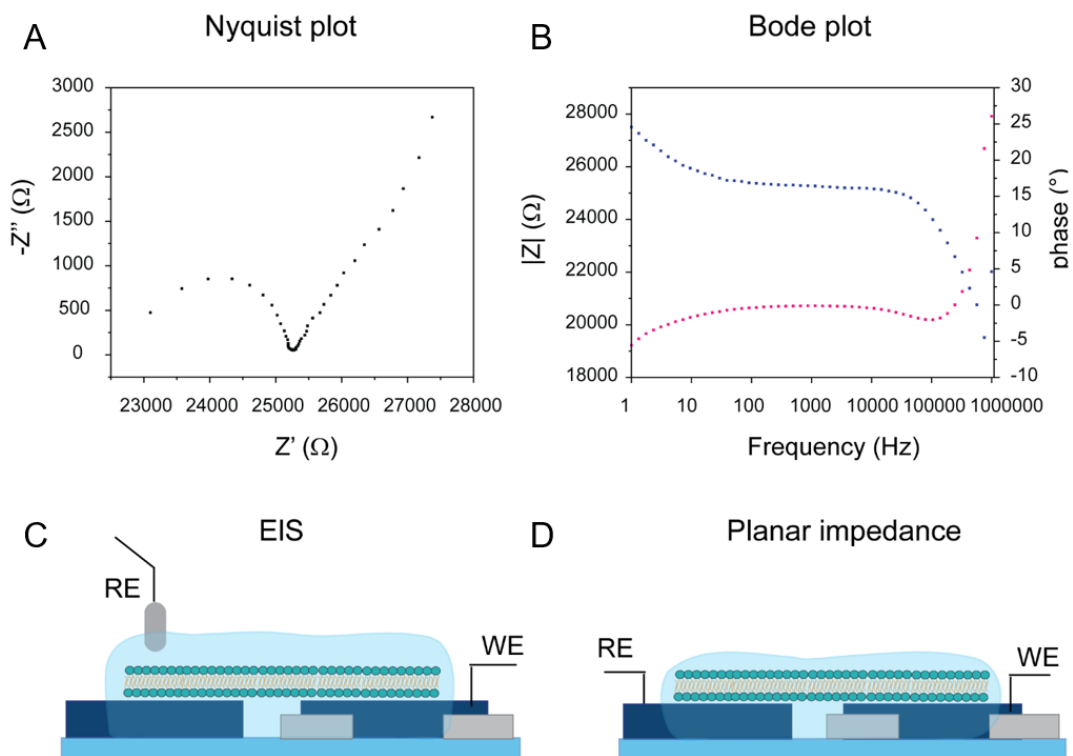


**Figure 2.9. Frequency response analysis and measurement setup.** A) Nyquist plot reporting the real and the imaginary values of impedance. B) Bode plot depicting the modulus and phase of impedance as function of frequency. C) Schematics of the measurement setup used to perform EIS with a top Ag/AgCl reference electrode. D) Schematics of the measurement setup used to perform planar impedance, where the PEDOT:PSS film itself was used as reference electrode.

## 2.14 Image processing and data analysis.

### 2.14.1 Live/dead cell populations analysis.

Acquired images were processed with Image J software (NIH, USA) to perform cell counting of live and dead cells populations. The analysis was performed on each frame derived by the Calcein-AM and Propidium Iodide labelling (**Paragraph 2.7**). The main analysis steps are described in **Figure 2.10**. In details, the red and green fluorescence channels were split in two separated images (**Figure 2.10 A**), and the uneven background was removed from the fluorescence microscopy images (**Figure 2.10 B**). Afterwards, an intensity threshold was applied to highlight all cells to count, so that the algorithm Find Maxima is able to find local maxima of fluorescent intensity: in this way each cell was considered as a particle and automatically counted (**Figure 2.10 C**).

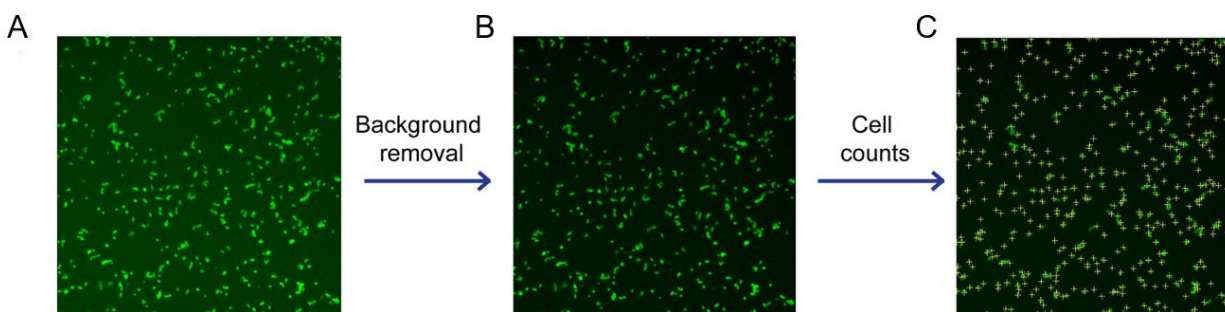


**Figure 2.10. Live/dead image analysis.** Schematic of the semi-automatic cell counts for viability quantification. A) Opening of green and red frames separately; B) image background removal; C) setting of the fluorescence-dependent threshold to identify single cells.

Viability was determined by acquiring 10 frames per experiment from 3 independent cell preparations (thereby  $N = 3$  is the statistical sample) collected randomly over the material surface. Each experimental condition was studied in triplicate ( $n = 3$ ). The percentage of cells viability was evaluated using the following formula:

$$\% \text{ Viability} = \frac{(\text{Live cells})}{(\text{Live cells} + \text{Dead cells})} \times 100$$

### 2.14.2 Data processing and analysis.

The pulse conductance modulation and the integration of the gate current for the biohybrid and biomimetic OECTs, as well as the EIS data analysis and fittings were carried out through SciPy and NumPy Python

libraries. Additionally, the numerical computation of the time response  $\tau$ , was performed through custom made MATLAB scripts. See **Annex C, D** and **E** for detailed scripts.

### 3 Results and Discussion

#### 3.1 Engineering a dopamine-mediated biohybrid synapse

The first part of the project was focused on engineering a functional biohybrid synapse with an organic electrochemical transistor acting as post-synaptic neuron, and dopaminergic cells, directly interfaced with the artificial platform, representing the biological pre-synaptic terminal. Here, the oxidation of dopamine secreted from cells is able to modulate the conductance of the OECT inducing a neurotransmitter-mediated long-term potentiation which emulates the synaptic plasticity of neurons.

##### 3.1.1 Characterization of the organic neuromorphic device artificial synapse.

The OECT was fabricated by means of photolithography (**Materials and Methods 2.1**) to obtain a three-terminal device with both gate and neuromorphic channel made of PEDOT:PSS. The platform was coupled with a microfluidic PDMS channel (**Materials and Methods 2.1**) to support the continuous flow of the electrolyte solution in contact with the device (**Figure 3.1 A**). The variation of the OECT channel current in response to gate voltage applied is given by the output and transfer characteristic curves which were acquired sweeping the gate (from 0.8 V to -0.2 V) and the channel voltage (from -0.6 V to 0.1 V) simultaneously (**Materials and Methods 2.3**). **Figure 3.1 B** reports the output curves which show the variation of the channel current ( $I_{\text{post}}$ ) as function of the output voltage ( $V_{\text{ch}}$ ). Here, three operating regions of the OECT can be identified: 1) the active region of the transistor, where the output current is almost constant and independent from the output voltage; 2) the saturation region, where a slight increase in output voltage causes a rapid increase in the output channel current and 3) the cut-off region, where the output current is almost zero even at higher  $V_{\text{ch}}$ . **Figure 3.1 C** instead displays the transfer curves, where the output current ( $I_{\text{post}}$ ) is represented vs. the input gate voltage ( $V_{\text{post}}$ ), and the transconductance ( $g_m$ ), defined as the derivative of the channel current with respect to the gate voltage, which describes the ability of the OECT in amplifying the input voltage signal applied at the gate electrode. Furthermore, the neuromorphic functions of the OECT were investigated applying a sequence of voltage pulses at the post-synaptic gate electrode while monitoring the output channel current at a fixed potential ( $V_{\text{ch}} = -0.1$  V, **Materials and Methods 2.3**). In particular, as PEDOT:PSS-based OECTs operate in depletion mode<sup>[266]</sup>, the application of a positive bias at the gate terminal drives cations from the electrolyte into the neuromorphic channel, inducing the de-doping of the organic semiconductor; when the voltage gate is switched back to 0 ( $V_{\text{post}} = 0$  V), cations can freely return into the electrolyte restoring the initial conductive state of the PEDOT:PSS channel (**Figure 3.1 D**). Such reversible (short-term) conductance modulation recalls the STP of biological synapses.

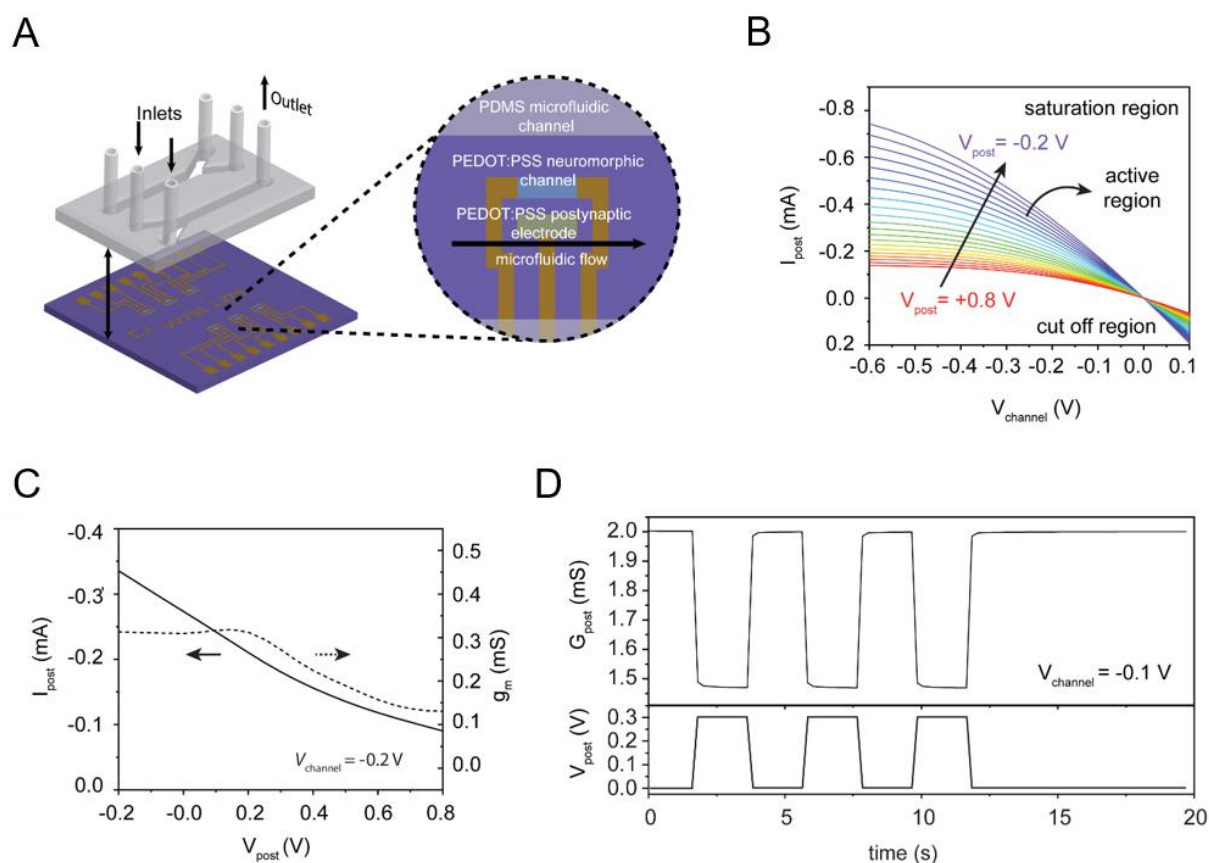


**Figure 3.1. Characterization of the organic neuromorphic device.** A) Schematic showing the neuromorphic device array coupled to the polydimethylsiloxane (PDMS) microfluidic channel and inset showing the single device structure. B) Output curves for the postsynaptic gate voltage  $V_{post}$  from  $+0.8\text{ V}$  (red) to  $-0.2\text{ V}$  (purple) with  $0.1\text{ V}$  increments. C) Transfer characteristics obtained by sweeping the voltage of the postsynaptic PEDOT:PSS gate electrode  $V_{post}$ . D) Pulsing curves of the PEDOT:PSS neuromorphic device showing that the postsynaptic current returns to the original level after a sequence of postsynaptic voltage pulses in the absence of dopamine with a short-term modulation of  $\sim 0.5\text{ ms}$  due to ionic currents. Adapted from ref. [267].

### 3.1.2 Characterization of the electrochemical oxidation of dopamine.

As the first part of the project is focused on tuning the neuromorphic properties of OECTs exploiting dopamine oxidation, the electrochemical reaction of the neurotransmitter at the PEDOT:PSS post-synaptic electrode was investigated by means of cyclic voltammetry (CV, **Materials and Methods 2.4.1**). The expected mechanism is a two-electron transfer reaction where dopamine is oxidized to dopamine-o-quinone releasing two protons and two electrons (**Figure 3.2 A**)<sup>[268]</sup>. The voltammograms in **Figure 3.2 B** report, for different concentration of dopamine, the current measured at working electrode as function of the voltage scanned during the analysis. Here, for low concentrations of dopamine (20-200  $\mu\text{M}$ ), the voltammogram shows an oxidation peak at 100 mV, which slightly shifts towards higher potential ( $\sim 200$ -

300 mV) when increasing the neurotransmitter concentration (0.5-1 mM). Interestingly, no reduction peak is observed in the reverse scan, meaning that the reaction is irreversible.

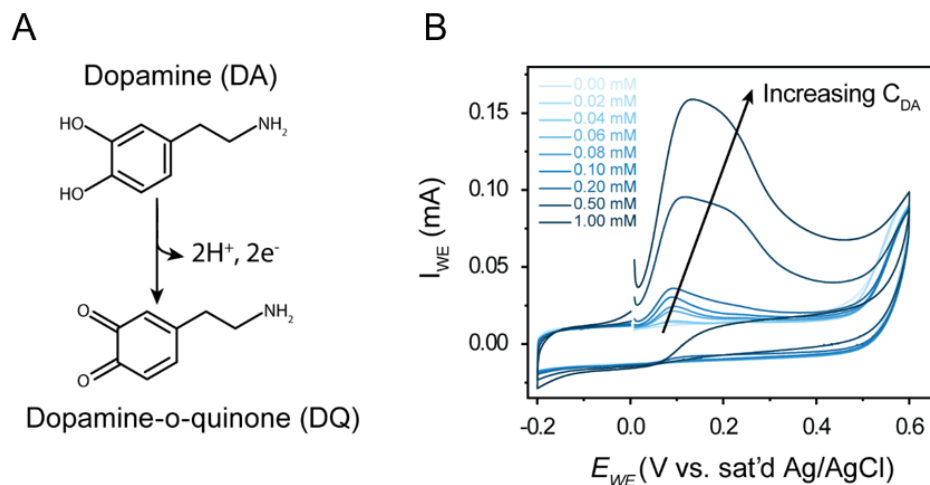


**Figure 3.2. Characterization of dopamine electrochemical oxidation.** A) Schematic of dopamine oxidation reaction at the postsynaptic electrode which controls the change in conductance of the postsynaptic channel. B) Cyclic voltammograms of PEDOT:PSS in solutions with varying dopamine concentration ( $C_{DA}$ ) using a three terminal half-cell measurement with Ag/AgCl as a reference electrode and a Pt mesh as the counter electrode. Adapted from ref. [267].

### 3.1.3 Calibration of the organic neuromorphic device with increasing dopamine concentration (steady-state measurements).

As OECTs conduction mechanism is based on the ionic to electronic current transduction of conductive polymers, electrochemical reactions releasing ionic species in solution can modulate the conductivity of such devices. In particular, in order to characterize the OECT response to the dopamine oxidation, the microfluidic channel was used to vary the concentration of neurotransmitter by using the two inlets to mix two different solutions: one without dopamine and the other containing 1 mM dopamine (**Materials and Methods 2.4.2**). The characteristic curves of the neuromorphic platform were then obtained by monitoring the post-synaptic current ( $I_{post}$ ) while sweeping the voltage at the gate electrode (where dopamine is actually oxidized) in presence of varying concentrations of dopamine (**Figure 3.3 A**). Here, the transfer curves exhibit decreasing values of output current as the dopamine concentration is increased. Similarly, the transconductance ( $g_m$ ) curves (**Figure 3.3 B**) reveal how, in correspondence of the oxidation potential of dopamine ( $V_{post} = +0.2$  V), the transconductance peak increases linearly with the neurotransmitter concentration until reaching a plateau at higher dopamine concentration (ca. 0.1 mM), as shown also in **Figure 3.3 C**. The hypothesized mechanism to explain the OECT behavior in response to dopamine

oxidation is shown in **Figure 3.3 D** where an oxidizing potential is applied at the post-synaptic gate electrode and the conversion of dopamine into dopamine-o-quinone induces the release of two electrons and two protons. Here, electrons are able to reduce the PEDOT in the two PEDOT:PSS electrodes (gate and channel), while protons compensate the remaining negative charges on the sulfonate groups of the PSS to maintain charge neutrality in the polymeric film <sup>[269]</sup>. Considering that both the post-synaptic electrode and channel are de-doped by the oxidation of dopamine, a decreased conductivity was observed in the two PEDOT:PSS films after the oxidation reaction (**Figure 3.3 E**) <sup>[270]</sup>.

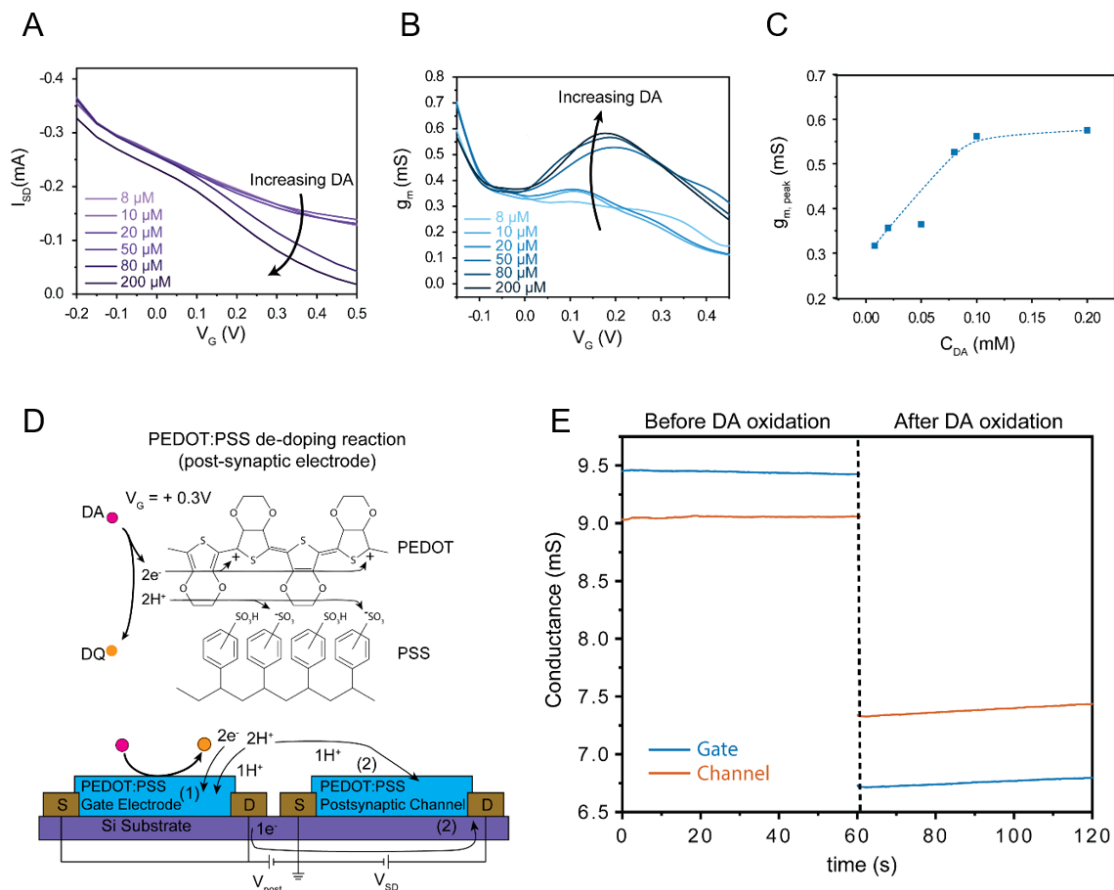


**Figure 3.3. Calibration of the OECT response varying dopamine concentration.** A) Transfer curves measured with varied dopamine concentration; B) transconductance curves acquired at different dopamine concentration in the microfluidic channel. C) Calibration curve showing the peak transconductance during transfer measurements as a function of increasing dopamine concentration. D) Mechanisms underlying dopamine-mediated conductance modulation: when dopamine (DA, pink circles) is oxidized to dopamine o-quinone (DQ, yellow circles), the oxidation products ( $2e^-$ ,  $2H^+$ ) can compensate the electronic and ionic charges in doped PEDOT:PSS, thereby de-doping the channel and gate; this reaction at the gate electrode (1) changes its potential, resulting in effective gating of the PEDOT:PSS postsynaptic channel, and results in a transfer of an electron and a proton to the postsynaptic channel (2) to maintain a potential drop of  $V_{post}$ . E) Conductance modulation of gate and channel electrodes as a result of dopamine oxidation. Adapted from ref. [267].

### 3.1.4 Dopamine-mediated synaptic plasticity.

In order to emulate the biological mechanism of synapses where the periodic stimulation of the pre-synaptic neuron induces the release of neurotransmitters at the synaptic cleft causing the strengthening (or weakening) of the synaptic connection and a long-term potentiation (or depression) of the post-synaptic site [26], here post-synaptic voltage pulses were applied at the gate electrode to characterize the plasticity response at the post-synaptic channel (**Figure 3.4 A, Materials and Methods 2.4.3**). In particular, the sequence of pulses had an amplitude of 0.3 V ( $V_{\text{post}}$ ) to enable the oxidation of dopamine, a pulse width (PW) of 2 seconds and an interval time between pulses ( $\Delta t$ ) of 2 seconds. As shown in **Paragraph 3.1.1**, such PW and  $\Delta t$  allow the reversible ON/OFF switching of the OECT as the 2 seconds delay between pulses enables the ionic discharge of the PEDOT:PSS channel restoring the initial conductive state. Furthermore, the electrical measurements were performed flowing the electrolyte solution at a constant rate into the microfluidic channel to facilitate the recycling of dopamine at the post-synaptic gate surface while preventing the fouling of the electrode due to deposition of oxidation byproducts (*i.e.*, polydopamine [271]). As shown in **Paragraph 3.1.1 (Figure 3.1 D)**, when a pulsed voltage is applied at the gate, the neuromorphic channel undergoes a reversible and temporary de-doping (without dopamine). Instead, when the dopamine is present in the electrolyte, protons produced by the oxidation reaction at the gate electrode contribute to the de-doping of the post-synaptic channel [269]. In this case, due to the irreversible nature of dopamine oxidation, the PEDOT:PSS conductance variation ( $\Delta G_{\text{post}}$ ) is permanently retained as protons injected into the polymeric film under an applied potential ( $V_{\text{post}}$ ), are not able to return into the electrolyte even if  $V_{\text{post}}$  is switched back to 0 V.

To further characterize the dopamine-mediated neuromorphic behavior of the OECT, the concentration of the neurotransmitter in solution was varied using the microfluidic mixing described earlier (**Materials and Methods 2.4.2**). Similar to the response observed in the transconductance curves (**Figure 3.3 B**), also the conductance modulation  $G_{\text{post}}$  is dependent on dopamine concentration (**Figure 3.4 B, C**) as more dopamine is oxidized at the gate electrode more protons accumulate in the electrolyte and therefore contribute to the cumulative de-doping of the PEDOT:PSS channel.

. The dopamine-mediated plasticity observed in the artificial synapse emulates both short and long-term potentiation of biological synapses, where the reversible modulation of  $G_{\text{post}}$  during pulsing recalls the STP, while the permanent change in  $G_{\text{post}}$  following pulsing is analog to LTP (**Figure 3.4 D**).

As in biological systems the synaptic strength can be enhanced [62] with high-frequency presynaptic pulses [62], here the pulse-time dependence of the device was investigated applying at the gate electrode sequence of pulses with different pulse width. As shown in **Figure 3.4 E**, the minimum pulse width resulting in a change

in post-synaptic conductance (LTP) also depends on the dopamine concentration; at 0.02 mM the pulse width must be higher than 100 ms to elicit a response, whereas at 0.2 mM a pulse width of 10 ms is sufficient to cause LTP: taking into account also the diffusion of dopamine into the electrolyte, perhaps at higher concentration a larger number of dopamine molecules are available at the gate electrode for being oxidized.

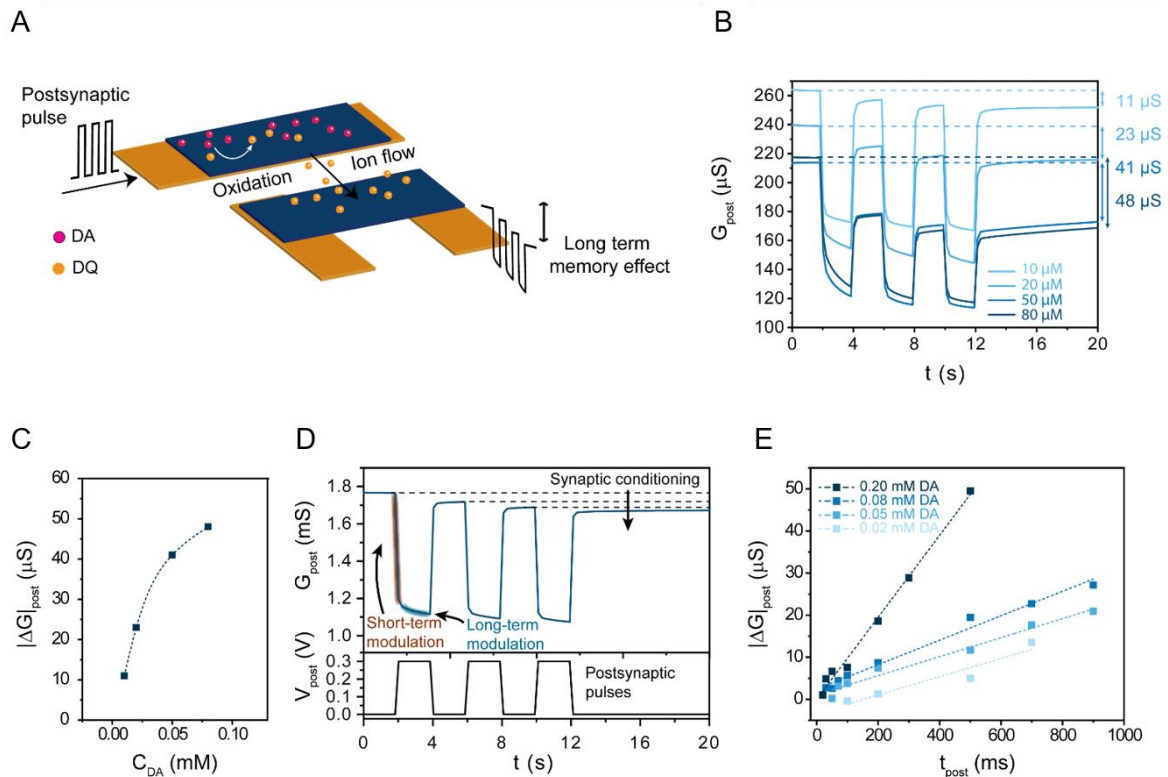


**Figure 3.4. Dopamine-mediated synaptic plasticity in artificial synapse.** A) Schematics depicting how the application of post-synaptic pulses at the gate electrode induces dopamine oxidation and consequent modulation of the post-synaptic current. B) Conductance modulation  $G_{\text{post}}$  elicited by three consecutive postsynaptic pulses ( $V_{\text{post}} = +0.3$  V,  $t_{\text{post}} = 2$  s) as a function of the dopamine concentration in the microfluidic channel. C) Calibration curve of conductance variation as function of dopamine: enhanced long-term modulation is observed with increasing dopamine D) Short-term and long-term modulation of the postsynaptic conductance ( $G_{\text{post}}$ ) under dopamine flow (in the absence of cells). E) Postsynaptic channel conductance update as a function of gate voltage pulse width with varied dopamine concentrations showing a nearly linear time dependence for all concentrations. Adapted from ref. [267].

### 3.1.5 Characterization of PC-12 cells-OECT interface.

In order to establish a biohybrid synapse, where the neuromorphic device responds to stimuli coming from a biological system, PC-12 neuron-like cells were plated onto PEDOT:PSS gate/channel electrodes using the microfluidic channel (**Materials and Methods 2.1, 2.6**). Here the OECT acts as artificial post-synaptic terminal, while the cell monolayer collectively constitutes the pre-synaptic domain. PC-12 cells, derived

from a pheochromocytoma of the rat adrenal medulla, are widely used in neurobiological studies as model system to investigate neuroinflammation, synaptogenesis and neurosecretion, thanks to their tendency to generate vesicles of dopamine and release them spontaneously <sup>[272,273]</sup>. First of all, cells' viability on PEDOT:PSS films was investigated by a live/dead assay (**Materials and Methods 2.7**) where live and dead cells populations were labelled with green and red fluorescence markers, respectively (**Figure 3.5 A**). Two different protein coatings (Collagen-IV and Poly-L-lysine) were tested to enhance cells' adhesion on the polymeric film (**Materials and Methods 2.5.2**): as the statistical analysis performed on the live/dead assay images (**Materials and Methods 2.14.1**) revealed a higher percentage of living cells on Collagen-IV-coated substrate (**Figure 3.5 B**), such protein coating was employed in the following experiments. Furthermore, the presence of dopamine vesicles in PC-12 cells seeded on PEDOT:PSS film was verified by means of immunohistochemistry (**Materials and Methods 2.8, Figure 3.5 C**), labelling dopamine with a specific antibody (green), while the F-actin cytoskeleton and nuclei were visualized with phalloidin (red) and Hoechst (blue), respectively. Here, the green fluorescence signal confirmed the presence of dopamine vesicles locally at the cell membrane, showing that dopamine is produced in vesicles in the PC-12 cells and then released.

To characterize the physical coupling between the cell monolayer and the neuromorphic device, the junction between PC-12 cells and the surface of the post-synaptic gate electrode was investigated using cross-sectional scanning electron microscopy with focused ion-beam milling (FIB/SEM, **Materials and Methods 2.9, 2.10**). The interspace between the plasma membrane of dopaminergic cells (pre-synaptic domain) and the PEDOT:PSS electrode (post-synaptic domain) constitutes the biohybrid synaptic cleft with an average spacing of 100 nm and minimum distance points of 5 – 10 nm, which is comparable to previous reports (REF) and similar size to biological neuronal synapses (5-10 nm, **Figure 3.5 D**) <sup>[274]</sup>.

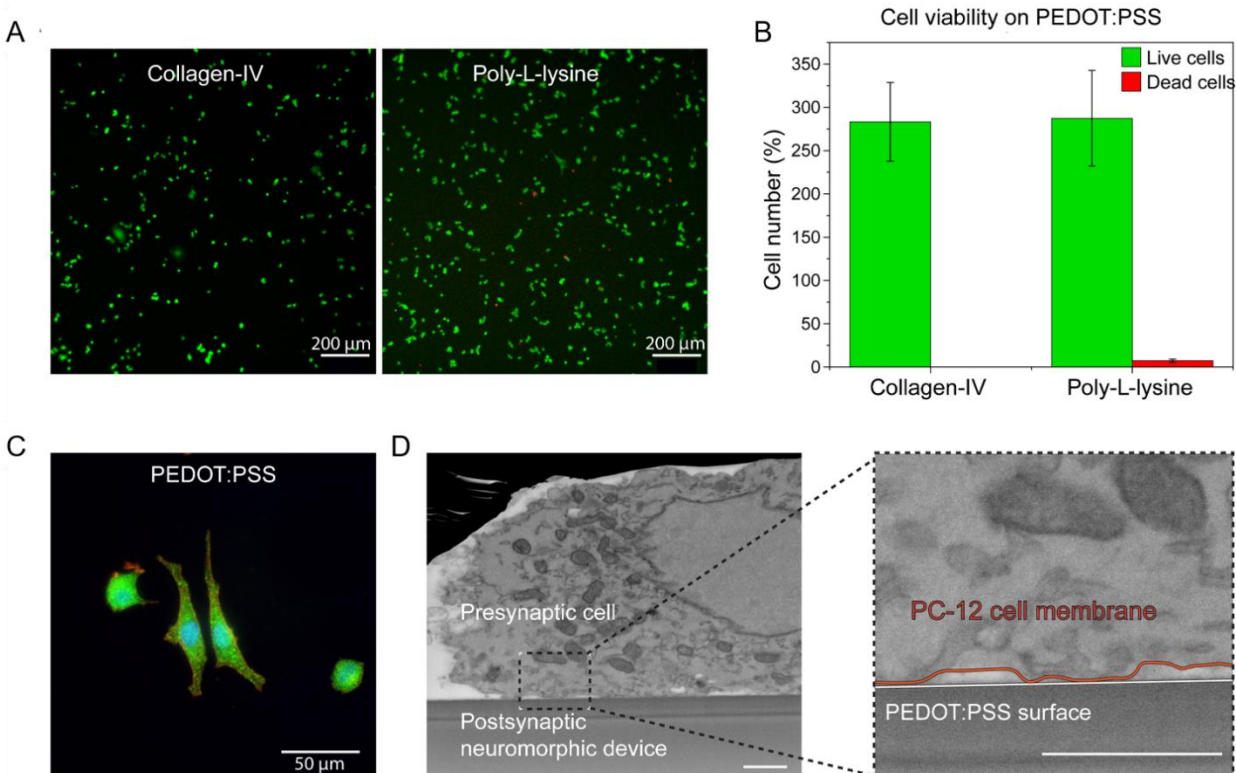


**Figure 3.5. Characterization of the biohybrid interface.** A) The viability of PC-12 cells was tested by staining live cells with calcein-AM (green) and dead cells with propidium iodide (red) for PEDOT:PSS electrodes coated with , collagen IV and poly-L-lysine films. B) Statistical analysis of cells viability on collagen-IV and PLL-coated PEDOT:PSS substrates. C) Immunohistochemistry of PC-12 cells seeded on PEDOT substrate, where dopamine is labelled in green, cell cytoskeleton in red and nuclei in blue. Scale bar: 50  $\mu\text{m}$ . D) SEM/FIB cross sectional image of a PC-12 cell (pre-synaptic terminal) plated on PEDOT:PSS (post-synaptic terminal) with inset highlighting the cell membrane (orange) to electrode (white) interface. Adapted from ref. [267].

### 3.1.6 Detection of dopamine release from PC-12 cells.

To initially characterize the response of the biohybrid synapse to dopamine, the transfer curves of the neuromorphic device coupled with PC-12 cells were measured. In detail, cells were plated at two different cell densities (**Materials and Methods 2.6**), labelled after 2 hours with with Calcein-AM and propidium iodide (**Materials and Methods 2.7**), and observed *via* fluorescence imaging (**Figure 3.6 A, B**) Here, the higher cell density show a total coverage of the neuromorphic channel area. Furthermore, the presence of a high number of cells causes an increase in the transconductance peak  $g_m$ , due to the higher amount of dopamine molecules released at the cell-electrode interface (**Figure 3.6 C**). However, when measuring the dopamine-mediated modulation of the biohybrid synapse in response to a sequence of post-synaptic voltage pulses ( $V_{\text{post}} = 0.3 \text{ V}$ ,  $\text{PW} = 2 \text{ s}$ ), the higher cell density induced a physical “barrier” effect due to the dense

network of cells preventing the efficient oxidation of dopamine at the post-synaptic electrode. Therefore, the conductance modulation observed in case of a highly packed cell layer (**Figure 3.6 D**) is lower compared to the low cell density condition (**Figure 3.6 E**).

After the first sequence of gate voltage pulses, the device was returned to the incubator for 2 hours: interestingly, the conductance state of the OECT remained nearly at the same level reached during the previous measurement due to the long-term plasticity effect. In fact, during the 2-hours incubation time, dopamine continued to accumulate at the post-synaptic electrode and the application of another sequence of post-synaptic voltage pulses resulted in a 40% larger (long-term potentiation)  $\Delta G_{\text{post}}$ . From the calibration curve shown in **Paragraph 3.1.4 (Figure 3.4 C)**, the concentration of dopamine released from PC-12 cells at the synaptic cleft was estimated as 10 – 15  $\mu\text{M}$  and 15 – 20  $\mu\text{M}$  after 2 and 4 hours of incubation, respectively.

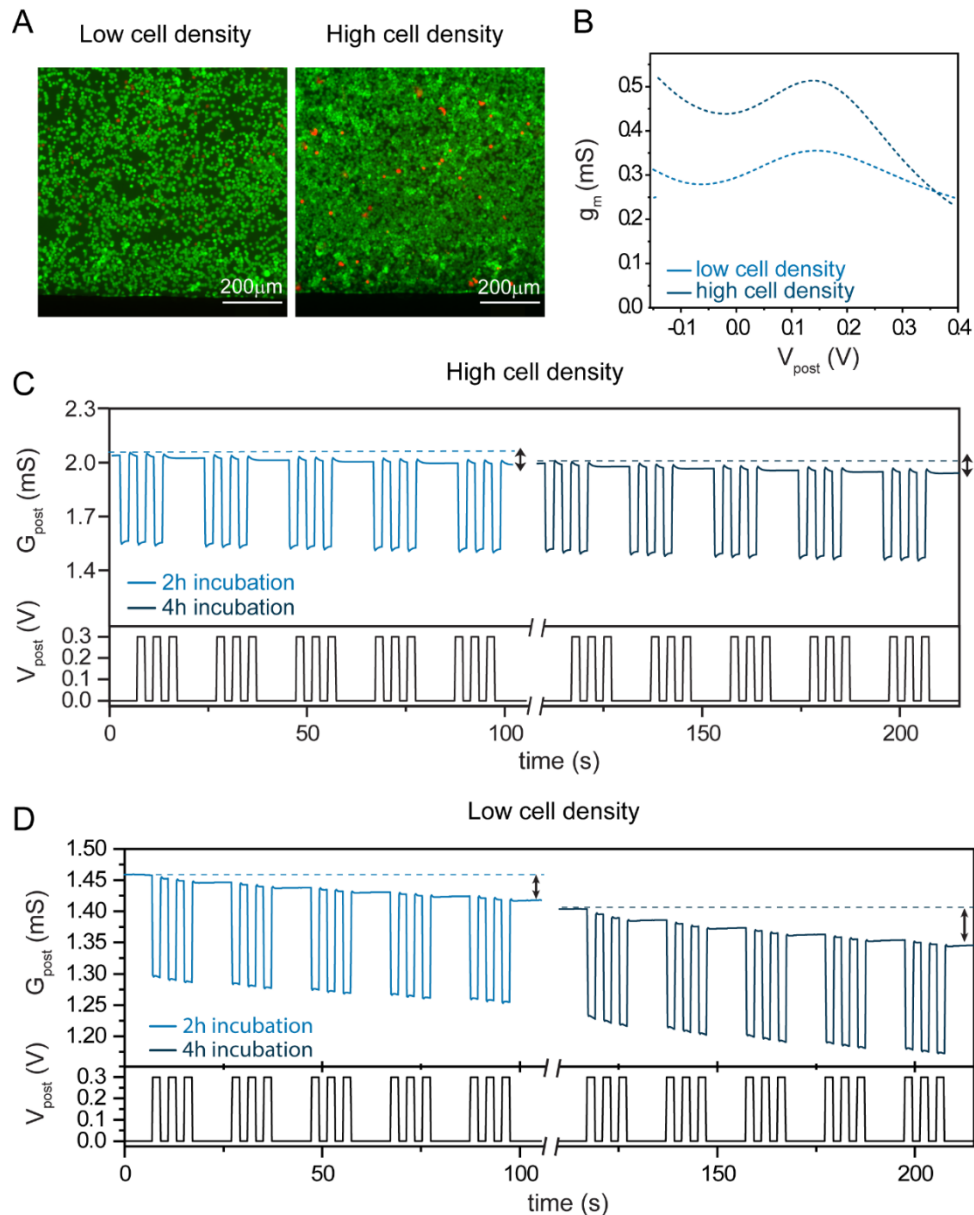


**Figure 3.6. Dopamine-mediated plasticity in the biohybrid synapse.** The figure reports a comparison between low and high cell density. A) Live/dead staining performed on PC-12 cells inside the microfluidic channel: the fluorescence micrographs provide an idea of the packed area of the channel. B) Transconductance of the neuromorphic device measured with low (light blue) and high (dark blue) PC-12 cell densities. C) Channel conductance modulation elicited by the application of pulsed bias at the gate in presence of high cell density on the neuromorphic channel. D) Channel conductance modulation elicited by the application of pulsed bias at the gate in presence of low cell density on the neuromorphic channel. Adapted from ref. [267].

After applying the pulsed bias at the gate electrode, a biocompatibility assay was performed as described in **Materials and Methods 2.7** to investigate the possible cytotoxicity of the neuromorphic device (**Figure 3.7 A**): the low number of dead cells confirms the high biocompatibility of the substrates and demonstrates

that the electrical measurements do not negatively affect the cell viability as previously reported [275,276]. Finally, the long-term stability of the biohybrid platform was investigated (**Figure 3.7 B**): the device remained responsive even after 24 hours in the incubator confirming both the high stability of PEDOT:PSS electrodes in biological media, as well as the excellent biocompatibility of the device surface.

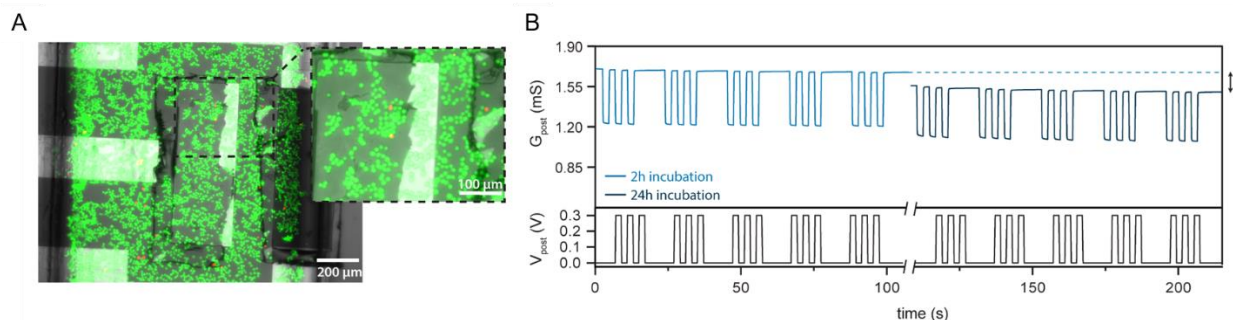
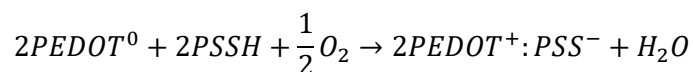


**Figure 3.7. Long-term stability of the biohybrid synapse.** A) Live/dead staining performed on PC-12 cells inside the microfluidic channel after applying repeated pulsed bias at the gate electrode: the green fluorescence confirms no alteration of cell viability from the electrical measurements. B) Comparison of conductance modulation elicited in the biohybrid synapse after 2 hours (light blue line) and after 24 hours (blue line) following cell plating. The efficiency of the device remains unaltered since synaptic plasticity behavior from dopamine oxidation is retained following extended exposure to the cell culture media. Adapted from ref. [267].

### 3.1.7 Dynamic response of the biohybrid synapse.

In biological synapses, once the information has been transmitted from the pre to the post-synaptic neuron, the neurotransmitters are cleared from the synapse through enzymatic degradation or re-uptake by specific transporters (**Figure 3.8 A**). In order to emulate the neurotransmitter recycling process [277] and characterize the dynamic response of the biohybrid synapse, the microfluidic system was used to refresh the electrolyte solution at the cell-device interface. Here, during steady-state measurements ( $V_{\text{post}} = 0.3 \text{ V}$ ,  $V_{\text{ch}} = -0.2 \text{ V}$ ) low flow rate ( $200 \mu\text{L}/\text{min}$ ) allowed the continuous accumulation and oxidation of dopamine released at the cell/PEDOT:PSS interface with the consequent decrease of post-synaptic conductance  $G_{\text{post}}$  (**Figure 3.8 B**, light blue area). On the other hand, at high flow rate ( $300 \mu\text{L}/\text{min}$ ) dopamine is washed away from the synaptic cleft before it can oxidize, emulating endocytosis. Furthermore, a memory recovery and increased  $G_{\text{post}}$  is observed (**Figure 3.8 B**, dark blue area): such behavior is the result of the competing effects of dopamine oxidation and reduction of oxygen dissolved in the electrolyte solution. Here, two protons and two electrons can be donated from neutral PEDOT to oxygen to form water, according to the following reaction [235,278]:



where PEDOT is oxidized to its conductive state and therefore  $G_{\text{post}}$  increases. Additionally, performing measurements under microfluidic conditions enhances such memory recovery as the fresh solution contains dissolved oxygen which is constantly replenished at the interface.

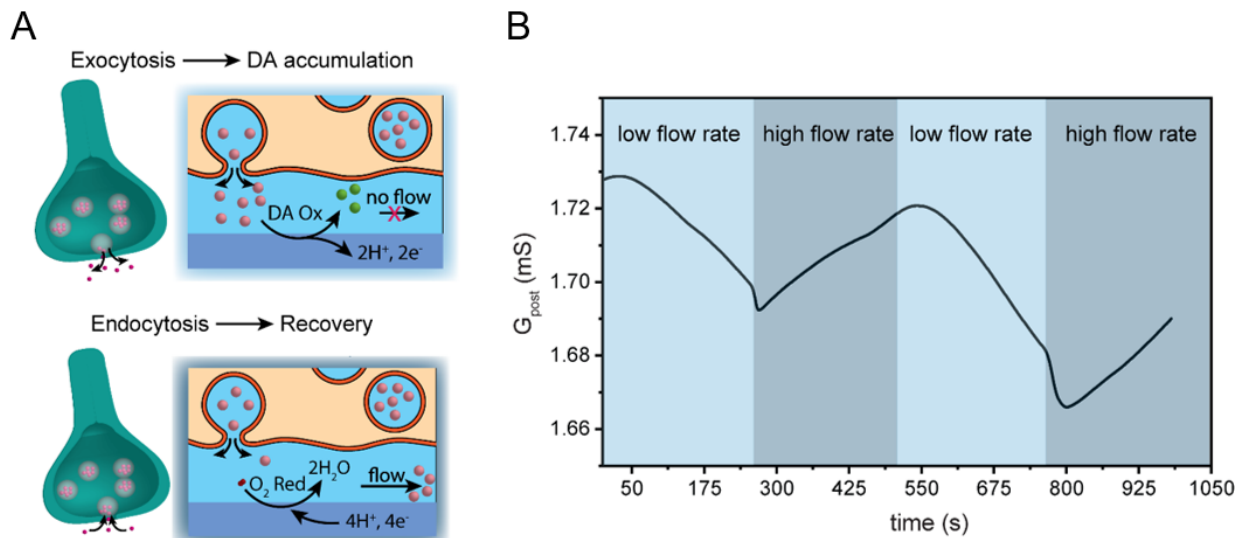


**Figure 3.8. Dynamic response of the biohybrid synapse.** A) Schematics depicting the exocytosis and endocytosis of neurotransmitter at the synaptic cleft in biological synapses. B) Channel conductance modulation of the biohybrid platform measured under a constant postsynaptic gate voltage ( $V_{\text{post}} = +0.3$  V) and under microfluidic flow to emulate neurotransmitter endocytosis. Adapted from ref. [267].

### 3.1.8 Characterization of the lower limit response of the biohybrid synapse.

In biological synapses the initiation of LTP can take place also in a short period of time (milliseconds to few minutes) as the dopamine at the synaptic cleft is immediately uptaken from the post-synaptic receptors [279,280]. To emulate this, PC-12 cells were stimulated with KCl solution to elicit the instantaneous release of dopamine and monitor the device response to post-synaptic pulses (**Materials and Methods 2.11**). Indeed, it has been demonstrated that KCl causes cell membrane depolarization inducing the aperture of voltage-gated ion channels: the consequent influx of  $\text{Ca}^{2+}$  ions within the membrane triggers the exocytosis of dopamine [281,282].

As shown in **Figure 3.9**, when dispensing 60 mM KCl, the dopamine released at the interface in the short time scale of the measurement ( $\sim 2$  mins) is not sufficient to elicit the device response during gate voltage pulsing (**Figure 3.9 A**). On the other hand, when exposed to 120 mM KCl, PC-12 cells release dopamine at a faster rate so that it can accumulate at the interface and the application of post-synaptic voltage pulses

induces long-term potentiation of the biohybrid synapse (**Figure 3.9 B**). As in biological systems synaptic strength can be modulated even by few vesicle release events (several dozen) <sup>[280]</sup>, here the sensitivity of the neuromorphic device to dopamine was achieved by adjusting the geometrical parameters of the device: reducing the area of the PEDOT:PSS channel, a lower number of charges and oxidation events can produce a response in the device. Indeed, PEDOT:PSS has a fixed charge (hole) carrier density,  $p = \text{ca. } 5 \times 10^{20}$  holes  $\text{cm}^{-3}$ , whereas the change in conductivity of PEDOT:PSS elicited by dopamine oxidation is related to the absolute number of charges by the following equation:

$$\Delta G = \Delta p * e * \mu * \frac{d * W}{L} = \frac{\Delta P}{d * W * L} * e * \mu * \frac{d * W}{L} = \frac{P_0 - \int I_{ox,DA} dt}{L^2} * e * \mu$$

where  $\Delta G$  is the variation of channel conductance,  $\Delta p$  is the variation of charge carriers (hole) density,  $e$  is the elementary charge ( $1.602 \times 10^{-19}$  C),  $\mu$  is the mobility of charges in PEDOT:PSS,  $d$  is the PEDOT:PSS film thickness,  $W$  is the device width,  $L$  is the device length,  $P_0$  is the absolute number of charge carriers equal by  $P_0 = 5 \times 10^{20} * t * W * L$ , and  $I_{ox,DA}$  is the oxidation current during a voltage pulse at the gate electrode which is integrated over the time  $dt$  to obtain the number of injected charges. Therefore, reducing the device dimensions  $W$  and  $L$ , the same integrated oxidation current induces a larger variation in carrier concentration  $\Delta p$ , resulting in enhanced channel conductance modulation  $\Delta G$ . As expected, for a fixed dopamine concentration (*i.e.*,  $10^{-5}$  M), neuromorphic devices with a smaller channel area (**Figure 3.9 C**, red curve) displays enhanced conductance change compared to the OECT with larger channel (**Figure 3.9 C**, grey curve). Finally, decreasing the channel dimension at  $300 \mu\text{m}^2$  (**Figure 3.9 C**, blue curve) reduces the detection limits of the device up to 100 nM dopamine solution as also previously reported <sup>[283–285]</sup>.

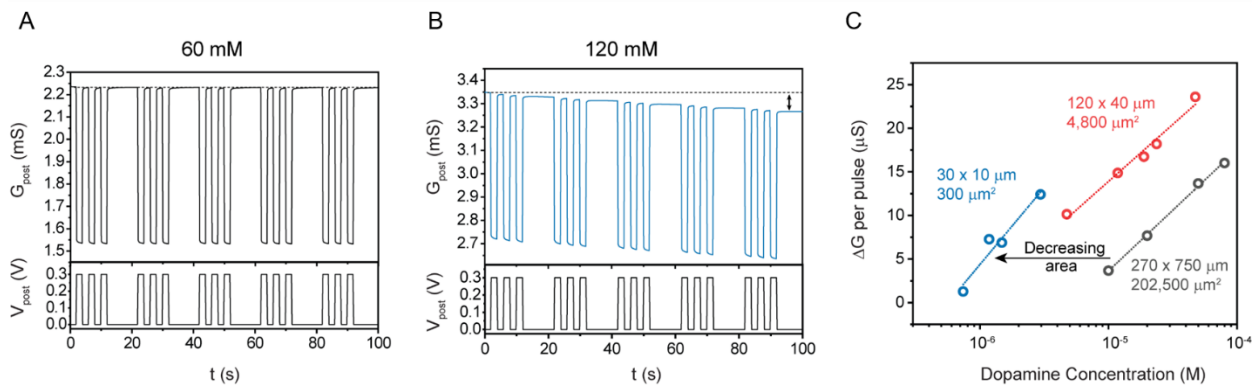


**Figure 3.9. Lower limit response of the biohybrid synapse.** A) Conductance modulation elicited by postsynaptic voltage pulses applied at the gate electrode after PC-12 cells stimulation with 60 mM KCl

solution. B) Conductance modulation in response to postsynaptic voltage pulses applied when PC-12 cells are stimulated with 120 mM KC solution. C) Dopamine-mediated conductance modulation of scaled neuromorphic devices: the conductance change is measured per pulse ( $V_{\text{pulse}} = 0.3 \text{ V}$ ,  $t_{\text{pulse}} = 2 \text{ s}$ ). Measurements are performed in the absence of microfluidic flow. Adapted from ref. [267].

## 3.2 Engineering a lipid bilayer-based biomimetic synapse

As discussed earlier (**Paragraph 3.1**), OECTs might emulate the learning process of neurons showing dopamine-mediated long-lasting memory upon periodic stimulation <sup>[267]</sup>. However, such artificial synapses still lack biomimetic features, which could promote their seamless integration within the neuronal network. For this, the second part of this thesis project was focused on the coupling of an organic neuromorphic device with supported lipid bilayers (SLBs) to engineer a biomimetic *in-vitro* synapse. In particular, the role of the synthetic membrane on the OECT short-term plasticity was investigated, exploring also different positioning of the gate electrode to explore whether this could facilitate or further inhibit the ions flow through the membrane with consequent effects on the short-term memory.

### 3.2.1 Investigation of the gate role on OECT short-term potentiation.

Here, an organic neuromorphic device made of PEDOT:PSS was fabricated using a glass substrate with ITO pads to contact the source, drain and gate electrodes; the PEDOT:PSS active layer was deposited through a selective dry etching procedure (**Materials and Methods 2.2**). The neuromorphic operation of the OECT was characterized applying a sequence of positive voltage pulses at the gate electrode, while monitoring the output channel current (**Materials and Methods 2.3**). Furthermore, in order to evaluate if the gate positioning might affect the STP of the artificial synapse, two different configurations of the OECT were explored, varying the position of the PEDOT:PSS gate electrode in respect to the neuromorphic channel to obtain a planar and a top-gate OECT (**Figure 3.10 A**).

In both configurations, the sequence of pulses applied at the gate electrode was varied to modulate the PEDOT:PSS channel conductance. The pulsed input indeed, is characterized by the voltage amplitude ( $A$ ) which drives the ions from the electrolyte into the PEDOT:PSS channel, the pulse width ( $PW$ ) and the time interval between consecutive pulses ( $\Delta t$ ) (**Figure 3.10 B**). The latter, in particular, has emerged as fundamental parameter for modulating the OECT conductance: the application of the pulsed voltage at the gate electrode induces a reversible de-doping of the PEDOT:PSS channel due to cations injected into the bulk of the polymer film <sup>[112]</sup>. When  $\Delta t$  is long enough to allow charge equilibrium before the application of a second pulse, the polymer is doped to its initial state; high frequency pulses, instead, force cations to remain trapped in the PEDOT:PSS channel causing a cumulative de-doping intended as a ‘memory effect’ which recalls the STP of biological synapses <sup>[232]</sup>. Therefore, the temporal response of the neuromorphic device in the planar and top configurations was investigated upon the application of a 6-pulses gate bias (fixed amplitude and width) with decreasing  $\Delta t$ . Here, when  $\Delta t = 7$  seconds a reversible de-doping of the PEDOT:PSS channel is observed, inducing a complete recovery of the initial channel conductance (**Figure 3.10 C-i**), therefore no memory effect is observed. For  $\Delta t = 1$  second, the device starts displaying STP (**Figure 3.10 C-ii**) as  $\Delta t$  is insufficient to allow cations injected in the polymeric channel to return into the

electrolyte before the application of the subsequent pulse. Here, the conductance modulation  $\Delta G$  is further enhanced when decreasing  $\Delta t$  from 1 to 0,5 seconds (**Figure 3.10 C-iii**). Interestingly, at a given  $\Delta t$ , the planar and top-gate OECT elicit the same conductance modulation confirming that the gate position does not have any relevant effect on the OECT short-term memory (**Figure 3.10 D**).

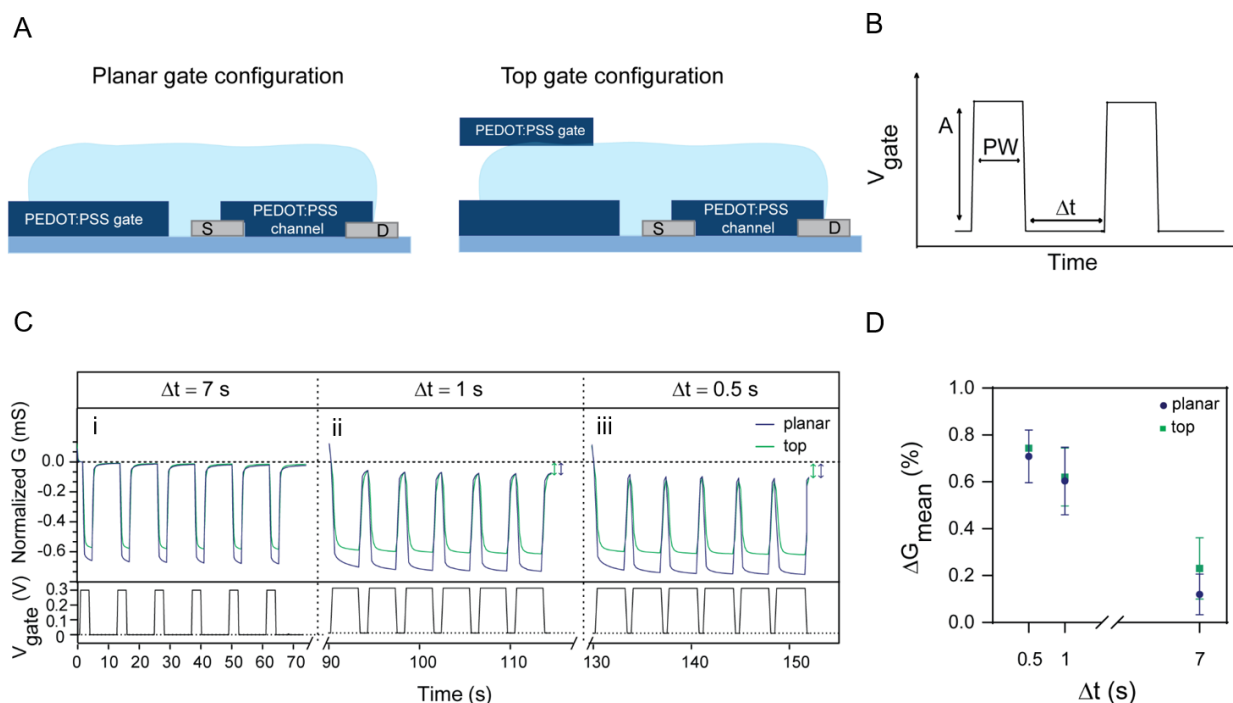
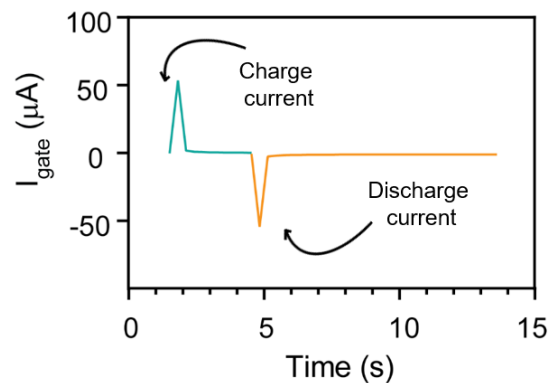


**Figure 3.10. Short-term potentiation of planar and top-gate unfunctionalized OECT.** A) Schematics of OECT architectures with planar gate electrode and PEDOT:PSS top gate. B) Graph of the voltage pulsed input applied at the gate electrode, showing the pulse amplitude, duration of the pulse (PW) and delay between pulses ( $\Delta t$ ). C, D) Conductance modulation elicited in the planar and top gate configurations by gate voltage pulses with variable  $\Delta t$ . Mean  $\Delta G$  calculated from 3 independent experiments. Adapted from ref. [286].

In order to investigate the ionic mechanism behind the conductance modulation elicited by the two gate configurations during the application of a 6-pulses gate bias, the gate current (*i.e.*, the current measured between the gate and source electrodes) was integrated to calculate the number of cations injected from the gate and retained in the neuromorphic channel during each pulse. In particular, the percentage of retained charge was calculated as follows:



$$\frac{(\text{returning charges} - \text{injected charges})}{\text{injected charges}} \times 100$$

**Figure 3.11. Gate current integration.** Graph displaying gate current measured during the application of gate voltage pulses: the light blue line corresponds to the current measured during the ON phase of the pulse (charge current), while the orange line is the current measured during the OFF phase of the pulse (discharge current). Adapted from ref.

where the returning and injected charges were obtained integrating the discharge (**Figure 3.11**, orange line) and charge current (**Figure 3.11**, light blue line) respectively. **Figure 3.12** reports the charge analysis of a single exemplary experiment for gate voltage pulses with  $\Delta t = 7$  seconds (left column),  $\Delta t = 1$  second (middle column),  $\Delta t = 0.5$  seconds (right column). Here, the graphs depicts how the number of injected charges (**Figure 3.12 A-i-ii-iii**) is approximately the same when decreasing the pulse delay, while the number of cations retained in the PEDOT:PSS channel increases (**Figure 3.12 B-i-ii-iii**), resulting in a conductance modulation (**Figure 3.12 C-i-ii-iii**).

Interestingly, the highest amount of charges is retained during the first pulse when the PEDOT:PSS channel is completely doped and therefore all negative charges of the PSS molecules can be compensated by cations entering the bulk of the polymer<sup>[232]</sup>. During the subsequent voltage pulses instead, since the neuromorphic channel is already partially de-doped, the number of ions retained in the polymeric film is lower. As expected, for each pulse delay, the two different gate configurations exhibit the same behavior with same amount of injected and retained charges; furthermore, in agreement with the working mechanisms of OECTs where the conductivity of the PEDOT:PSS channel is modulated by the number of cations trapped in the bulk of the polymer<sup>[231]</sup>, here the  $\Delta G$  values follow the same behavior of the charge retention, confirming that the planar and top gate elicit the same conductance modulation.

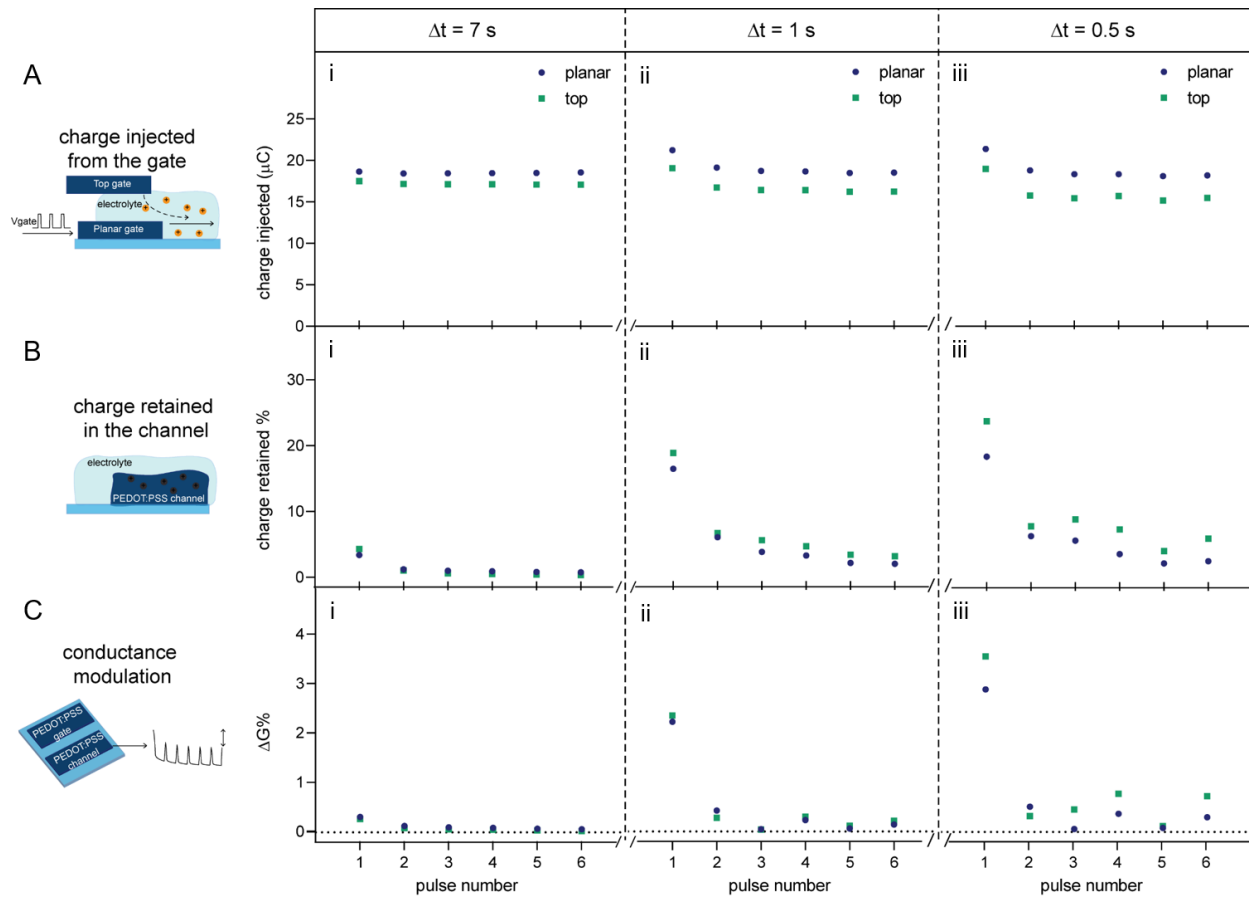


**Figure 3.12. Ionic charge analysis in the unfunctionalized OEET.** Graphs report data obtained from the integration of the gate current measured during the application of gate voltage pulses (6 pulses) with varying  $\Delta t$ . A) Number of charges injected from the gate (during the ON pulse phase); B) percentage of charges retained into the PEDOT:PSS channel after pulse removal; C) Conductance modulation calculated for every single pulse of the gate voltage applied. Graphs report data of a single exemplary experiment. Adapted from ref. [286].

### 3.2.2 Investigation of pulse delays to enhance short-term potentiation.

As discussed in **Paragraph 3.2.1**, the STP of the artificial synapse can be modulated varying  $\Delta t$  in the applied gate input. Here, we investigated the influence of  $\Delta t$  in order to increase the ions migration from the electrolyte into the neuromorphic channel and consequently enhance the STP of the artificial synapse. In OEETs, the movement of ionic species can be modelled through an equivalent ionic RC circuit where the resistor and the capacitor are connected in series (**Figure 3.13 A**)<sup>[112,287]</sup>. Here, the resistive part accounts for the ion flow through the electrolyte, while the capacitance models the accumulation of charges inside the bulk of the conducting polymer. Therefore, the electrochemical doping/de-doping of the PEDOT:PSS channel can be described as the charge/discharge of the equivalent RC circuit and is characterized by a time constant ( $\tau$ ). In particular, such parameter also refers to the time needed to charge the equivalent circuit

from the discharged state to the 63.2% of its maximum charge, or equivalently, as the time needed to discharge about 37% of its fully-charged state [288]. Furthermore, such electrical RC circuit can be fully charged/discharged after  $5\tau$  (see **Annex F** for detailed numerical computation), suggesting that the time constant  $\tau$  might be exploited to tune the neuromorphic properties of artificial synapses. For this, here different sequences of voltage pulses were applied at the gate electrode varying  $\Delta t$  as multiple values of  $\tau$  to modulate the conductivity (and STP) of the PEDOT:PSS channel switching the polymer from fully to partial de-doped state.

First of all, as  $\tau$  strongly depends on the dimensions and geometry of the neuromorphic platform [287], here the numerical value of  $\tau_{\text{OECT}}$  was calculated both for the planar and top configurations, applying a sequence of voltage pulses at the gate electrode and then setting a threshold in the channel current during the post-processing (**Materials and Methods 2.14.2**) to identify the time needed to charge the neuromorphic channel up to the 63% (**Figure 3.13 B**). The top gate OECT exhibited slightly higher time constant ( $\tau_{\text{OECT-top}} = 0.429 \pm 0.049$  seconds) compared to its planar counterpart ( $\tau_{\text{OECT-planar}} = 0.32 \pm 0.01$  seconds) probably due to the higher volume of electrolyte that connects the gate and channel in the top configuration: indeed, this might influence the response time of the device as the migration of ions into the PEDOT:PSS channel requires longer time [289].

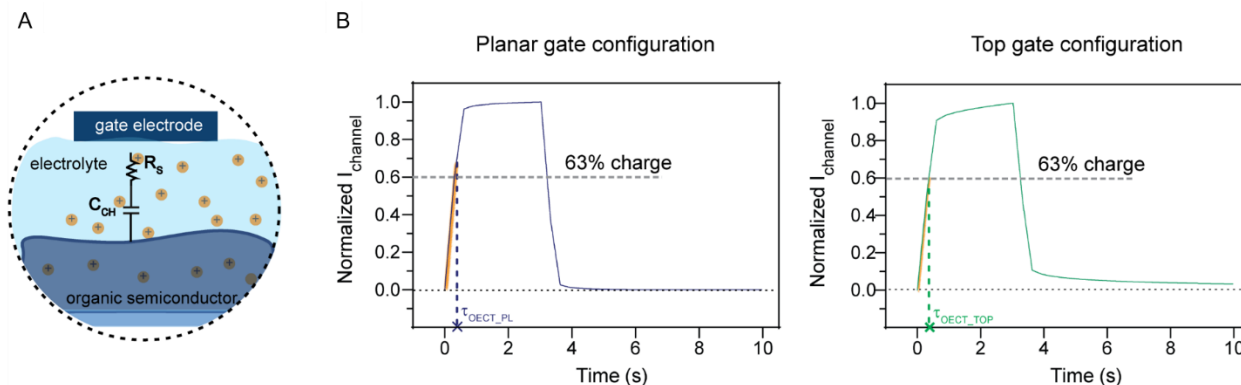


**Figure 3.13. Electrical modelling and time response of the unfunctionalized OECT.** A) Schematics of the electrical circuit modelling ionic conduction in OECTs. B) Channel current response for planar and top gate configurations elicited by the application of gate voltage pulse with  $\Delta t = 7$  s: the dashed horizontal lines represent the current threshold set to calculate the time response of the device. Adapted from ref. [286].

Then, in order to investigate how  $\tau_{\text{OECT}}$  could modulate the STP of the artificial synapse, voltage pulses with  $\Delta t$  equal to multiple values of  $\tau_{\text{OECT}}$  (from  $1 \tau_{\text{OECT}}$  to  $5 \tau_{\text{OECT}}$ ) were applied at the gate electrode (both in planar and top configurations), while monitoring the output channel current. As shown in **Figure 3.14**, both gate configurations show a relevant conductance decrease for  $\Delta t$  equal to  $1 \tau_{\text{OECT}}$  (**Figure 3.14 A-i** and

**B-i)** and  $2 \tau_{\text{OECT}}$  (**Figure 3.14 A-ii** and **B-ii**) where the short delays between pulses do not allow the ionic discharge of the PEDOT:PSS channel and therefore induces a STP in the OECT. On the other side instead, pulse delays equal to  $3 \tau_{\text{OECT}}$  (**Figure 3.14 A-iii** and **B-iii**),  $4 \tau_{\text{OECT}}$  (**Figure 3.14 A-iv** and **B-iv**) and  $5 \tau_{\text{OECT}}$  (**Figure 3.14 A-v** and **B-v**) allowing charge equilibrium, enable almost the complete recovery of PEDOT:PSS initial conductance, in agreement with literature where the RC circuit which models the ionic conductivity in OECTs is completely charged/discharged after  $5 \tau$  [288].

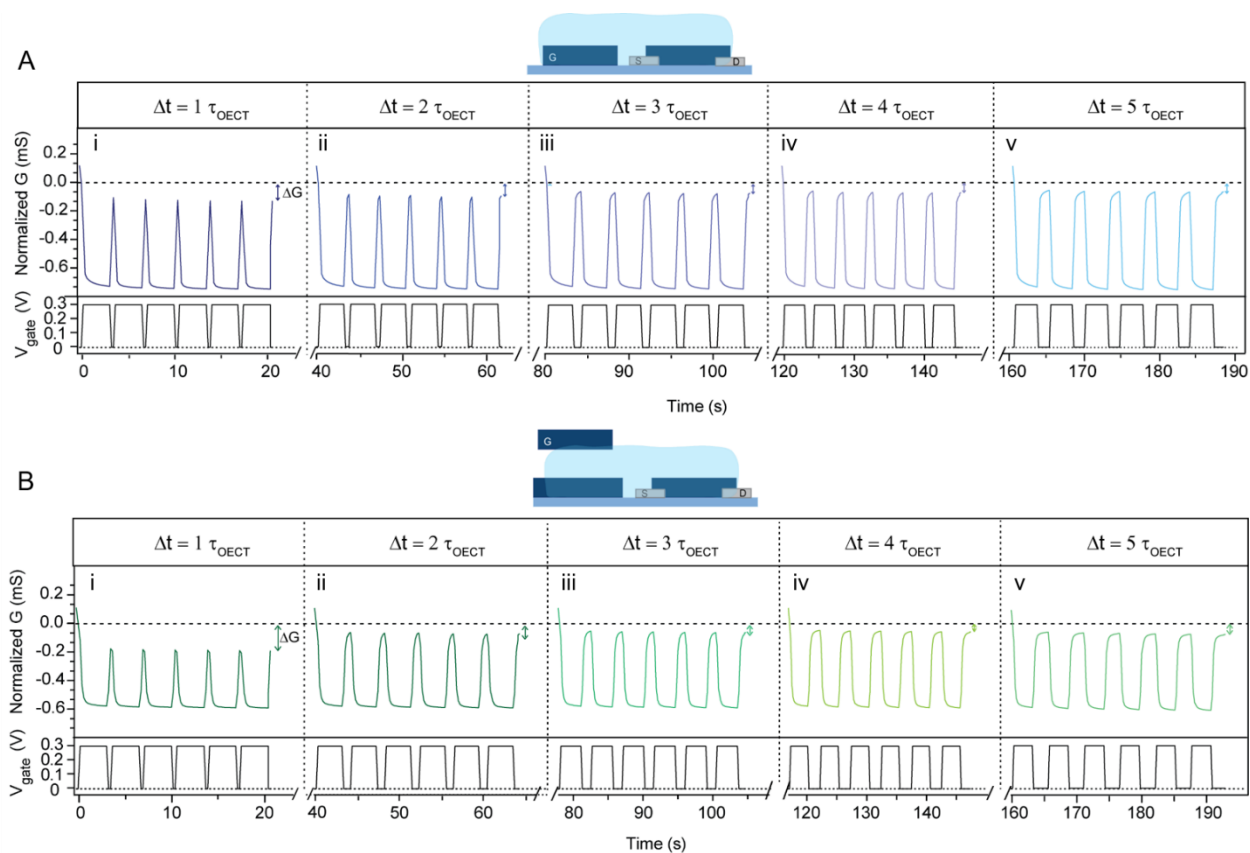


**Figure 3.14. Short-term potentiation of the unfunctionalized OECT in response to gate voltage pulses with  $\Delta t$  set as multiple values of  $\tau_{\text{OECT}}$ .** A) Conductance modulation for planar unfunctionalized OECT elicited by gate voltage pulses with  $\Delta t$  set as multiple values of  $\tau_{\text{OECT}}$  ranging from 1 to  $5 \tau_{\text{OECT}}$ . B) Conductance modulation for the top gate unfunctionalized OECT elicited by gate voltage pulses with  $\Delta t$  set as multiple values of  $\tau_{\text{OECT}}$  ranging from 1 to  $5 \tau_{\text{OECT}}$ . Adapted from ref. [286].

### 3.2.3 Formation and characterization of the supported lipid bilayer.

As described in **Paragraph 1.4.2** SLBs offer an optimal approach to engineer biomimetic *in-vitro* platforms, as they present the same lipid composition of biological membranes. Here the artificial synapse was functionalized with a phosphatidylcholine -based supported lipid bilayer assembled from POPC that is one of the major component of biological membranes and facilitates the formation of a fluid and

homogeneous bilayer. In particular, as the formation of SLBs on conductive polymers requires a solvent-assisted procedure (SALB) <sup>[142]</sup>, the OECT was coupled with a microfluidic channel which enables both the confinement of POPC liposomes at the gate/channel area and the solvent exchange needed to induce vesicles rupture (**Materials and Methods 2.12.2**). Then, as the SLB assembled on the OECT interfaces both the rigid glass and the PEDOT:PSS gate and channel, to investigate how these alternating surfaces affect the SLB formation, its outward architecture and uniformity, the bilayer fluidity and its surface profile were characterized using FRAP and AFM techniques.

Fluidity and homogeneity of the lipid bilayer were validated by means of FRAP (**Materials and Methods 2.12.3**). As shown in the fluorescence intensity profiles reported in **Figure 3.15**, the complete fluorescence intensity is recovered within 5 minutes and the POPC lipid molecules exhibit high lateral mobility when the SLB is formed both on PEDOT:PSS (**Figure 3.15 A**) and glass (**Figure 3.15 B**). Additionally, fluorescence intensity profiles show a maximum value ( $F_{\max}$ ) that is lower when the bilayer is formed on the polymeric film ( $F_{\max\text{-PEDOT:PSS}} \sim 30$ ,  $F_{\max\text{-glass}} \sim 80$ ). This suggests that the presence of the conductive polymer might attenuate the fluorophore activity inserted within the SLB: indeed, lipid molecules were labelled with Texas Red (**Materials and Methods 2.12.1**), a red fluorophore with  $\lambda_{\text{EM}} = 615$  nm, and, as reported from previous studies, the transmittance of PEDOT:PSS films is maximum for incident light with wavelengths in the blue region of the visible spectrum, while it decreases when moving into the red region <sup>[290]</sup>.

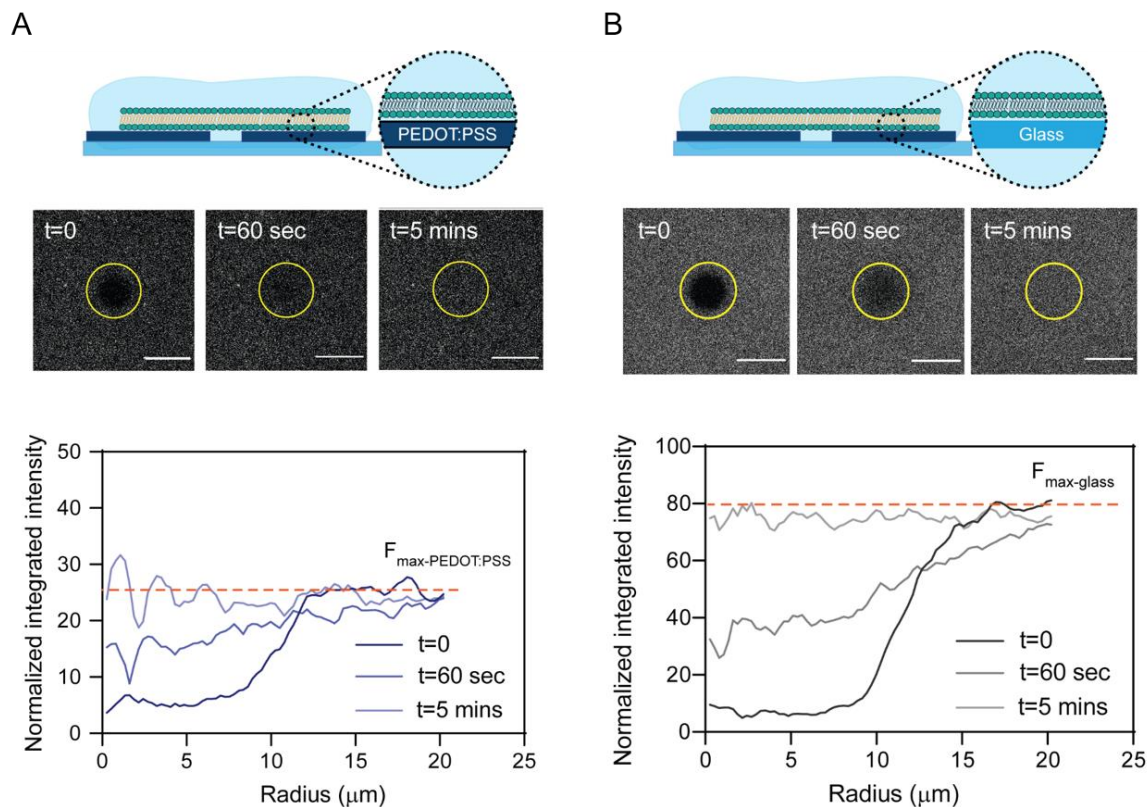


**Figure 3.15. FRAP characterization of POPC SLB on OECT surface.** A) FRAP snapshots and fluorescence intensity profiles at different time points after photobleaching for the POPC bilayer assembled on PEDOT:PSS. B) FRAP snapshots and fluorescence intensity profiles at different time points after photobleaching for the POPC bilayer assembled on glass (B). Scale bar: 50 μm. Adapted from ref. [286].

Furthermore, the estimation of the SLB diffusion coefficients (**Table 3.1**) suggests that the different surface morphology and rigidity might affect the lipid mobility within the membrane: indeed, the area of the SLBs which interfaces the PEDOT:PSS film presented higher fluidity, compared to bilayer regions in contact with the rigid glass, suggesting a ‘cushion effect’ of the polymer which reduces the frictional coupling between the lipid membrane and the underlying substrate <sup>[291]</sup>.

Surface	Diffusivity [ $\mu\text{m}^2/\text{s}$ ]
POPC on PEDOT:PSS	$1.58 \pm 0.18$
POPC on glass	$1.30 \pm 0.18$

**Table 3.1. Diffusion coefficients of POPC bilayer on PEDOT:PSS and glass.**

The local roughness of the SLB and its surface profile were determined using tapping mode AFM in liquid (**Materials and Methods 2.12.4**). As shown in **Figure 3.16 A-i**, the PEDOT:PSS films prior to the SLB assembly, display a characteristic fuzzy surface morphology with sharp-cornered structures <sup>[292,293]</sup>; after the bilayer formation instead, the indented surface texture became smoother, suggesting an homogeneous lipid coverage (**Figure 3.16 A-ii**). On the other hand, bare glass exhibits a coarse morphology (**Figure 3.16 B-i**), whose domains become more defined and sphere-like after the bilayer formation (**Figure 3.16 B-ii**).

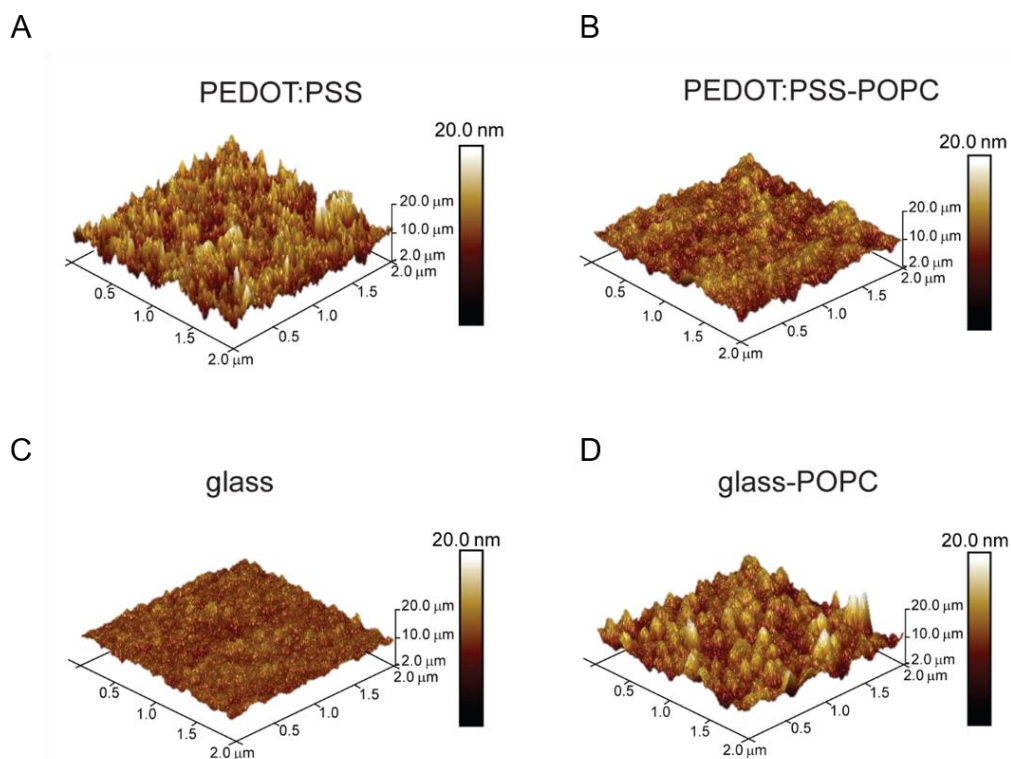


**Figure 3.16. AFM characterization of POPC SLB on OECT surface.** A) AFM 3D images of the surface morphology of bare PEDOT:PSS; B) AFM 3D images of the surface morphology of POPC bilayer formed on PEDOT:PSS; C) AFM 3D images of the surface morphology of bare glass; D) AFM 3D images of the surface morphology of POPC assembled on glass. Adapted from ref. [286].

Interestingly, the analysis of the RMS roughness ( $R_q$ ) (**Materials and Methods 2.14.2**) highlighted a less predominant unevenness of the bilayer structure when formed on PEDOT:PSS ( $R_q=27\%$ ) than in the case

of glass surfaces ( $R_q=31\%$ ), demonstrating how the substrate morphology affects the SLB structure (**Table 3.2**)<sup>[294]</sup>.

Surface	$R_q$ [nm]
PEDOT:PSS	$2.27 \pm 0.24$
POPC on PEDOT:PSS	$1.64 \pm 0.18$
Glass	$1.70 \pm 0.58$
POPC on glass	$2.23 \pm 0.46$

**Table 3.2. Roughness values of POPC bilayer on PEDOT:PSS and glass.**

### 3.2.4 Investigation of the gate role on the short-term potentiation in the biomimetic synapse.

As the structural and morphological characterization of the SLB confirmed the formation of a homogeneous and fluid bilayer on the OEECT, the STP of the biomimetic synapse was investigated applying gate voltage pulses with different  $\Delta t$  as described in **Paragraph 3.2.1**, both in planar and top gate configurations. Of note, in the case of planar OEECTs, the SLB covers both gate and channel (**Figure 3.17 A**), while in the top configuration the gate surface is not hindered by the membrane (**Figure 3.17 B**). Furthermore, the top gate allows to replicate the mechanism of ions migration of biological systems, where the ions exchange from different cell compartments takes place across the lipid membranes with a transverse flow<sup>[295]</sup>; similarly, here ions are forced to cross the SLB when injected from the gate to the neuromorphic channel.

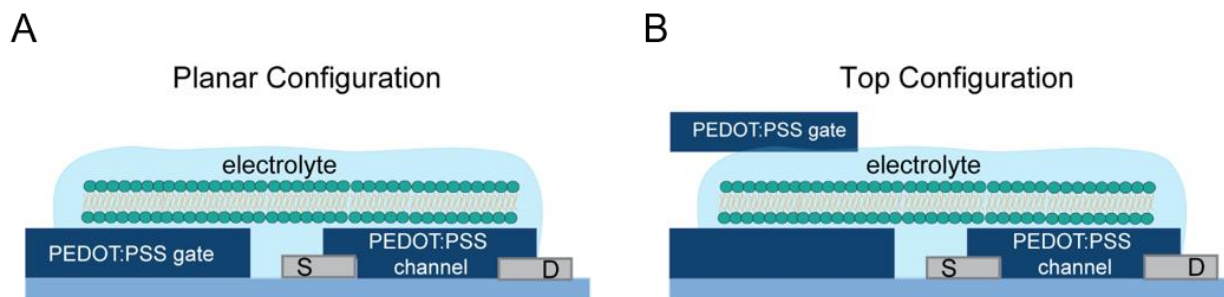


**Figure 3.17. Schematics of biomimetic synapse configurations.** A) Schematic of biomembrane-based OEECT architecture with planar gate electrode B) Schematic of biomembrane-based OEECT architecture with PEDOT:PSS top gate (B). Adapted from ref. [286].

**Figure 3.18** reports the channel conductance modulation elicited in the biomembrane-based OECT upon the application of a 6-pulses voltage gate bias. Similarly to the unfunctionalized device (**Paragraph 3.2.1**), also in this case the device displays a STP when  $\Delta t$  is decreased from 7 seconds (**Figure 3.18 A-i**) to 1 second (**Figure 3.18 A-ii**) and 0.5 seconds (**Figure 3.18 A-iii**) as the short time interval between pulses does not allow for a reversible doping of the organic polymer before the application of the subsequent pulse. Interestingly, unlike the unfunctionalized device where the gate positioning does not affect the STP of the OECT (**Paragraph 3.2.1**), here in presence of the POPC bilayer the top gate exhibits higher conductance modulation compared to the planar case (**Figure 3.18 B**).

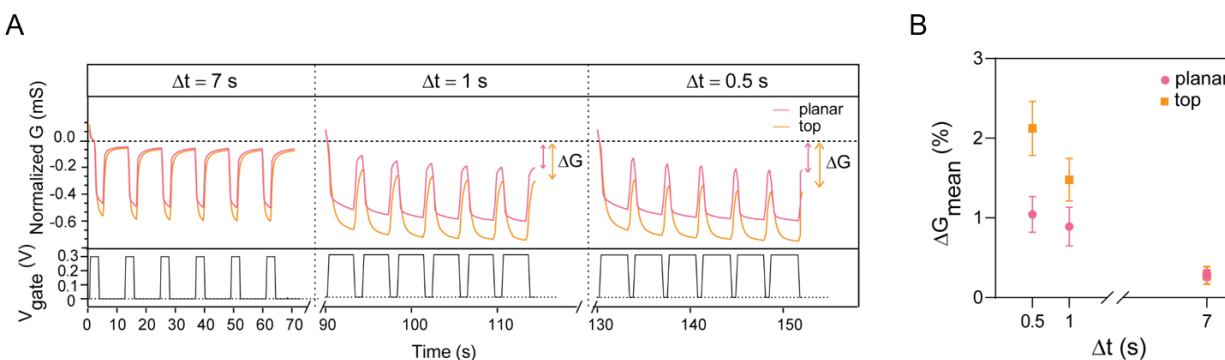


**Figure 3.18. Short-term potentiation for planar and top-gate biomimetic synapse.** A, B) Conductance modulation of the POPC-coated OECT elicited in the planar and top gate configurations by gate voltage pulses with variable  $\Delta t$ . Mean  $\Delta G$  were calculated from 3 independent experiments. Adapted from ref. [286].

In order to investigate the ionic mechanism underlying the STP of the biomembrane-based OECT, the number of injected/retained cations was calculated integrating the gate current measured during the application of a 6-pulses voltage gate bias (**Paragraph 3.2.1**). Here, as shown in **Figure 3.19**, in the planar configuration the presence of the bilayer at the gate electrode causes a decrease in the number of cations injected from the gate (**Figure 3.19 A-i, ii, iii**); on the other hand, for short pulse delays ( $\Delta t = 1$  second and 0.5 seconds) in the top gate OECT, the SLB enhances the charge retention into the PEDOT:PSS channel (**Figure 3.19 B-i, ii, iii**), therefore eliciting higher conductance modulation (**Figure 3.19 C-i, ii, iii**).

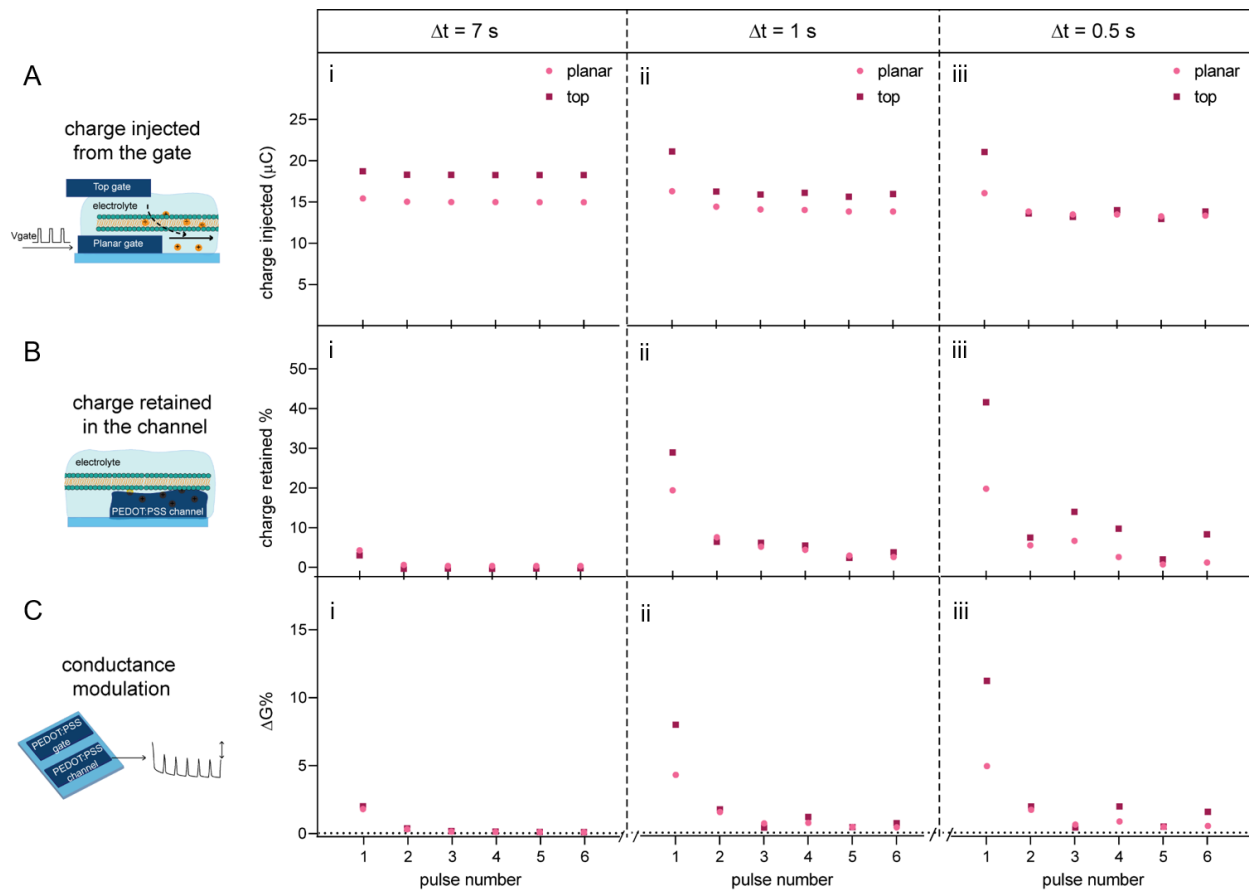


**Figure 3.19. . Ionic charge analysis in the biomimetic synapse.** Graphs report data of the biomembrane-based OECT obtained from the integration of the gate current measured during the application of gate voltage pulses (6 pulses) with varying  $\Delta t$ . A) Number of charges injected from the gate during the ON pulse phase; B) percentage of charges retained into the PEDOT:PSS channel after pulse removal. C), Conductance modulation calculated for every single pulse of the gate voltage applied. Graphs report data of a single exemplary experiment. Adapted from ref. [286].

### 3.2.5 Frequency response characterization of the biomimetic synapse.

To further investigate the different ionic paths promoted by the presence of the biomembrane, the frequency response of the neuromorphic device was investigated by means of EIS and planar impedance: the latter in particular accounts for the resistive paths between the gate and channel of the OECT neglecting the electrolyte resistance (**Materials and Methods 2.13**). In particular EIS was performed using an Ag/AgCl reference electrode placed above the SLB, while the neuromorphic channel was used as working electrode. Here, the Nyquist plots corresponding to bare (blue curve) and POPC-functionalized PEDOT:PSS (pink curve) films show how the presence of the SLB leads to an increase of the real value of the impedance, with the subsequent shift of the curve along the x-axis, and to the formation of a semicircle at high frequency

(**Figure 3.20 A**). These two phenomena denote an increased resistance in the path of ions and a slower charge accumulation at the electrode/electrolyte interface, respectively <sup>[121]</sup>.

In addition, the frequency response of the neuromorphic device using a planar measurement setup (**Materials and Methods 2.14**) was investigated: here, the impedance measured using the PEDOT:PSS gate and channel as reference and working electrodes, revealed that the presence of the bilayer causes a variation in the slope of the curve shown in the Nyquist plot suggesting spherical diffusion regime <sup>[121]</sup> (**Figure 3.20 B**). Impedance data referred to both EIS and planar frequency response characterizations, were fitted using the equivalent electrical circuit shown in **Figure 3.20 C**: here the resistance  $R_S$  accounts for the electrolyte solution resistance,  $R_{DL}$  and  $C_{DL}$  describe the membrane/electrode interface, while the Warburg element  $Z_W$  resolves the non-idealities of the conducting polymer electrodes, such as non-uniformity of the film thickness, ionic relaxation processes, swelling and interaction between redox sites and experimental artifacts <sup>[296]</sup>. Numerical values of  $R_S$ ,  $R_{DL}$  and  $C_{DL}$  computed through curve fitting are listed in **Table 3.3**: here, values obtained prior the formation of the bilayer describe the capacitive behavior of planar PEDOT:PSS electrode (first and third columns), which is reduced after SLB assembly as shown from decreased  $C_{DL}$  values observed both for EIS and planar frequency measurements. This findings describe the incorporation of the insulating bilayer between the electrode and the electrolyte <sup>[297]</sup>. Additionally, the SLB assembly might cause an increase in  $R_{DL}$  resistance in both measurements suggesting that the bilayer is correctly formed and, as expected, it behaves like a barrier, hindering the passage of ions. Interestingly, the  $R_{DL}$  extracted from the EIS doubles the one calculated from the planar frequency measurement, suggesting that cations are forced to cross the SLB when the reference electrode is positioned on top of the bilayer, and therefore account for a more resistive path. The marked SLB-resistive behavior found from EIS investigation supports the results obtained from the charge analysis shown in **Paragraph 3.2.4**, where, in the top gate configuration, the biomembrane enhances the percentage of charges retained in the neuromorphic channel, hindering the ionic discharge and the reversible doping of the organic polymer.

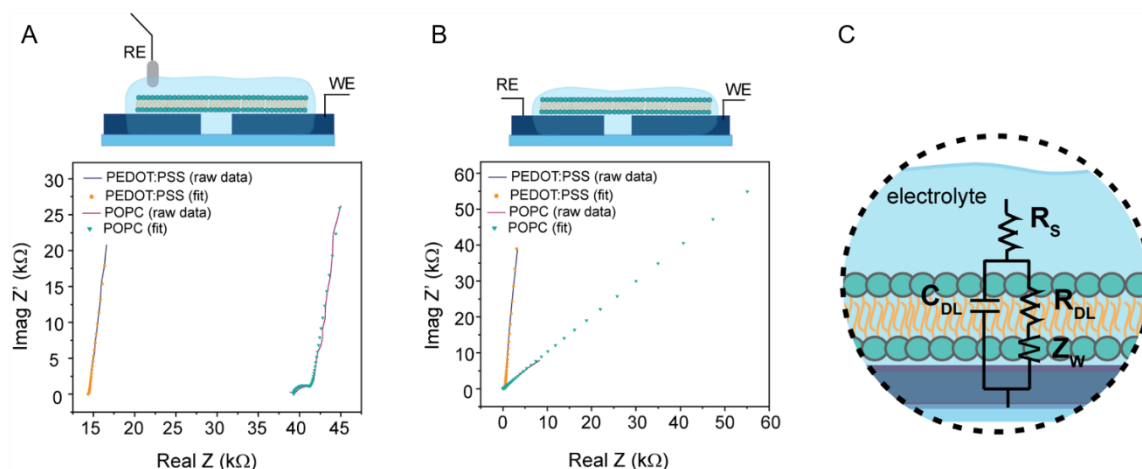


**Figure 3.20. Frequency response characterization of the biomembrane-based OECT.** A) EIS Nyquist plots, where the blue curve corresponds to bare PEDOT:PSS and the pink curve is given by the POPC-functionalized PEDOT:PSS. Dots represent the data fitting. B) Planar impedance Nyquist plots, where the blue curve corresponds to bare PEDOT:PSS and the pink curve is given by the POPC-functionalized PEDOT:PSS. Dots represent the data fitting. C) Equivalent electrical circuit used to fit the frequency response data. Adapted from ref. [286].

	EIS – PEDOT	EIS – SLB	IMPEDANCE PEDOT	IMPEDANCE SLB
$R_s$ [k $\Omega$ ]	$15.8 \pm 2.1$	$27.1 \pm 10.5$	$0.5 \pm 0.1$	$1.2 \pm 0.2$
$R_{DL}$ [ $\Omega$ ]	$356.3 \pm 197.9$	$2230.0 \pm 208.8$	$215.7 \pm 39.1$	$1156.7 \pm 89.6$
$C_{DL}$ [ $\mu$ F]	$8.1 \pm 0.6$	$4.8 \pm 2.3$	$10.6 \pm 1.8$	$6.4 \pm 2.3$

**Table 3.3. Numerical data of frequency response measurements obtained through circuitual fitting.**

### 3.2.6 Investigation of pulse delays to enhance short-term potentiation in the biomimetic synapse.

As shown in **Paragraph 3.24**, the resistive properties of the SLB influence the ionic conduction of the OECT according to the gate positioning. Here we investigated if the presence of the biomembrane affects also the time constant of the neuromorphic device, calculating the numerical value of  $\tau$  for the biomimetic synapse (named as  $\tau_{\text{OECT-SLB}}$ ), both for the planar and top configurations (**Materials and Methods 2.14.2**). As shown in **Figure 3.21 A-B**, in presence of the POPC membrane the pulse shape of the output channel current is smoother compared to the ones obtained for the unfunctionalized OECT, for both planar (**Figure 3.21 A**) and top configurations (**Figure 3.21 B**), suggesting a delay in the output current caused by the artificial membrane. Indeed, the computation of  $\tau_{\text{OECT-SLB}}$  revealed higher time response both for planar and top gate OECTs compared to their unfunctionalized counterparts (**Figure 3.21 C**); interestingly, such

increment is emphasized when the gate terminal is placed in the top configuration. This result additionally supports the hypothesis that the position of the gate electrode might elicit diverse ionic paths through the bilayer where cations are forced to cross the SLB barrier to reach the PEDOT:PSS channel, causing a significant delay in the top gate OECT response ( $\tau$  increases of 45%). On the other hand, in the planar gate device, ions might move in the aqueous cushion placed at the interface between the lipid bilayer and the PEDOT:PSS channel where the hindrance caused by the SLB slightly affects the response time of the device ( $\tau$  increases of 25%).

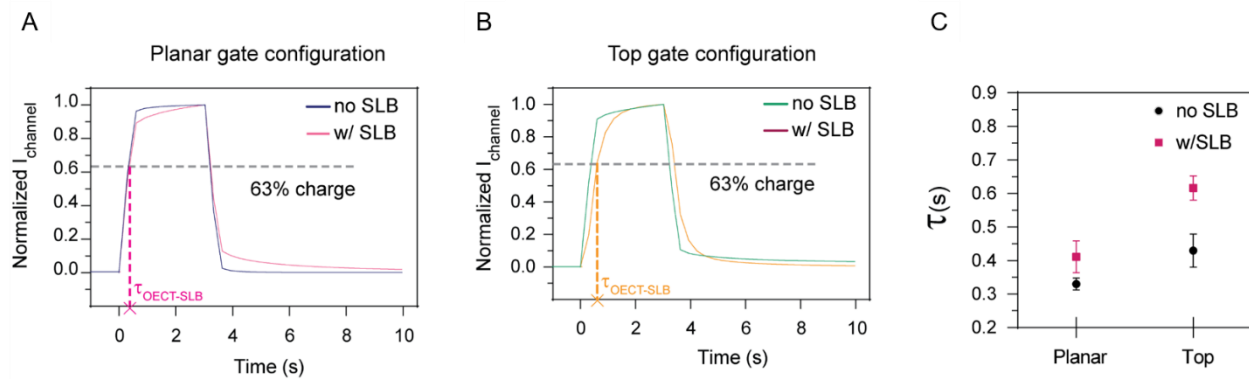


**Figure 3.21. Time response of the biomimetic synapse.** A) Channel current response elicited by the application of voltage pulses ( $\Delta t = 7$  s) at the planar gate electrode in the biomembrane-based OECT. Dashed horizontal lines represent the current threshold set to calculate the time response of the device. B) Channel current response elicited by the application of voltage pulses ( $\Delta t = 7$  s) at the top gate electrode in the biomembrane-based OECT. Dashed horizontal lines represent the current threshold set to calculate the time response of the device. C) Mean values of  $\tau_{\text{OECT-SLB}}$  calculated from 3 independent experiments for planar and top gate configurations with and without the lipid bilayer. Adapted from ref. [286].

Then, to investigate if the increased response time of the biomembrane-based OECT affects the neuromorphic functions of the device, a sequence of voltage pulses with  $\Delta t$  equal to multiple values of  $\tau_{\text{OECT-SLB}}$  (from 1 to 5  $\tau_{\text{OECT-SLB}}$ ) was applied at the gate electrode. Similarly to the unfunctionalized device (**Paragraph 3.2.2**), also in this case the highest conductance modulation is elicited by gate pulses with  $\Delta t = 1 \tau_{\text{OECT-SLB}}$ , with  $\Delta G = 490 \mu\text{S}$  for planar OECT (**Figure 3.22 A-i**) and  $\Delta G = 600 \mu\text{S}$  for the top gate configuration (**Figure 3.22 B-i**). Extending the time interval between pulses (up to  $\Delta t = 5 \tau_{\text{OECT-SLB}}$ ), instead, enables the cations discharge of the PEDOT:PSS channel and therefore the polymer partly recovers its initial conductivity, even if a slight memory effect is still visible in both configurations, with  $\Delta G = 371 \mu\text{S}$  in case of planar gate electrode (**Figure 3.22 A-v**) and  $\Delta G = 420 \mu\text{S}$  for the top gate OECT (**Figure 3.22 B-v**).

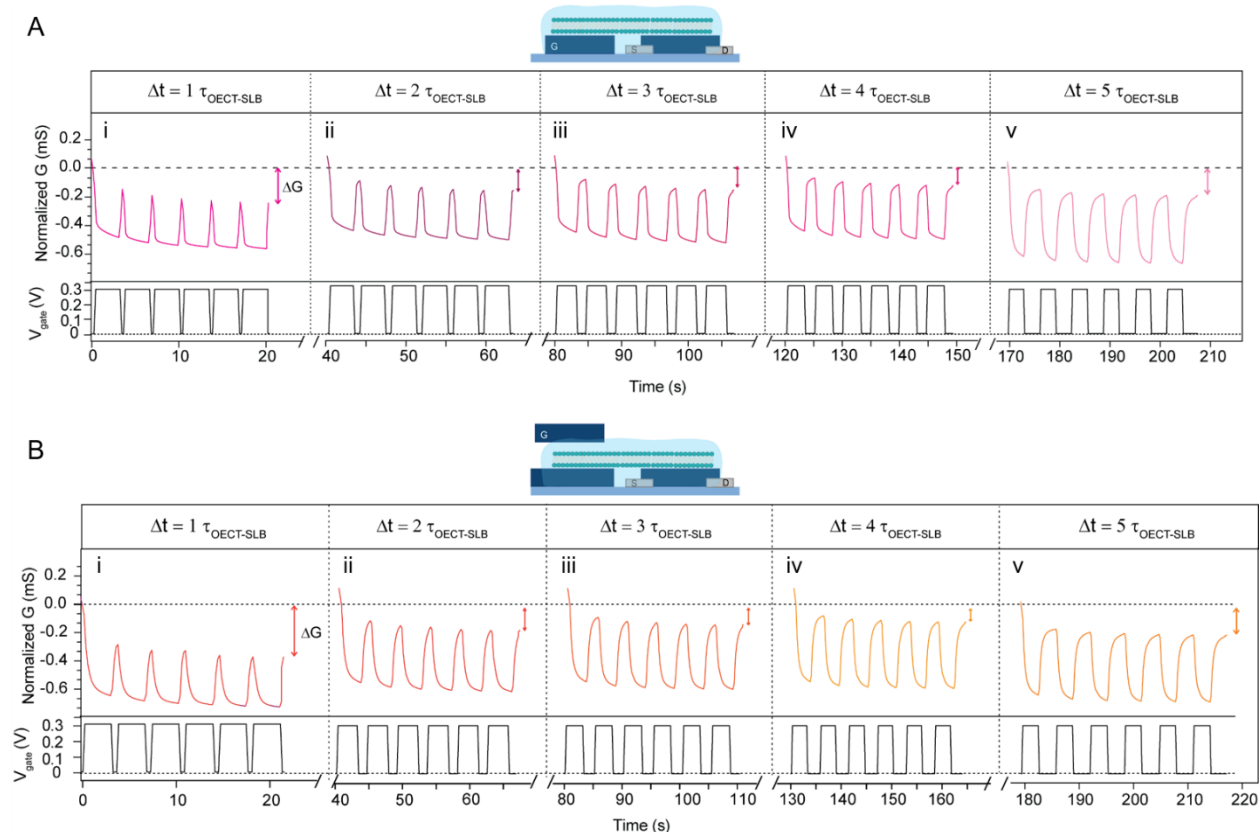


**Figure 3.22. Short-term potentiation of the biomimetic synapse in response to gate voltage pulses with  $\Delta t$  set as multiple values of  $\tau_{\text{OECT-SLB}}$ .** A) Conductance modulation elicited in the planar gate biomembrane-based OECT upon the application of gate voltage pulses with  $\Delta t$  set as multiple values of  $\tau_{\text{OECT-SLB}}$  ranging from 1 to 5  $\tau_{\text{OECT-SLB}}$ . B) Conductance modulation elicited in the top gate biomembrane-based OECT upon the application of gate voltage pulses with  $\Delta t$  set as multiple values of  $\tau_{\text{OECT-SLB}}$  ranging from 1 to 5  $\tau_{\text{OECT-SLB}}$ . Adapted from ref. [286].

Furthermore, the comparison of the mean conductance variation elicited by gate voltage pulses with  $\Delta t$  ranging from 1 to 5  $\tau$  for both gate configurations with and without SLB, highlights how in presence of the POPC-bilayer the biomimetic synapse exhibited amplified STP for both gate configurations and for all voltage pulses sequences (1  $\tau$ , 2  $\tau$ , 3  $\tau$ , 4  $\tau$  and 5  $\tau$ , **Figure 3.23 A**). This result further confirms that the presence of the SLB hinders the ionic discharge of the PEDOT:PSS channel, therefore enhancing neuromorphic behavior.

As mentioned in **Paragraph 3.2.2**, indeed, according to the RC model circuit,  $\Delta t = 1 \tau$  should elicit a discharge of the polymeric channel of 37%, therefore, at a given  $\Delta t$ , the unfunctionalized OECT and the biomimetic synapse should exhibit the same conductance modulation. However, the calculation based on the integration of the gate current highlights that the presence of the bilayer  $\Delta t = 1 \tau$  induces a lower ionic discharge. Here, the biomembrane enhances the number of charges trapped in the neuromorphic channel in

case of the top gate device (**Figure 3.23 B-C**), amplifying the STP. In fact, the doping/de-doping of OECTs coupled with lipid bilayers cannot be defined as the charge and discharge of a simple RC circuit, but a more sophisticated electrical modelling is required in order to describe the complex ionic processes of biomimetic neuromorphic devices.

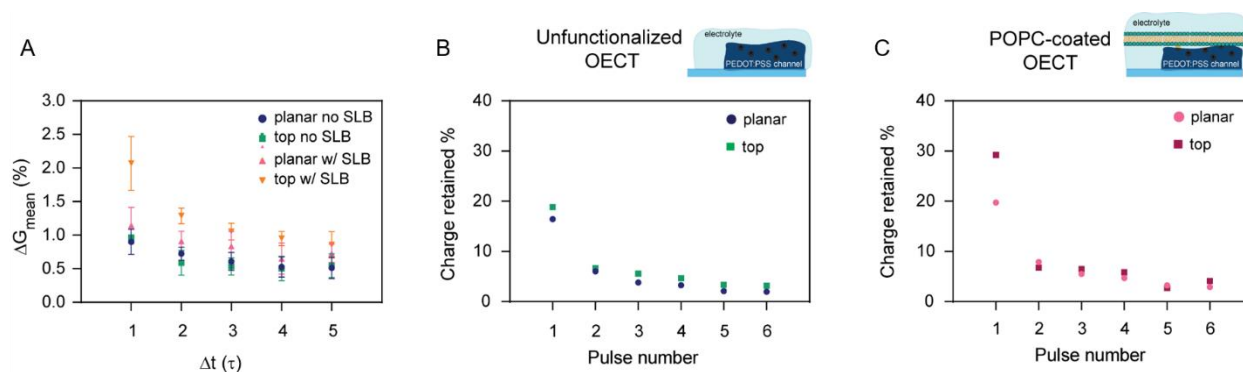


**Figure 3.23. Comparison of the short-term potentiation elicited in the unfunctionalized OECT and biomimetic synapse.** A) Mean conductance variation obtained from three independent experiments, elicited by gate voltage pulses with  $\Delta t$  ranging from 1 to 5  $\tau$  for both gate configurations with and without SLB. B) Percentage of charge retained in the neuromorphic channel per pulse in the unfunctionalized OECT. C) Percentage of charge retained in the neuromorphic channel per pulse in the biomimetic synapse (C). Adapted from ref. [286].

## 4 Conclusions

Neurodegenerative diseases affect millions of people worldwide and, although scientific research has made tremendous progress in the field, hindering the progression of the disease is still highly challenging. Lately, alterations in synaptic functioning and neuronal membrane composition have been revealed in the early stage of disease, suggesting they might be among the main causes of neurodegeneration. The complexity of the brain and the nervous system, however, prevents the characterization of mechanisms underlying cognitive impairment and inhibit the development of therapeutic treatments able to hamper neurodegeneration prior the appearance of the symptoms. The impossibility to investigate the degeneration of neuronal cells in their native environment, lead to a growing interest for *in vitro* biomimetic neuroelectronic platforms which, on one hand resemble simplified models of the nervous system thus facilitating experimental studies, and on the other hand exhibit all the fundamental features of the human brain so that all mechanisms involved in synaptic dysfunction might be thoroughly characterized. At this purpose in recent years more and more neuroelectronic platforms have been engineered with biomimetic features resembling neuronal architecture: from here, the development of artificial biomembranes able to recapitulate native cell membrane composition, and 3D electrodes presenting surface topographies recalling dendritic spines shape. Furthermore, the attempt to mimic also the biomechanical properties of neuronal tissues, placed conductive polymers as leading materials for neuroelectronic devices as they display low Young's modulus comparable to that of the human brain, as well as a peculiar conduction mechanism as they can transduce ionic currents into electrical signals similarly to biological synapses. Taking advantage of such ionic-electronic conduction and inspired by the learning abilities of the brain, in the last decade researchers exploited conductive polymers for developing OECTs which can act as neuromorphic devices, artificial platforms able to exhibit an adaptive behavior recalling synaptic plasticity. Here, in the first part of the project, a biohybrid platform was engineered by the direct coupling of a PEDOT:PSS-based organic neuromorphic device with PC-12 cells: the so-formed synapse presents an artificial post-synaptic terminal and a biological pre-synaptic end. Furthermore, exploiting the ability of cells to spontaneously secrete dopamine, a neurotransmitter-mediated plasticity was demonstrated. Here, the application of square voltage pulses at the gate electrode induces the electrochemical oxidation of dopamine, and protons and electrons produced from the reaction contribute to the conductance modulation of the neuromorphic channel. Of note, the artificial post-synaptic neurons is able to retain memory of dopamine-based stimulation exhibiting a short and a long-term plasticity with retention time extended up to 24 hours. The biohybrid interface was furtherly investigated by means of optical and electron microscopy which confirmed not only the presence of dopamine vesicles at the pre-synaptic site, but validated also the excellent biocompatibility of the artificial device, as cells viability did not show any alterations even after performing the electrochemical

measurements. Additionally, the neurotransmitter recycling was mimicked operating the device under microfluidic flow that, removing dopamine from the artificial synaptic cleft is able to restore the initial conductive state of the neuromorphic device. Finally, the Hebbian learning principle is emulated by means of chemical stimulation of the pre-synaptic terminal: here, dopamine releasing can be triggered exposing PC-12 cells to a KCl solution which elicit synaptic modulation even in a short time-scale. Once validated the neurotransmitter-mediated plasticity of the organic neuromorphic device, in the second part of the project the biomimetic features of the artificial synapse were improved, coupling the device with supported lipid bilayers. In particular, a homogeneous fluid phospholipid bilayer was assembled on the surface of the OECT to recapitulate cell membrane composition. Here, the outward architecture and uniformity of the SLB were characterized by means of FRAP and AFM, which validated the high lateral mobility of lipid molecules and the integrity of the double layer. Later, the influence of such synthetic membrane on the short-term plasticity of the neuromorphic device was investigated testing also two different configurations of the gate electrode, a planar and a top one. Of note, while in absence of the SLB the position of the gate electrode is irrelevant for the OECT functions, the presence of the biomembrane splits the two configurations, enhancing the top gate-modulated plasticity. As support of this result, the quantification of cations trapped into the neuromorphic channel revealed that the SLB behaves like a barrier hindering the discharge of the PEDOT:PSS channel and therefore enhancing the short-term conductance modulation: such ionic hindrance is amplified in case of the top gate configuration, *i.e.*, when ions moving from the gate to the channel and *vice versa* need to cross the double layer. Additionally, the biomembrane enhances the time response of the device in agreement with previous reported studies: however such variation is again enhanced in the top gate OECT. All these findings therefore suggest that the lipid double layer might modulate the ionic flow in a different way, depending whether ions need to cross the membrane or can freely move in the aqueous cushion placed at the device-SLB interface. Although the ionic pathways require further investigation, it is clear that biomembrane-based OECTs exhibit enhanced synaptic behavior, appearing as promising candidates for *in vitro* synapses resembling both the outward architecture and functionalities of biological neurons. The biomimetic device here implemented presents a very simplified model of cell membranes as the double layer was formed using a single phospholipid molecule. Further studies will be addressed on increasing the complexity of the artificial membrane assembling a SLB with sphingolipids and cholesterol and embedding neurotransmitter receptors within the double layer: with such biomimetic features the neuromorphic device could indeed resemble the physiological mechanism of chemical synapses as in presence of neurotransmitters binding to their receptors, ions could freely diffuse into the neuromorphic channel modulating the synaptic strength (*i.e.*, OECT conductance) of the artificial synapse. As future perspective, the introduction of neuromimetic topographical cues on the OECT surface would provide an artificial synapse whose architecture, geometry and functionalities recall the ones of

biological neurons. Here, the surface modifications of the device can lead to a spontaneous coupling of the cellular and electronic platform into a symbiotic unit, while also improving the neuromorphic functions of the OECT mimicking post-synaptic membrane composition. Furthermore, the neurotransmitter-mediated plasticity of neuromorphic devices open up a wealth of possibilities for the investigation of neurodegenerative disorders such as Parkinson's disease in which the dopaminergic pathways are disrupted, and more in general to untangle pathophysiological mechanisms involving synaptic plasticity loss.

## References

- [1] “Basic Structure and Function of the Nervous System | Anatomy and Physiology I,” can be found under <https://courses.lumenlearning.com/cuny-csi-ap-1/chapter/basic-structure-and-function-of-the-nervous-system/>, **n.d.**
- [2] S. Jäkel, L. Dimou, *Frontiers in Cellular Neuroscience* **2017**, *11*.
- [3] “Overview of neuron structure and function (article) | Khan Academy,” can be found under [https://www.khanacademy.org/\\_render](https://www.khanacademy.org/_render), **n.d.**
- [4] F. Naz, Y. H. Siddique, *The Open Biology Journal* **2020**, *8*, DOI 10.2174/1874196702008010006.
- [5] “Neurodegenerative Diseases,” can be found under <https://www.niehs.nih.gov/research/supported/health/neurodegenerative/index.cfm>, **n.d.**
- [6] M.-T. Heemels, *Nature* **2016**, *539*, 179.
- [7] R. Armstrong, *Folia Neuropathol* **2020**, *58*, 93.
- [8] P. Scheltens, K. Blennow, M. M. B. Breteler, B. de Strooper, G. B. Frisoni, S. Salloway, W. M. Van der Flier, *Lancet* **2016**, *388*, 505.
- [9] L. M. Bekris, C.-E. Yu, T. D. Bird, D. W. Tsuang, *J Geriatr Psychiatry Neurol* **2010**, *23*, 213.
- [10] M. Giri, M. Zhang, Y. Lü, *Clin Interv Aging* **2016**, *11*, 665.
- [11] B. De Strooper, *Cell* **2014**, *159*, 721.
- [12] W. Poewe, K. Seppi, C. M. Tanner, G. M. Halliday, P. Brundin, J. Volkmann, A.-E. Schrag, A. E. Lang, *Nat Rev Dis Primers* **2017**, *3*, 17013.
- [13] C. Rangel-Barajas, I. Coronel, B. Florán, *Aging Dis* **2015**, *6*, 349.
- [14] D. F. Lázaro, E. F. Rodrigues, R. Langohr, H. Shahpasandzadeh, T. Ribeiro, P. Guerreiro, E. Gerhardt, K. Kröhnert, J. Klucken, M. D. Pereira, B. Popova, N. Kruse, B. Mollenhauer, S. O. Rizzoli, G. H. Braus, K. M. Danzer, T. F. Outeiro, *PLoS Genet* **2014**, *10*, e1004741.
- [15] D. Salat, E. Tolosa, *J Parkinsons Dis* **2013**, *3*, 255.
- [16] C. O. Oluigbo, A. Salma, A. R. Rezai, *IEEE Rev Biomed Eng* **2012**, *5*, 88.
- [17] A. Compston, A. Coles, *Lancet* **2008**, *372*, 1502.
- [18] W.-J. Huang, W.-W. Chen, X. Zhang, *Exp Ther Med* **2017**, *13*, 3163.
- [19] E. M. Frohman, M. K. Racke, C. S. Raine, *New England Journal of Medicine* **2006**, *354*, 942.
- [20] B. Hemmer, M. Kerschensteiner, T. Korn, *Lancet Neurol* **2015**, *14*, 406.
- [21] C. H. Polman, B. M. J. Uitdehaag, *West J Med* **2000**, *173*, 398.
- [22] P. Imbriani, T. Schirinzi, M. Meringolo, N. B. Mercuri, A. Pisani, *Front Neurol* **2018**, *9*, 103.
- [23] K. Dietrich, Y. Bouter, M. Müller, T. A. Bayer, *Molecules* **2018**, *23*, E718.
- [24] R. Marin, *Front Physiol* **2013**, *4*, 188.
- [25] T. M. Wishart, S. H. Parson, T. H. Gillingswater, *J Neuropathol Exp Neurol* **2006**, *65*, 733.

- [26] R. W. Holz, S. K. Fisher, *Basic Neurochemistry: Molecular, Cellular and Medical Aspects. 6th edition* **1999**.
- [27] N. Rouach, E. Avignone, W. Mème, A. Koulakoff, L. Venance, F. Blomstrand, C. Giaume, *Biol Cell* **2002**, *94*, 457.
- [28] D. Purves, G. J. Augustine, D. Fitzpatrick, L. C. Katz, A.-S. LaMantia, J. O. McNamara, S. M. Williams, *Neuroscience. 2nd edition* **2001**.
- [29] M. J. Fogarty, R. Kanjhan, M. C. Bellingham, P. G. Noakes, *J. Neurosci.* **2016**, *36*, 80.
- [30] W. A. Catterall, A. P. Few, *Neuron* **2008**, *59*, 882.
- [31] F. Ackermann, C. L. Waites, C. C. Garner, *EMBO Rep* **2015**, *16*, 923.
- [32] M. G. Stewart, V. I. Popov, I. V. Kraev, N. Medvedev, H. A. Davies, in *The Synapse* (Eds.: V. Pickel, M. Segal), Academic Press, Boston, **2014**, pp. 1–20.
- [33] M. U. Ghani, F. Mesadi, S. D. Kanık, A. Ö. Argunşah, A. F. Hobbiss, I. Israely, D. Ünay, T. Taşdizen, M. Çetin, *J Neurosci Methods* **2017**, *279*, 13.
- [34] W. C. Risher, T. Ustunkaya, J. S. Alvarado, C. Eroglu, *PLOS ONE* **2014**, *9*, e107591.
- [35] Y. Hayashi, A. K. Majewska, *Neuron* **2005**, *46*, 529.
- [36] J. Bourne, K. M. Harris, *Curr Opin Neurobiol* **2007**, *17*, 381.
- [37] H. Hering, M. Sheng, *Nat Rev Neurosci* **2001**, *2*, 880.
- [38] J. C. Fiala, M. Feinberg, V. Popov, K. M. Harris, *J Neurosci* **1998**, *18*, 8900.
- [39] Y. Yoshihara, M. De Roo, D. Muller, *Curr Opin Neurobiol* **2009**, *19*, 146.
- [40] N. E. Ziv, S. J. Smith, *Neuron* **1996**, *17*, 91.
- [41] A. J. G. D. Holtmaat, J. T. Trachtenberg, L. Wilbrecht, G. M. Shepherd, X. Zhang, G. W. Knott, K. Svoboda, *Neuron* **2005**, *45*, 279.
- [42] J. Grutzendler, N. Kasthuri, W.-B. Gan, *Nature* **2002**, *420*, 812.
- [43] T. Xu, X. Yu, A. J. Perlik, W. F. Tobin, J. A. Zweig, K. Tennant, T. Jones, Y. Zuo, *Nature* **2009**, *462*, 915.
- [44] M. Joëls, H. Karst, R. A. Sarabdjitsingh, *Acta Physiol (Oxf)* **2018**, *223*, e13066.
- [45] J. J. Kim, M. W. Jung, *Neurosci Biobehav Rev* **2006**, *30*, 188.
- [46] J. Herms, M. M. Dorostkar, *Annu Rev Pathol* **2016**, *11*, 221.
- [47] B. D. Boros, K. M. Greathouse, E. G. Gentry, K. A. Curtis, E. L. Birchall, M. Gearing, J. H. Herskowitz, *Ann Neurol* **2017**, *82*, 602.
- [48] L. K. Parajuli, K. Wako, S. Maruo, S. Kakuta, T. Taguchi, M. Ikuno, H. Yamakado, R. Takahashi, M. Koike, *eNeuro* **2020**, *7*, ENEURO.0072.
- [49] A. Rmz, *Molecular Neuropharmacology*, **n.d.**
- [50] S. E. Hyman, *Curr Biol* **2005**, *15*, R154.

- [51] C. Henley, **2021**.
- [52] Z. Lackovic, *EJIFCC* **2004**, *15*, 61.
- [53] D. Purves, G. J. Augustine, D. Fitzpatrick, L. C. Katz, A.-S. LaMantia, J. O. McNamara, S. M. Williams, *Neuroscience. 2nd edition* **2001**.
- [54] R. C. Malenka, *Nat Rev Neurosci* **2003**, *4*, 923.
- [55] A. Citri, R. C. Malenka, *Neuropsychopharmacol* **2008**, *33*, 18.
- [56] H. Shouval, S. Wang, G. Wittenberg, *Frontiers in Computational Neuroscience* **2010**, *4*.
- [57] Y. Yang, N. Calakos, *Frontiers in Synaptic Neuroscience* **2013**, *5*.
- [58] T. W. Rosahl, M. Geppert, D. Spillane, J. Herz, R. E. Hammer, R. C. Malenka, T. C. Südhof, *Cell* **1993**, *75*, 661.
- [59] R. S. Zucker, W. G. Regehr, *Annu Rev Physiol* **2002**, *64*, 355.
- [60] P.-Y. Deng, V. A. Klyachko, *Commun Integr Biol* **2011**, *4*, 543.
- [61] F. S. D. Pj, A. Lf, *Neuron* **2005**, *45*, DOI 10.1016/j.neuron.2005.02.001.
- [62] W. C. Abraham, O. D. Jones, D. L. Glanzman, *npj Sci. Learn.* **2019**, *4*, 1.
- [63] D. A. Fortin, T. Srivastava, T. R. Soderling, *Neuroscientist* **2012**, *18*, 326.
- [64] S. Hasegawa, S. Sakuragi, K. Tominaga-Yoshino, A. Ogura, *Sci Rep* **2015**, *5*, 7707.
- [65] G. Martella, P. Bonsi, S. W. Johnson, A. Quartarone, *Neural Plasticity* **2018**, *2018*, e9230704.
- [66] G.-M. Wu, C.-P. Du, Y. Xu, *International Journal of Neuroscience* **2021**, *0*, 1.
- [67] C. Lazzari, M. J. Kipanyula, M. Agostini, T. Pozzan, C. Fasolato, *Neurobiol Aging* **2015**, *36*, 877.
- [68] G. Valincius, F. Heinrich, R. Budvytyte, D. J. Vanderah, D. J. McGillivray, Y. Sokolov, J. E. Hall, M. Lösche, *Biophys J* **2008**, *95*, 4845.
- [69] A. C. Paula-Lima, J. Brito-Moreira, S. T. Ferreira, *J Neurochem* **2013**, *126*, 191.
- [70] D. J. Selkoe, *Science* **2002**, *298*, 789.
- [71] B. Picconi, G. Piccoli, P. Calabresi, *Adv Exp Med Biol* **2012**, *970*, 553.
- [72] T.-F. Yuan, W.-G. Li, C. Zhang, H. Wei, S. Sun, N.-J. Xu, J. Liu, T.-L. Xu, *Translational Neurodegeneration* **2020**, *9*, 44.
- [73] K. A. Jansen, P. Atherton, C. Ballestrem, *Semin Cell Dev Biol* **2017**, *71*, 75.
- [74] M. S. Bretscher, *Science* **1973**, *181*, 622.
- [75] J. A. F. Op den Kamp, *Annual Review of Biochemistry* **1979**, *48*, 47.
- [76] D. Puchkov, V. Haucke, *Trends Cell Biol* **2013**, *23*, 493.
- [77] J. Marszalek, H. Lodish, *Annual review of cell and developmental biology* **2005**, DOI 10.1146/ANNUREV.CELLBIO.21.122303.120624.
- [78] B. Davletov, C. Montecucco, *Curr Opin Neurobiol* **2010**, *20*, 543.

- [79] I. Milosevic, J. B. Sørensen, T. Lang, M. Krauss, G. Nagy, V. Haucke, R. Jahn, E. Neher, *J Neurosci* **2005**, *25*, 2557.
- [80] G. Di Paolo, P. De Camilli, *Nature* **2006**, *443*, 651.
- [81] A. Grossfield, S. E. Feller, M. C. Pitman, *PNAS* **2006**, *103*, 4888.
- [82] J. A. Allen, R. A. Halverson-Tamboli, M. M. Rasenick, *Nat Rev Neurosci* **2007**, *8*, 128.
- [83] Y. Barenholz, *Subcell Biochem* **2004**, *37*, 167.
- [84] S. M, K. E, *Cold Spring Harbor perspectives in biology* **2011**, *3*, DOI 10.1101/cshperspect.a005678.
- [85] M. G. Martín, F. Pfrieger, C. G. Dotti, *EMBO Rep* **2014**, *15*, 1036.
- [86] C. Pacheco, L. G. Aguayo, C. Opazo, *Front Physiol* **2012**, *3*, 297.
- [87] P. J. Barrett, Y. Song, W. D. Van Horn, E. J. Hustedt, J. M. Schafer, A. Hadziselimovic, A. J. Beel, C. R. Sanders, *Science* **2012**, *336*, 1168.
- [88] G. Di Paolo, T.-W. Kim, *Nat Rev Neurosci* **2011**, *12*, 284.
- [89] A. Slanzi, G. Iannoto, B. Rossi, E. Zenaro, G. Constantin, *Frontiers in Cell and Developmental Biology* **2020**, *8*.
- [90] M. Gulino, D. Kim, S. Pané, S. D. Santos, A. P. Pêgo, *Frontiers in Neuroscience* **2019**, *13*.
- [91] W. Liu, Z. Yang, in *2010 Proceedings of ESSCIRC*, **2010**, pp. 17–26.
- [92] R. Yang, C. H. Tam, K. L. Cheung, K. C. Wong, N. Xi, J. Yang, K. W. C. Lai, *Robotics and Biomimetics* **2014**, *1*, 20.
- [93] M. P. Maher, J. Pine, J. Wright, Y. C. Tai, *J Neurosci Methods* **1999**, *87*, 45.
- [94] B. Sakmann, E. Neher, *Annu Rev Physiol* **1984**, *46*, 455.
- [95] A. Prominski, B. Tian, *Current Opinion in Biotechnology* **2021**, *72*, 69.
- [96] P. Rinklin, B. Wolfrum, *Neuroforum* **2021**, *27*, 213.
- [97] C. Lubrano, G. M. Matrone, C. Forro, Z. Jahed, A. Offenhaeusser, A. Salleo, B. Cui, F. Santoro, *MRS Communications* **2020**, *10*, 398.
- [98] Y. Jiang, B. Tian, *Nat Rev Mater* **2018**, *3*, 473.
- [99] J. Rivnay, R. M. Owens, G. G. Malliaras, *Chem. Mater.* **2014**, *26*, 679.
- [100] M. Bianchi, A. De Salvo, M. Asplund, S. Carli, M. D. Lauro, A. Schulze-Bonhage, T. Stieglitz, L. Fadiga, F. Biscarini, **2021**, DOI 10.36227/techrxiv.16938844.v1.
- [101] S. G. Higgins, A. Lo Fiego, I. Patrick, A. Creamer, M. M. Stevens, *Advanced Materials Technologies* **2020**, *5*, 2000384.
- [102] C. Pitsalidis, A.-M. Pappa, A. J. Boys, Y. Fu, C.-M. Moysidou, D. van Niekerk, J. Saez, A. Savva, D. Iandolo, R. M. Owens, *Chem. Rev.* **2021**, DOI 10.1021/acs.chemrev.1c00539.

- [103] S. Zips, L. Grob, P. Rinklin, K. Terkan, N. Y. Adly, L. J. K. Weiß, D. Mayer, B. Wolfrum, *ACS Appl. Mater. Interfaces* **2019**, *11*, 32778.
- [104] P. D. Jones, A. Moskalyuk, C. Barthold, K. Gutöhrlein, G. Heusel, B. Schröppel, R. Samba, M. Giugliano, *Frontiers in Neuroscience* **2020**, *14*.
- [105] L. Ferlauto, M. J. I. Airaghi Leccardi, N. A. L. Chenais, S. C. A. Gilliéron, P. Vagni, M. Bevilacqua, T. J. Wolfensberger, K. Sivula, D. Ghezzi, *Nat Commun* **2018**, *9*, 992.
- [106] C. M. Frost, D. C. Ursu, S. M. Flattery, A. Nedic, C. A. Hassett, J. D. Moon, P. J. Buchanan, R. Brent Gillespie, T. A. Kung, S. W. P. Kemp, P. S. Cederna, M. G. Urbanek, *J Neuroeng Rehabil* **2018**, *15*, 108.
- [107] D. Khodagholy, T. Doublet, P. Quilichini, M. Gurfinkel, P. Leleux, A. Ghestem, E. Ismailova, T. Hervé, S. Sanaur, C. Bernard, G. G. Malliaras, *Nat Commun* **2013**, *4*, 1575.
- [108] M. ElMahmoudy, S. Inal, A. Charrier, I. Uguz, G. G. Malliaras, S. Sanaur, *Macromolecular Materials and Engineering* **2017**, *302*, 1600497.
- [109] L. Ghasemi-Mobarakeh, M. P. Prabhakaran, M. Morshed, M. H. Nasr-Esfahani, H. Baharvand, S. Kiani, S. S. Al-Deyab, S. Ramakrishna, *J Tissue Eng Regen Med* **2011**, *5*, e17.
- [110] R. Ravichandran, S. Sundarajan, J. R. Venugopal, S. Mukherjee, S. Ramakrishna, *J R Soc Interface* **2010**, *7 Suppl 5*, S559.
- [111] B. D. Paulsen, K. Tybrandt, E. Stavrinidou, J. Rivnay, *Nat. Mater.* **2020**, *19*, 13.
- [112] D. A. Bernards, G. G. Malliaras, *Advanced Functional Materials* **2007**, *17*, 3538.
- [113] C. Yao, Q. Li, J. Guo, F. Yan, I.-M. Hsing, *Advanced Healthcare Materials* **2015**, *4*, 528.
- [114] D. Khodagholy, J. N. Gelinas, Z. Zhao, M. Yeh, M. Long, J. D. Greenlee, W. Doyle, O. Devinsky, G. Buzsáki, *Science Advances* **2016**, DOI 10.1126/sciadv.1601027.
- [115] Y. Liang, F. Brings, V. Maybeck, S. Ingebrandt, B. Wolfrum, A. Pich, A. Offenhäusser, D. Mayer, *Advanced Functional Materials* **2019**, *29*, 1902085.
- [116] K. Xie, N. Wang, X. Lin, Z. Wang, X. Zhao, P. Fang, H. Yue, J. Kim, J. Luo, S. Cui, F. Yan, P. Shi, *eLife n.d.*, *9*, e50345.
- [117] A. J. Hackett, J. Malmström, J. Travas-Sejdic, *Progress in Polymer Science* **2017**, *70*, 18.
- [118] E. Šafaříková, L. Švihálková Šindlerová, S. Štríteský, L. Kubala, M. Vala, M. Weiter, J. Vítěček, *Sensors and Actuators B: Chemical* **2018**, *260*, 418.
- [119] N. Bhagwat, R. E. Murray, S. I. Shah, K. L. Kiick, D. C. Martin, *Acta Biomater* **2016**, *41*, 235.
- [120] X. Cui, D. C. Martin, *Sensors and Actuators B: Chemical* **2003**, *89*, 92.
- [121] X. Cui, V. A. Lee, Y. Raphael, J. A. Wiler, J. F. Hetke, D. J. Anderson, D. C. Martin, *J Biomed Mater Res* **2001**, *56*, 261.

- [122] M. N. Gueye, A. Carella, J. Faure-Vincent, R. Demadrille, J.-P. Simonato, *Progress in Materials Science* **2020**, *108*, 100616.
- [123] K. J. Gilmore, M. Kita, Y. Han, A. Gelmi, M. J. Higgins, S. E. Moulton, G. M. Clark, R. Kapsa, G. G. Wallace, *Biomaterials* **2009**, *30*, 5292.
- [124] M. Baudry, *Proceedings of the IEEE* **n.d.**
- [125] T. W. Berger, R. E. Hampson, D. Song, A. Goonawardena, V. Z. Marmarelis, S. A. Deadwyler, *J Neural Eng* **2011**, *8*, 046017.
- [126] S. A. Deadwyler, R. E. Hampson, D. Song, I. Opris, G. A. Gerhardt, V. Z. Marmarelis, T. W. Berger, *Exp Neurol* **2017**, *287*, 452.
- [127] A. Mariano, C. Lubrano, U. Bruno, C. Ausilio, N. B. Dinger, F. Santoro, *Chem. Rev.* **2021**, DOI 10.1021/acs.chemrev.1c00363.
- [128] D. L. Sparks, M. N. Sabbagh, D. J. Connor, J. Lopez, L. J. Launer, P. Browne, D. Wasser, S. Johnson-Traver, J. Lochhead, C. Ziolkowski, *Arch Neurol* **2005**, *62*, 753.
- [129] G. Li, E. B. Larson, J. A. Sonnen, J. B. Shofer, E. C. Petrie, A. Schantz, E. R. Peskind, M. A. Raskind, J. C. S. Breitner, T. J. Montine, *Neurology* **2007**, *69*, 878.
- [130] J. Sarkis, V. Vié, *Front Bioeng Biotechnol* **2020**, *8*, 270.
- [131] R. P. Richter, R. Bérat, A. R. Brisson, *Langmuir* **2006**, *22*, 3497.
- [132] C. A. Keller, B. Kasemo, *Biophys J* **1998**, *75*, 1397.
- [133] E. Reimhult, F. Höök, B. Kasemo, *Phys. Rev. E* **2002**, *66*, 051905.
- [134] E. Reimhult, F. Höök, B. Kasemo, *Langmuir* **2003**, *19*, 1681.
- [135] K. Simons, J. L. Sampaio, *Cold Spring Harb Perspect Biol* **2011**, *3*, a004697.
- [136] J. C. Lawrence, D. E. Saslowsky, J. M. Edwardson, R. M. Henderson, *Biophys J* **2003**, *84*, 1827.
- [137] “Handbook of Lipid Bilayers,” can be found under <https://www.routledge.com/Handbook-of-Lipid-Bilayers/Marsh/p/book/9781420088328>, **n.d.**
- [138] P. S. Cremer, S. G. Boxer, *Journal of Physical Chemistry B* **1999**, *103*, 2554.
- [139] N. F. Hussain, A. P. Siegel, Y. Ge, R. Jordan, C. A. Naumann, *Biophys J* **2013**, *104*, 2212.
- [140] S. M. Schiller, R. Naumann, K. Lovejoy, H. Kunz, W. Knoll, *Angew Chem Int Ed Engl* **2003**, *42*, 208.
- [141] I. P. McCabe, M. B. Forstner, *Open Journal of Biophysics* **2013**, *3*, 59.
- [142] A. R. Ferhan, B. K. Yoon, S. Park, T. N. Sut, H. Chin, J. H. Park, J. A. Jackman, N.-J. Cho, *Nat Protoc* **2019**, *14*, 2091.
- [143] S. R. Tabaei, J. A. Jackman, M. Kim, S. Yorulmaz, S. Vafaei, N.-J. Cho, *J Vis Exp* **2015**, 53073.
- [144] S. R. Tabaei, J. A. Jackman, S.-O. Kim, V. P. Zhdanov, N.-J. Cho, *Langmuir* **2015**, *31*, 3125.
- [145] S. R. Tabaei, W. B. Ng, S.-J. Cho, N.-J. Cho, *ACS Appl Mater Interfaces* **2016**, *8*, 11875.

- [146] S. R. Tabaei, J.-H. Choi, G. Haw Zan, V. P. Zhdanov, N.-J. Cho, *Langmuir* **2014**, *30*, 10363.
- [147] S. R. Tabaei, J. A. Jackman, S.-O. Kim, B. Liedberg, W. Knoll, A. N. Parikh, N.-J. Cho, *Langmuir* **2014**, *30*, 13345.
- [148] L. M. Kawakami, B. K. Yoon, J. A. Jackman, W. Knoll, P. S. Weiss, N.-J. Cho, *Langmuir* **2017**, *33*, 14756.
- [149] Y. Zhang, S. Wustoni, A. Savva, A. Giovannitti, I. McCulloch, S. Inal, *J. Mater. Chem. C* **2018**, *6*, 5218.
- [150] Y. Kurihara, T. Sawazumi, T. Takeuchi, *Analyst* **2014**, *139*, 6016.
- [151] K. Zobel, S. E. Choi, R. Minakova, M. Gocyla, A. Offenhäusser, *Soft Matter* **2017**, *13*, 8096.
- [152] R. Ghosh Moulick, G. Panaitov, L. Du, D. Mayer, A. Offenhäusser, *Nanoscale* **2018**, *10*, 5295.
- [153] M. J. Richards, C.-Y. Hsia, R. R. Singh, H. Haider, J. Kumpf, T. Kawate, S. Daniel, *Langmuir* **2016**, *32*, 2963.
- [154] G. T. Charras, M. Coughlin, T. J. Mitchison, L. Mahadevan, *Biophysical Journal* **2008**, *94*, 1836.
- [155] A. Svetlova, J. Ellieroth, F. Milos, V. Maybeck, A. Offenhäusser, *Langmuir* **2019**, *35*, 8076.
- [156] Y. Zhang, S. Inal, C.-Y. Hsia, M. Ferro, M. Ferro, S. Daniel, R. M. Owens, *Advanced Functional Materials* **2016**, *26*, 7304.
- [157] H. Su, H.-Y. Liu, A.-M. Pappa, T. C. Hidalgo, P. Cavassin, S. Inal, R. M. Owens, S. Daniel, *ACS Appl. Mater. Interfaces* **2019**, *11*, 43799.
- [158] H.-Y. Liu, A.-M. Pappa, T. C. Hidalgo, S. Inal, R. M. Owens, S. Daniel, *Anal Bioanal Chem* **2020**, *412*, 6265.
- [159] S. T. Ferreira, M. V. Lourenco, M. M. Oliveira, F. G. De Felice, *Front Cell Neurosci* **2015**, *9*, 191.
- [160] H.-Y. Liu, A.-M. Pappa, A. Pavia, C. Pitsalidis, Q. Thiburce, A. Salleo, R. M. Owens, S. Daniel, *Langmuir* **2020**, *36*, 7325.
- [161] A.-M. Pappa, H.-Y. Liu, W. Traberg-Christensen, Q. Thiburce, A. Savva, A. Pavia, A. Salleo, S. Daniel, R. M. Owens, *ACS Nano* **2020**, *14*, 12538.
- [162] A. Hai, D. Kamber, G. Malkinson, H. Erez, N. Mazurski, J. Shappir, M. E. Spira, *J. Neural Eng.* **2009**, *6*, 066009.
- [163] P. Wijdenes, H. Ali, R. Armstrong, W. Zaidi, C. Dalton, N. I. Syed, *Sci Rep* **2016**, *6*, 34553.
- [164] T. J. J. Hondrich, B. Lenyk, P. Shokoohimehr, D. Kireev, V. Maybeck, D. Mayer, A. Offenhäusser, *ACS Appl. Mater. Interfaces* **2019**, *11*, 46451.
- [165] S. Aslanoglou, Y. Chen, V. Oorschot, Z. Trifunovic, E. Hanssen, K. Suu, N. H. Voelcker, R. Elnathan, *J. Am. Chem. Soc.* **2020**, *142*, 15649.
- [166] R. Huys, D. Braeken, D. Jans, A. Stassen, N. Collaert, J. Wouters, J. Loo, S. Severi, F. Vleugels, G. Callewaert, K. Verstreken, C. Bartic, W. Eberle, *Lab Chip* **2012**, *12*, 1274.

- [167] B. van Meerbergen, T. Raemaekers, K. Winters, D. Braeken, C. Bartic, M. Spira, Y. Engelborghs, W. G. Annaert, G. Borghs, *Journal of Experimental Nanoscience* **2007**, 2, 101.
- [168] H. Teixeira, C. Dias, P. Aguiar, J. Ventura, *Advanced Materials Technologies* **2021**, 6, 2000770.
- [169] M. E. Spira, N. Shmoel, S.-H. M. Huang, H. Erez, *Frontiers in Neuroscience* **2018**, 12.
- [170] F. Milos, A. Belu, D. Mayer, V. Maybeck, A. Offenhäusser, *Advanced Biology* **2021**, 5, 2000248.
- [171] M. E. Spira, A. Hai, *Nature Nanotech* **2013**, 8, 83.
- [172] A. Hai, J. Shappir, M. E. Spira, *J Neurophysiol* **2010**, 104, 559.
- [173] A. Hai, J. Shappir, M. E. Spira, *Nat Methods* **2010**, 7, 200.
- [174] B. X. E. Desbailles, E. de Coulon, A. Bertsch, S. Rohr, P. Renaud, *Nano Lett.* **2019**, 19, 6173.
- [175] B. Van Meerbergen, J. Loo, R. Huys, T. Raemaekers, K. Winters, D. Braeken, Y. Engelborghs, W. Annaert, G. Borghs, C. Bartic, *Journal of Experimental Nanoscience* **2008**, 3, 147.
- [176] M. E. Spira, D. Kamber, A. Dormann, A. Cohen, C. Bartic, G. Borghs, K. Shabthai, J. P. M. L. Langedijk, S. Yitzchaik, J. Shappir, *MRS Online Proceedings Library (OPL)* **2007**, 1004, DOI 10.1557/PROC-1004-P02-05.
- [177] M. Marcus, K. Baranes, M. Park, I. S. Choi, K. Kang, O. Shefi, *Advanced Healthcare Materials* **2017**, 6, 1700267.
- [178] S. Patel, K. Kurpinski, R. Quigley, H. Gao, B. S. Hsiao, M.-M. Poo, S. Li, *Nano Lett* **2007**, 7, 2122.
- [179] H. B. Wang, M. E. Mullins, J. M. Cregg, C. W. McCarthy, R. J. Gilbert, *Acta Biomater* **2010**, 6, 2970.
- [180] H. Hwang, G. Kang, J. H. Yeon, Y. Nam, J.-K. Park, *Lab Chip* **2009**, 9, 167.
- [181] J. S. Chua, C.-P. Chng, A. A. K. Moe, J. Y. Tann, E. L. K. Goh, K.-H. Chiam, E. K. F. Yim, *Biomaterials* **2014**, 35, 7750.
- [182] M. Park, E. Oh, J. Seo, M.-H. Kim, H. Cho, J. Y. Choi, H. Lee, I. S. Choi, *Small* **2016**, 12, 1148.
- [183] P. N. Sergi, I. Morana Roccasalvo, I. Tonazzini, M. Cecchini, S. Micera, *PLoS One* **2013**, 8, e70304.
- [184] I. M. Roccasalvo, P. N. Sergi, I. Tonazzini, M. Cecchini, S. Micera, *Annu Int Conf IEEE Eng Med Biol Soc* **2015**, 2015, 7147.
- [185] L. Yao, S. Wang, W. Cui, R. Sherlock, C. O'Connell, G. Damodaran, A. Gorman, A. Windebank, A. Pandit, *Acta Biomaterialia* **2009**, 5, 580.
- [186] F. Johansson, P. Carlberg, N. Danielsen, L. Montelius, M. Kanje, *Biomaterials* **2006**, 27, 1251.
- [187] L. Micholt, A. Gärtner, D. Prodanov, D. Braeken, C. G. Dotti, C. Bartic, *PLOS ONE* **2013**, 8, e66170.
- [188] C. Xie, L. Hanson, W. Xie, Z. Lin, B. Cui, Y. Cui, *Nano Lett* **2010**, 10, 4020.

- [189] G. Gopalakrishnan, P. T. Yam, C. Madwar, M. Bostina, I. Rouiller, D. R. Colman, R. B. Lennox, *ACS Chem. Neurosci.* **2011**, *2*, 700.
- [190] H. N. Kim, D.-H. Kang, M. S. Kim, A. Jiao, D.-H. Kim, K.-Y. Suh, *Ann Biomed Eng* **2012**, *40*, 1339.
- [191] J. J. S. Rickard, I. Farrer, P. Goldberg Oppenheimer, *ACS Nano* **2016**, *10*, 3865.
- [192] Z. P. A. N, A. M, W. De, T.-S. J, *ACS applied materials & interfaces* **2018**, *10*, DOI 10.1021/acsami.8b02289.
- [193] C. Huang, B. Dong, N. Lu, B. Yang, L. Gao, L. Tian, D. Qi, Q. Wu, L. Chi, *Small* **2009**, *5*, 583.
- [194] F. Santoro, Y. van de Burgt, S. T. Keene, B. Cui, A. Salleo, *ACS Appl. Mater. Interfaces* **2017**, *9*, 39116.
- [195] C. Luo, R. Poddar, X. Liu, **2006**, DOI 10.1116/1.2186341.
- [196] S. M. Richardson-Burns, J. L. Hendricks, B. Foster, L. K. Povlich, D.-H. Kim, D. C. Martin, *Biomaterials* **2007**, *28*, 1539.
- [197] J. H. Lee, Y. S. Rim, W. K. Min, K. Park, H. T. Kim, G. Hwang, J. Song, H. J. Kim, *Advanced Functional Materials* **2021**, *31*, 2107074.
- [198] D. Ielmini, S. Ambrogio, *Nanotechnology* **2019**, *31*, 092001.
- [199] Y. Van De Burgt, A. Melianas, S. T. Keene, G. Malliaras, A. Salleo, *Nature Electronics* **2018**, *1*, 386.
- [200] D. S. Jeong, K. M. Kim, S. Kim, B. J. Choi, C. S. Hwang, *Advanced Electronic Materials* **2016**, *2*, 1600090.
- [201] T.-S. Kim, Y. Lee, W. Xu, Y. H. Kim, M. Kim, S.-Y. Min, T. H. Kim, H. W. Jang, T.-W. Lee, *Nano Energy* **2019**, *58*, 437.
- [202] L. Q. Zhu, C. J. Wan, L. Q. Guo, Y. Shi, Q. Wan, *Nat Commun* **2014**, *5*, 3158.
- [203] W. Xu, S.-Y. Min, H. Hwang, T.-W. Lee, *Sci Adv* **2016**, *2*, e1501326.
- [204] S. Battistoni, *BioNanoSci.* **2021**, *11*, 227.
- [205] H. Huang, C. Ge, Z. Liu, H. Zhong, E. Guo, M. He, C. Wang, G. Yang, K. Jin, *J. Semicond.* **2021**, *42*, 013103.
- [206] M.-K. Kim, Y. Park, I.-J. Kim, J.-S. Lee, *iScience* **2020**, *23*, 101846.
- [207] W. Lu, K.-H. Kim, T. Chang, S. Gaba, in *16th Asia and South Pacific Design Automation Conference (ASP-DAC 2011)*, **2011**, pp. 217–223.
- [208] W. Sun, B. Gao, M. Chi, Q. Xia, J. J. Yang, H. Qian, H. Wu, *Nat Commun* **2019**, *10*, 3453.
- [209] S. Gao, X. Yi, J. Shang, G. Liu, R.-W. Li, *Chem. Soc. Rev.* **2019**, *48*, 1531.
- [210] Y.-L. Liu, K.-L. Wang, G.-S. Huang, C.-X. Zhu, E.-S. Tok, K.-G. Neoh, E.-T. Kang, *Chem. Mater.* **2009**, *21*, 3391.

- [211] B. Koo, H. Baek, J. Cho, *Chem. Mater.* **2012**, *24*, 1091.
- [212] B. Hu, X. Zhu, X. Chen, L. Pan, S. Peng, Y. Wu, J. Shang, G. Liu, Q. Yan, R.-W. Li, *J. Am. Chem. Soc.* **2012**, *134*, 17408.
- [213] L. Yuan, S. Liu, W. Chen, F. Fan, G. Liu, *Advanced Electronic Materials* **2021**, *7*, 2100432.
- [214] V. C. Nguyen, P. S. Lee, *Sci Rep* **2016**, *6*, 19594.
- [215] Y. Liang, A. Offenhäusser, S. Ingebrandt, D. Mayer, *Adv Healthc Mater* **2021**, *10*, e2100061.
- [216] U. S. Bhansali, M. A. Khan, D. Cha, M. N. AlMadhoun, R. Li, L. Chen, A. Amassian, I. N. Odeh, H. N. Alshareef, *ACS Nano* **2013**, *7*, 10518.
- [217] Y. van de Burgt, E. Lubberman, E. J. Fuller, S. T. Keene, G. C. Faria, S. Agarwal, M. J. Marinella, A. Alec Talin, A. Salleo, *Nature Mater* **2017**, *16*, 414.
- [218] Y. van de Burgt, P. Gkoupidenis, *MRS Bulletin* **2020**, *45*, 631.
- [219] F. Torricelli, D. Z. Adrahtas, Z. Bao, M. Berggren, F. Biscarini, A. Bonfiglio, C. A. Bortolotti, C. D. Frisbie, E. Macchia, G. G. Malliaras, I. McCulloch, M. Moser, T.-Q. Nguyen, R. M. Owens, A. Salleo, A. Spanu, L. Torsi, *Nat Rev Methods Primers* **2021**, *1*, 1.
- [220] H. Yuan, H. Shimotani, A. Tsukazaki, A. Ohtomo, M. Kawasaki, Y. Iwasa, *J. Am. Chem. Soc.* **2010**, *132*, 6672.
- [221] J.-T. Yang, C. Ge, J.-Y. Du, H.-Y. Huang, M. He, C. Wang, H.-B. Lu, G.-Z. Yang, K.-J. Jin, *Advanced Materials* **2018**, *30*, 1801548.
- [222] M. T. Sharbati, Y. Du, J. Torres, N. D. Ardolino, M. Yun, F. Xiong, *Advanced Materials* **2018**, *30*, 1802353.
- [223] J. Rivnay, P. Leleux, M. Ferro, M. Sessolo, A. Williamson, D. A. Koutsouras, D. Khodagholy, M. Ramuz, X. Strakosas, R. M. Owens, C. Benar, J.-M. Badier, C. Bernard, G. G. Malliaras, *Sci Adv* **2015**, *1*, e1400251.
- [224] P. Gkoupidenis, N. Schaefer, X. Strakosas, J. A. Fairfield, G. G. Malliaras, *Appl. Phys. Lett.* **2015**, *107*, 263302.
- [225] P. Gkoupidenis, S. Rezaei-Mazinani, C. M. Proctor, E. Ismailova, G. G. Malliaras, *AIP Advances* **2016**, *6*, 111307.
- [226] P. Gkoupidenis, D. A. Koutsouras, G. G. Malliaras, *Nat Commun* **2017**, *8*, 15448.
- [227] S. Desbief, M. di Lauro, S. Casalini, D. Guerin, S. Tortorella, M. Barbalinardo, A. Kyndiah, M. Murgia, T. Cramer, F. Biscarini, D. Vuillaume, *Organic Electronics* **2016**, *38*, 21.
- [228] C. Qian, J. Sun, L. Kong, G. Gou, J. Yang, J. He, Y. Gao, Q. Wan, *ACS Appl. Mater. Interfaces* **2016**, *8*, 26169.
- [229] B. D. Paulsen, R. Wu, C. J. Takacs, H.-G. Steinrück, J. Strzalka, Q. Zhang, M. F. Toney, J. Rivnay, *Advanced Materials* **2020**, *32*, 2003404.

- [230] J. Rivnay, S. Inal, B. A. Collins, M. Sessolo, E. Stavrinidou, X. Strakosas, C. Tassone, D. M. Delongchamp, G. G. Malliaras, *Nat Commun* **2016**, *7*, 11287.
- [231] A. Savva, S. Wustoni, S. Inal, *J. Mater. Chem. C* **2018**, *6*, 12023.
- [232] P. Gkoupidenis, N. Schaefer, B. Garlan, G. G. Malliaras, *Advanced Materials* **2015**, *27*, 7176.
- [233] A. V. Marquez, N. McEvoy, A. Pakdel, *Molecules* **2020**, *25*, 5288.
- [234] H. Ling, D. A. Koutsouras, S. Kazemzadeh, Y. van de Burgt, F. Yan, P. Gkoupidenis, *Applied Physics Reviews* **2020**, *7*, 011307.
- [235] S. T. Keene, A. Melianas, Y. van de Burgt, A. Salleo, *Advanced Electronic Materials* **2019**, *5*, 1800686.
- [236] X. Ji, B. D. Paulsen, G. K. K. Chik, R. Wu, Y. Yin, P. K. L. Chan, J. Rivnay, *Nat Commun* **2021**, *12*, 2480.
- [237] B. Winther-Jensen, B. Kolodziejczyk, O. Winther-Jensen, *APL Materials* **2015**, *3*, 014903.
- [238] T. D. Nguyen, T. Q. Trung, Y. Lee, N.-E. Lee, *Advanced Engineering Materials* **n.d.**, *n/a*, 2100918.
- [239] T. P. A. van der Pol, S. T. Keene, B. W. H. Saes, S. C. J. Meskers, A. Salleo, Y. van de Burgt, R. A. J. Janssen, *J. Phys. Chem. C* **2019**, *123*, 24328.
- [240] S. T. Keene, T. P. A. van der Pol, D. Zakhidov, C. H. L. Weijtens, R. A. J. Janssen, A. Salleo, Y. van de Burgt, *Advanced Materials* **2020**, *32*, 2000270.
- [241] J. Y. Gerasimov, R. Gabrielsson, R. Forchheimer, E. Stavrinidou, D. T. Simon, M. Berggren, S. Fabiano, *Advanced Science* **2019**, *6*, 1801339.
- [242] M. Giordani, M. Sensi, M. Berto, M. D. Lauro, C. Bortolotti, H. L. Gomes, M. Zoli, F. Zerbetto, L. Fadiga, F. Biscarini, **2020**, DOI 10.1002/adfm.202070187.
- [243] E. Juzekaeva, A. Nasretdinov, S. Battistoni, T. Berzina, S. Iannotta, R. Khazipov, V. Erokhin, M. Mukhtarov, *Advanced Materials Technologies* **2019**, *4*, 1800350.
- [244] S. Y. Yeung, X. Gu, C. M. Tsang, S. W. Tsao, I. Hsing, *Sensors and Actuators A: Physical* **2019**, *287*, 185.
- [245] L. H. Jimison, S. A. Tria, D. Khodagholy, M. Gurfinkel, E. Lanzarini, A. Hama, G. G. Malliaras, R. M. Owens, *Adv Mater* **2012**, *24*, 5919.
- [246] M. Sessolo, D. Khodagholy, J. Rivnay, F. Maddalena, M. Gleyzes, E. Steidl, B. Buisson, G. G. Malliaras, *Adv Mater* **2013**, *25*, 2135.
- [247] O. P. Dimitriev, D. A. Grinko, Yu. V. Noskov, N. A. Ogurtsov, A. A. Pud, *Synthetic Metals* **2009**, *159*, 2237.
- [248] S. Zhang, P. Kumar, A. S. Nouas, L. Fontaine, H. Tang, F. Cicoira, *APL Materials* **2015**, *3*, 014911.

- [249] A. Håkansson, S. Han, S. Wang, J. Lu, S. Braun, M. Fahlman, M. Berggren, X. Crispin, S. Fabiano, *Journal of Polymer Science Part B: Polymer Physics* **2017**, *55*, 814.
- [250] N. Elgrishi, K. J. Rountree, B. D. McCarthy, E. S. Rountree, T. T. Eisenhart, J. L. Dempsey, *J. Chem. Educ.* **2018**, *95*, 197.
- [251] R. S, V. C, D. C. D, W. Aw, L. L, R. C, C. M, A. G, V. F, M. R, C. M, M. C, R. Ba, C. Gu, M. R, *Scientific reports* **2013**, *3*, DOI 10.1038/srep01395.
- [252] J. Khoshnoodi, V. Pedchenko, B. Hudson, *Microsc Res Tech* **2008**, *71*, 357.
- [253] D. Mazia, G. Schatten, W. Sale, *J Cell Biol* **1975**, *66*, 198.
- [254] F. Santoro, W. Zhao, L.-M. Joubert, L. Duan, J. Schnitker, Y. van de Burgt, H.-Y. Lou, B. Liu, A. Salleo, L. Cui, Y. Cui, B. Cui, *ACS Nano* **2017**, *11*, 8320.
- [255] X. Li, L. Matino, W. Zhang, L. Klausen, A. F. McGuire, C. Lubrano, W. Zhao, F. Santoro, B. Cui, *Nat Protoc* **2019**, *14*, 1772.
- [256] F. Santoro, E. Neumann, G. Panaitov, A. Offenhäusser, *Microelectron. Eng.* **2014**, *124*, 17.
- [257] M. B. M. Meddens, S. de Keijzer, A. Cambi, in *Fluorescence Microscopy* (Eds.: A. Cornea, P.M. Conn), Academic Press, Boston, **2014**, pp. 49–63.
- [258] D. M. Soumpasis, *Biophys J* **1983**, *41*, 95.
- [259] O. Marti, B. Drake, P. K. Hansma, *Appl. Phys. Lett.* **1987**, *51*, 484.
- [260] J. Jass, T. Tjärnhage, G. Puu, *Biophys J* **2000**, *79*, 3153.
- [261] I. Reviakine, A. Brisson, *Langmuir* **2000**, *16*, 1806.
- [262] E. P. Randviir, C. E. Banks, *Anal. Methods* **2013**, *5*, 1098.
- [263] E. Primiceri, M. S. Chiriaco, E. D’Amone, E. Urso, R. E. Ionescu, A. Rizzello, M. Maffia, R. Cingolani, R. Rinaldi, G. Maruccio, *Biosens Bioelectron* **2010**, *25*, 2711.
- [264] F. Hempel, J. K. Y. Law, T. C. Nguyen, R. Lanche, A. Susloparova, X. T. Vu, S. Ingebrandt, *Biosens Bioelectron* **2021**, *180*, 113101.
- [265] T. K. Bera, J. Nagaraju, G. Lubineau, *J. Vis.* **2016**, *19*, 691.
- [266] J. Rivnay, S. Inal, A. Salleo, R. M. Owens, M. Berggren, G. G. Malliaras, *Nat Rev Mater* **2018**, *3*, 1.
- [267] S. T. Keene, C. Lubrano, S. Kazemzadeh, A. Melianas, Y. Tuchman, G. Polino, P. Scognamiglio, L. Cinà, A. Salleo, Y. van de Burgt, F. Santoro, *Nat. Mater.* **2020**, *19*, 969.
- [268] T. Łuczak, *Electroanalysis* **2008**, *20*, 1639.
- [269] I. Gualandi, D. Tonelli, F. Mariani, E. Scavetta, M. Marzocchi, B. Fraboni, *Sci Rep* **2016**, *6*, 35419.
- [270] I. Gualandi, M. Marzocchi, E. Scavetta, M. Calienni, A. Bonfiglio, B. Fraboni, *J. Mater. Chem. B* **2015**, *3*, 6753.

- [271] V. Ball, *Frontiers in Bioengineering and Biotechnology* **2018**, *6*.
- [272] B. Wiatrak, A. Kubis-Kubiak, A. Piwowar, E. Barg, *Cells* **2020**, *9*, E958.
- [273] R. H. S. Westerink, A. G. Ewing, *Acta Physiol (Oxf)* **2008**, *192*, 273.
- [274] E. G. Gray, in *Progress in Brain Research* (Eds.: K. Akert, P.G. Waser), Elsevier, **1969**, pp. 141–155.
- [275] S. T. Larsen, R. Taboryski, *Analyst* **2012**, *137*, 5057.
- [276] Y.-S. Hsiao, C.-C. Lin, H.-J. Hsieh, S.-M. Tsai, C.-W. Kuo, C.-W. Chu, P. Chen, *Lab Chip* **2011**, *11*, 3674.
- [277] R. M. Wightman, C. L. Haynes, *Nat Neurosci* **2004**, *7*, 321.
- [278] B. Winther-Jensen, O. Winther-Jensen, M. Forsyth, D. R. Macfarlane, *Science* **2008**, *321*, 671.
- [279] C. N. J. Meunier, P. Chameau, P. M. Fossier, *Frontiers in Synaptic Neuroscience* **2017**, *9*.
- [280] A. A. Alabi, R. W. Tsien, *Cold Spring Harb Perspect Biol* **2012**, *4*, a013680.
- [281] K. D. Kozminski, D. A. Gutman, V. Davila, D. Sulzer, A. G. Ewing, *Anal Chem* **1998**, *70*, 3123.
- [282] W. Macias, R. Carlson, A. Rajadhyaksha, A. Barczak, C. Konradi, *Brain Res* **2001**, *890*, 222.
- [283] R. F. Vreeland, C. W. Atcherley, W. S. Russell, J. Y. Xie, D. Lu, N. D. Laude, F. Porreca, M. L. Heien, *Anal. Chem.* **2015**, *87*, 2600.
- [284] H. Tang, P. Lin, H. L. W. Chan, F. Yan, *Biosensors and Bioelectronics* **2011**, *26*, 4559.
- [285] R. A. Picca, K. Manoli, E. Macchia, L. Sarcina, C. Di Franco, N. Cioffi, D. Blasi, R. Österbacka, F. Torricelli, G. Scamarcio, L. Torsi, *Advanced Functional Materials* **2020**, *30*, 1904513.
- [286] C. Lubrano, U. Bruno, C. Ausilio, F. Santoro, *ADV MATER* **n.d.**
- [287] J. T. Friedlein, R. R. McLeod, J. Rivnay, *Organic Electronics* **2018**, *63*, 398.
- [288] **N.d.**
- [289] R. Wu, M. Matta, B. D. Paulsen, J. Rivnay, *Chem. Rev.* **2022**, DOI 10.1021/acs.chemrev.1c00597.
- [290] J. E. McCarthy, C. A. Hanley, L. J. Brennan, V. G. Lambertini, Y. K. Gun'ko, *J. Mater. Chem. C* **2013**, *2*, 764.
- [291] M. Tanaka, E. Sackmann, *Nature* **2005**, *437*, 656.
- [292] X. Crispin, F. L. E. Jakobsson, A. Crispin, P. C. M. Grim, P. Andersson, A. Volodin, C. van Haesendonck, M. Van der Auweraer, W. R. Salaneck, M. Berggren, *Chem. Mater.* **2006**, *18*, 4354.
- [293] L. Ouyang, C. Musumeci, M. J. Jafari, T. Ederth, O. Inganäs, *ACS Appl Mater Interfaces* **2015**, *7*, 19764.
- [294] R. Tero, *Materials (Basel)* **2012**, *5*, 2658.
- [295] C. Henley, **2021**.
- [296] G. Inzelt, G. G. Láng, in *Electropolymerization*, John Wiley & Sons, Ltd, **2010**, pp. 51–76.
- [297] G. Ertürk, B. Mattiasson, *Sensors* **2017**, *17*, 390.



## List of Publications

### Peer-reviewed articles (\*co-first author)

- “Supported lipid bilayers coupled to organic neuromorphic devices modulate short-term plasticity in biomimetic synapses”, Lubrano, C., Bruno, U., Ausilio, C., Santoro, F., *Advanced Materials*, **2022**, submitted.
- “Advances in cell-conductive polymer biointerfaces and role of the plasma membrane”, Mariano, A., Lubrano, C.\*, Bruno, U., Ausilio, C., Dinger, N., Santoro, F., *Chemical Reviews* **2021**.
- “Altered heparan sulfate metabolism during development triggers dopamine-dependent autistic-behaviours in models of lysosomal storage disorders”, De Risi, M., Tufano, M., Alvino, F., Ferraro, M., Torromino, G., Gigante, Y., Monfregola, J., Marrocco, E., Pulcrano, S., Tunisi, L., Lubrano, C., Papy-Garcia, D., Tuchman, Y., Salleo, A., Santoro, F., Bellenchi, G., Cristino, L., Ballabio, A., Fraldi, A., De Leonibus, E., *Nature Communications* **2021**, accepted.
- “New Frontiers for Selective Biosensing with Biomembrane-Based Organic Transistors”, Lubrano, C., Matrone, G. M., Iaconis, G., Santoro, F., *ACS Nano* **2020**, 14, 10, 12271–12280.
- “Towards biomimetic electronics that emulate cells”, Lubrano, C., Matrone, G. M., Forro, C., Jahed, Z., Offenhausser, A., Salleo, A., Cui, B., Santoro, F., *MRS Communication*, **2020**.
- “A biohybrid synapse with neurotransmitter-mediated plasticity”, Keene, S. T., Lubrano, C.\*, Kazemzadeh, S., Melianas, A., Tuchman, Y., Polino, G., Scognamiglio, P., Cinà, L., Salleo, A., van de Burgt, Y., Santoro, F., *Nature Materials*, **2020**.
- “A nanostructure platform for live-cell manipulation of membrane curvature”, Li, X., Martino, L., Zhang, W., Klausen, L., McGuire, A. F., Lubrano, C., Zhao, W., Santoro, F., Cui, B., *Nature Protocols*, **2019**.
- “Cells Adhering to 3D Vertical Nanostructures: Cell Membrane Reshaping without Stable Internalization”, Dipalo M., McGuire, A. F., Lou, H., Caprettini, V., Melle, G., Bruno, G., Lubrano, C., Martino, L., Li, X., De Angelis, F., Cui, B., Santoro, F., *Nano Letters*, **2018**.

**Annex A**

Equipment			
Item	Specification	Company	Catalog number
Arkeo		Cicci research	
Autolab PGSTAT302N		Metrohm	
Axio Observer Z1 Zeiss	Widefield fluorescence	Zeiss	
Bruker Dimension Icon microscope		Bruker	
Countess II Automated Cell Counter		Thermo Fisher Scientific	A27977
Dual beam microscope (SEM/FIB)	Helios Nanolab 600i and 650	Thermo Fisher Scientific	
Leica TCS SP5 Zeiss	gated with STED microscope	Zeiss	
Microfluidic pumping system		Cicci research	PR2008-0199
Mini-Extruder		Sigma Aldrich	610000-1EA
Scanning electron microscopy (SEM)	ULTRAPLUSS ZEISS field emission fun (FEG)	ZEISS	
Zeiss Axio Imager Vario	upright microscope	Zeiss	

**Annex B**

Chemicals			
Item	Specification	Company	Catalog number
1,2-Dihexadecanoyl-sn-Glycero-3-Phosphoethanolamine, Triethylammonium Salt (Texas Red DHPE)		Life Technologies	T1395MP
2-Oleoyl-1-palmitoyl-sn-glycero-3-phosphocholine		Sigma Aldrich	42773-100MG
2-propanol		Sigma Aldrich	33539-2.5L-M
3-glycidyloxypropyl)trimethoxysilane		Sigma Aldrich	440167-100ML
4-Dodecylbenzenesulfonic acid		Sigma Aldrich	44198-250ML
Acetone		Merck Life Science	32201-2.5L-M
Alexa Fluor 488	Anti-mouse, 2 mg/mL	Thermo Fisher Scientific	A11029
Bovine Serum Albumin BSA		Euroclone SPA	CHB3057401
Calcein-AM		Sigma Aldrich	17783
Collagen-IV from human placenta		Sigma Aldrich	C5533-5MG
Dopamine hydrochloride		Sigma Aldrich	H8502
Dopamine monoclonal antibody		Thermo Fisher Scientific	MA1-26966
Dulbecco's Modified Eagle's Medium		Sigma Aldrich	D6546
Ethanol		Sigma Aldrich	24105-2.5L-M
Ethylen glycol		Sigma Aldrich	102466-1L-M
Fetal Bovine Serum		Sigma Aldrich	F7524
Glass coverslips	12 mm diameter	Thermo Scientific	11856933
Glass coverslips	25x25 mm square	Thermo Scientific	13246778
Gluteraldehyde		Società Italiana Chimici	16220
Hoechst	10 mg/mL	Thermo Fisher Scientific	H3570
L-glutamine	200 mM	Sigma Aldrich	G8541
N-2-hydroxyethylpiperazine-N-2-ethane sulfonic acid (HEPES)	1 M	Life Technologies	15630056
Osmium tetroxide		Società Italiana Chimici	19190
Paraformaldehyde	16 % in aqueous solution	Società Italiana Chimici	15710
Penicillin-Stroptomycin	10,000 units penicillin and 10 mg streptomycin/mL	Sigma Aldrich	P4333
Phalloidin-X 647 conjugated dyes		Thermo Fisher Scientific	A22287
Phosphate Buffer Saline		Sigma Aldrich	D8537
poly(3,4-ethylenedioxythiophene) polystyrene sulfonate		Heraeus	81076212
Polycarbonate membranes	0.1µm pore, 19 mm diameter	Sigma Aldrich	610005-1EA
Poly-L-lysine	0.1% (w/v) H <sub>2</sub> O	Sigma Aldrich	P8920
Polymethylmethacrylate	PMMA 950 A4	MicroChem	
Potassium chloride		Sigma Aldrich	P3911-500G
Potassium ferrocyanide		Società Italiana Chimici	25102-20
Propidium iodide		Thermo Fisher Scientific	P1304MP
Resin		Società Italiana Chimici	14300
Silver conductive paste		RS component	1863593
Sodium cacodylate buffer		Società Italiana Chimici	11652
Sylgard 184		Farnell	101697
Tannic acid		Sigma Aldrich	403040

Interactive Biohybrid Synapses – Claudia Lubrano, M.Sc.

Thiocarbohydrazide (TCH)		Società Italiana Chimici	21900
Tris(hydroxymethyl)aminomethane buffer	100 mM, pH 7.4	Sigma Aldrich	648315-100ML
Trypsin-EDTA	2.5 g porcine trypsin and 0.2 g EDTA	Sigma Aldrich	T4049-100ML
Tryton-X		Sigma Aldrich	T9284-1L

## Annex C

Pulse conductance variation.

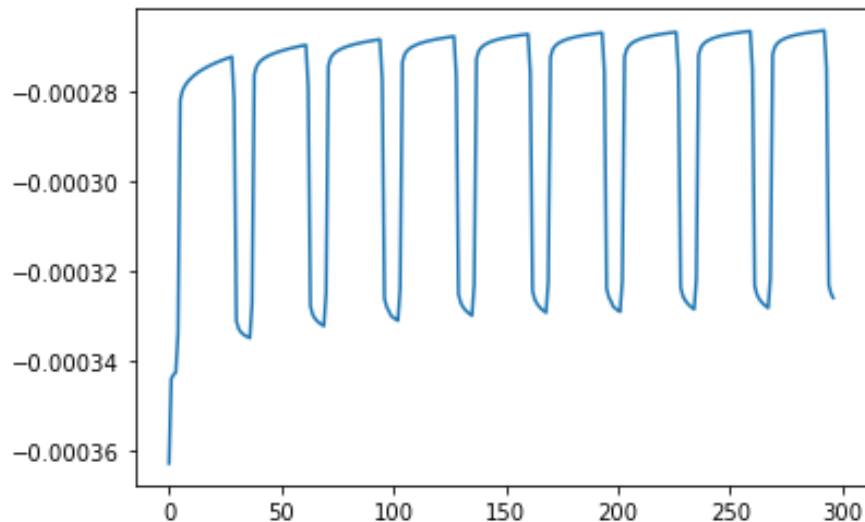
```
import numpy as np
import matplotlib.pyplot as plt
%matplotlib inline
import pandas as pd
import matplotlib.pyplot as plt
import numpy as np
%matplotlib inline

# Import all the libraries
import os
import numpy as np
import numpy as np
import matplotlib.pyplot as plt

# Load data/

path_raw = 'may/2021_05_18/transistor/planar/tau
exp/Z11_planar_PD=3tau_re3/Pulsed_Transistor/'
raw_data = sorted([x for x in os.listdir(path_raw) if x.endswith('.txt')])
file_index = 0
data=pd.read_csv(path_raw+raw_data[0], sep='\t')
raw_data[0]

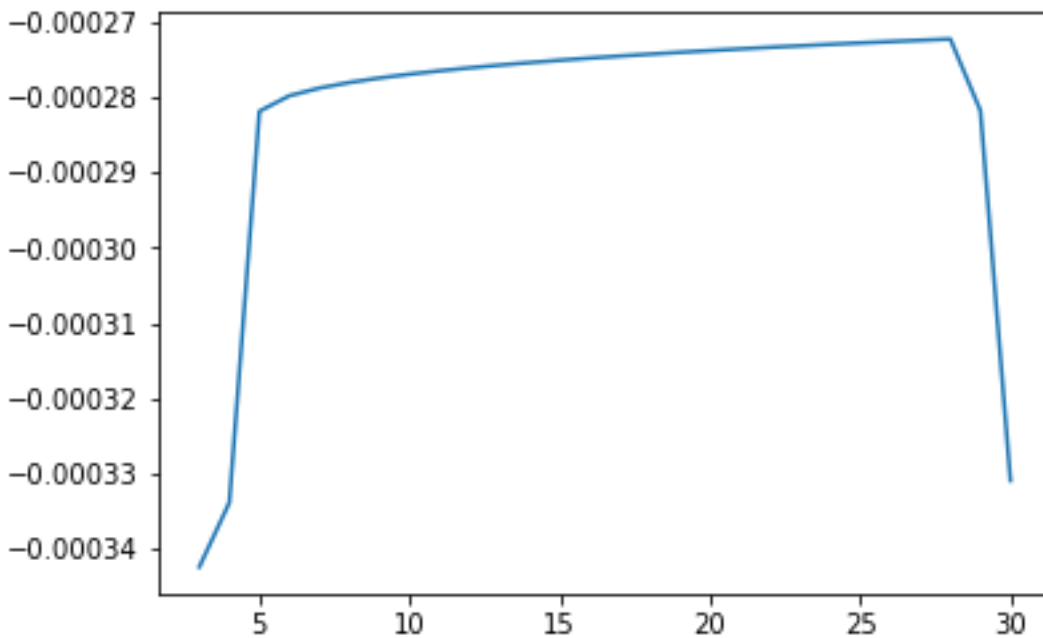
# Plot data/
v_ga = data['I Channel (A)']
plt.plot(v_ga)
```



```
# cut single pulse → first pulse
```

```
plt.plot(v_ga[3:37])
```

```
a=3;  
b=37;
```



```
# calculation of channel current variation
```

```
t=data.keys()[0]
```

```
ich=data.keys()[4]
```

```
time=np.asarray(data[t])
```

```
I_channel=np.asarray(data[ich])
```

```
I_channel[a]/1e-6
```

```
I_channel[b]/1e-6
```

```
# delta channel
```

```
delta_ch = I_channel[b]-I_channel[a]
```

```
delta_ch/1e-6
```

## Annex D

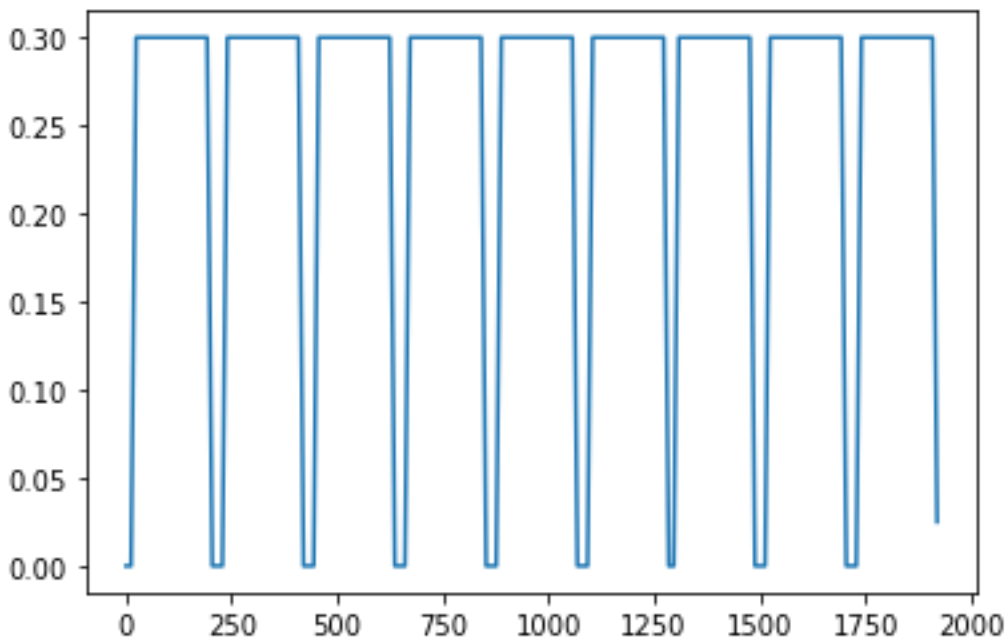
Gate current integration.

```
import numpy as np
import matplotlib.pyplot as plt
%matplotlib inline
import pandas as pd
import matplotlib.pyplot as plt
import numpy as np
%matplotlib inline

# Import all the libraries
import os
import numpy as np
import numpy as np
import matplotlib.pyplot as plt

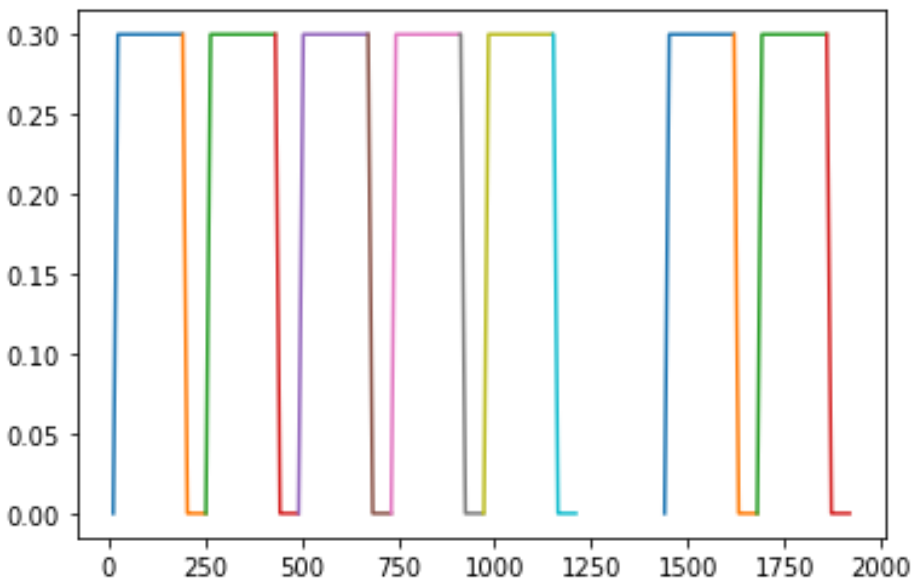
# Load data
path_raw = 'File name/'
raw_data = sorted([x for x in os.listdir(path_raw) if
x.endswith('resampled.txt')])
file_index = 0
data=pd.read_csv(path_raw+raw_data[file_index], sep='\t')
raw_data

v_ga = data['V gate (V)']
plt.plot(v_ga)
```



Interactive Biohybrid Synapses – Claudia Lubrano, M.Sc.

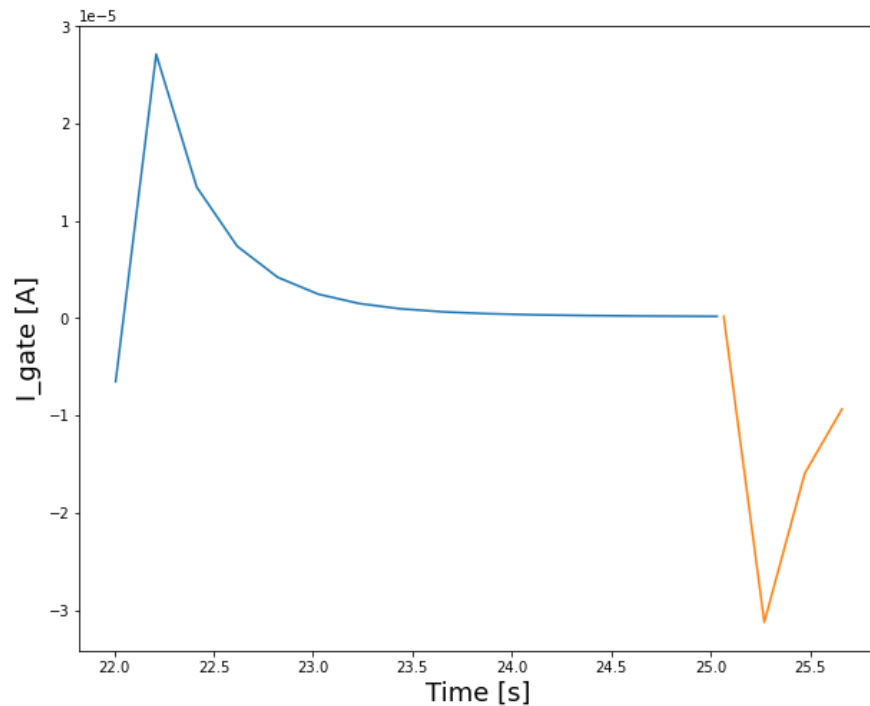
```
#plt.plot(v_ga[0:3000])  
  
plt.plot(v_ga[12:191])  
plt.plot(v_ga[192:228])  
  
plt.plot(v_ga[228:407])  
plt.plot(v_ga[408:444])  
  
plt.plot(v_ga[444:623])  
plt.plot(v_ga[624:660])  
  
plt.plot(v_ga[660:839])  
plt.plot(v_ga[840:876])  
  
plt.plot(v_ga[876:1055])  
plt.plot(v_ga[1056:1092])  
  
#plt.plot(v_ga[1092:1271])  
#plt.plot(v_ga[1272:1296])  
  
plt.plot(v_ga[1296:1475])  
plt.plot(v_ga[1476:1512])  
  
plt.plot(v_ga[1512:1691])  
plt.plot(v_ga[1692:1728])  
  
a = 1296  
b = 1475  
c = 1476  
d = 1512
```



```
t=data.keys()[0]
iG=data.keys()[2]

time=np.asarray(data[t])
I_gate=np.asarray(data[iG])

plt.figure(figsize=(10,8))
#plt.plot(time,I_gate, '-')
plt.plot(time[a:b],I_gate[a:b], '-')
plt.plot(time[c:d],I_gate[c:d], '-')
plt.xlabel('Time [s]',fontSize=18)
plt.ylabel('I_gate [A]',fontSize=18)
plt.title('')
```



```
# gate current integration with simpson method
from scipy.integrate import simps

sum_car = simps(I_gate[a:b], time[a:b])
sum_scar = simps(I_gate[c:d], time[c:d])

sum_car/1e-6
sum_scar/1e-6
diff = sum_car + sum_scar
diff/1e-6
```

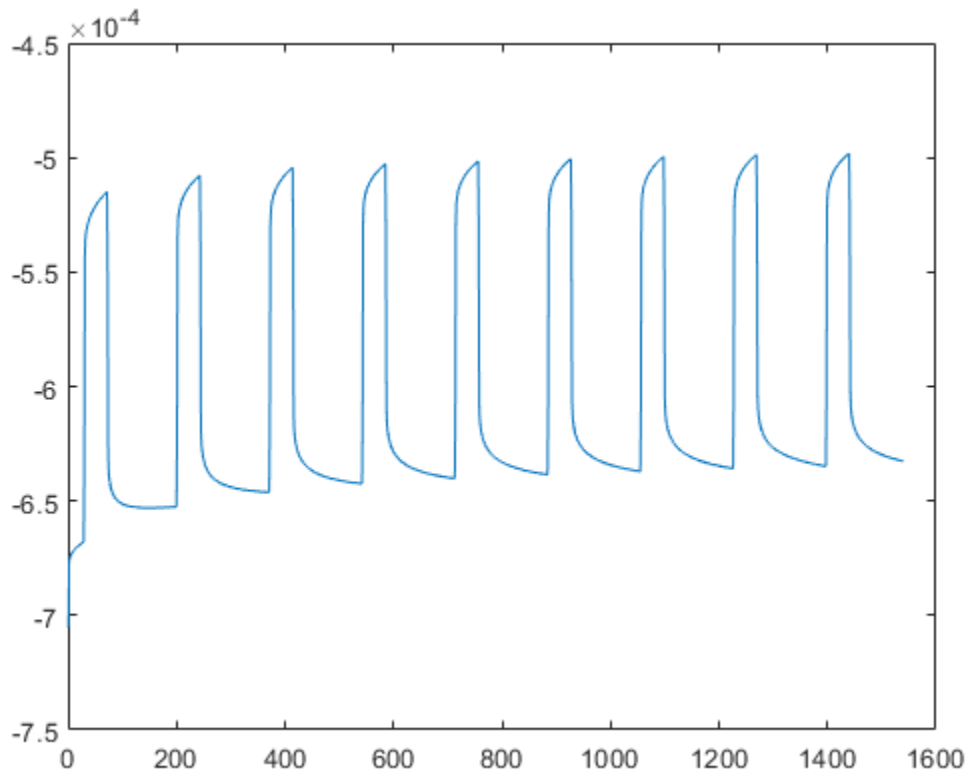


## Annex E

Computation of time response of OECT.

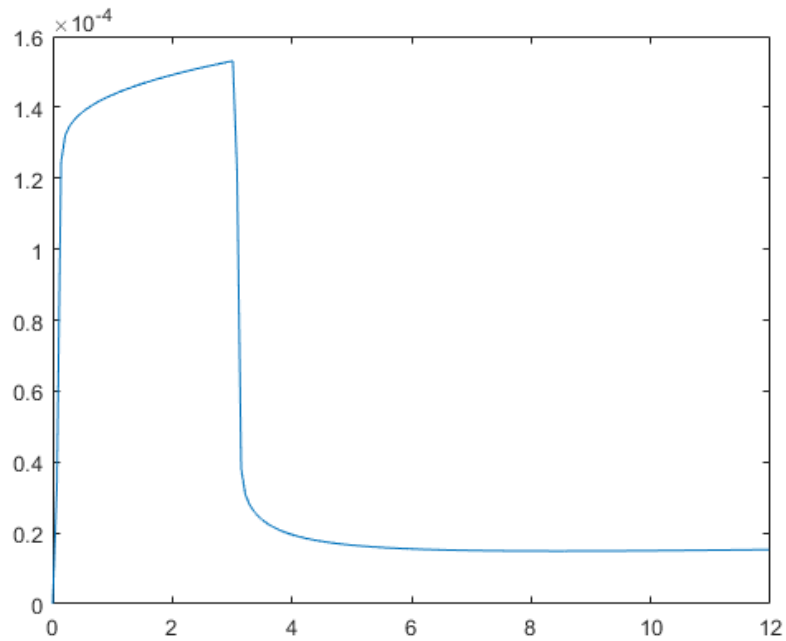
### Load Data

```
%Load data
data = load('File name.txt');
% Plot channel current → Time (s)      V gate (V)      I gate (A)      V Channel (V)      I
Channel (A)
time = data(:,1);
Vgat = data(:,2);
Igat = data(:,3);
Vcha = data(:,4);
Icha = data(:,5);
plot(Icha)
```



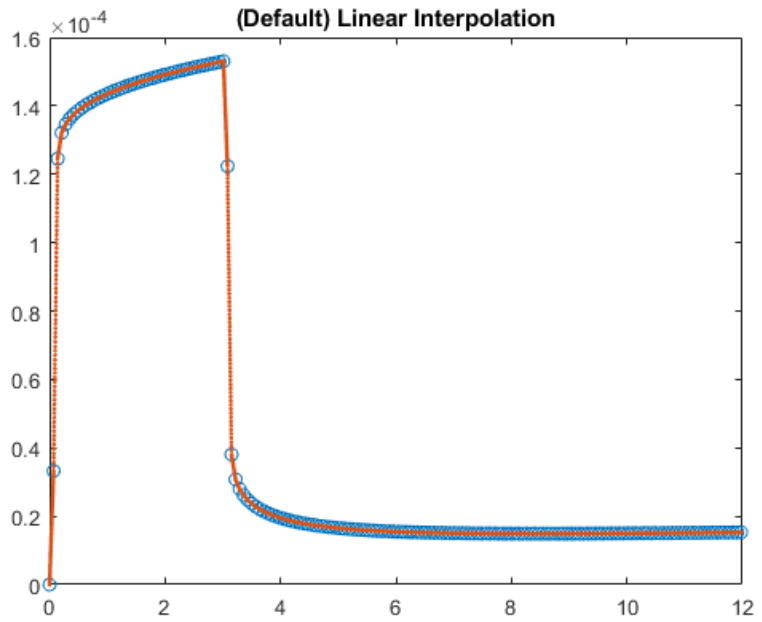
## Cut Data

```
t_cut = time(29:200);  
t_cut = t_cut - t_cut(1);  
i_cut = Icha(29:200);  
i_cut = i_cut - i_cut(1);  
plot(t_cut, i_cut)
```



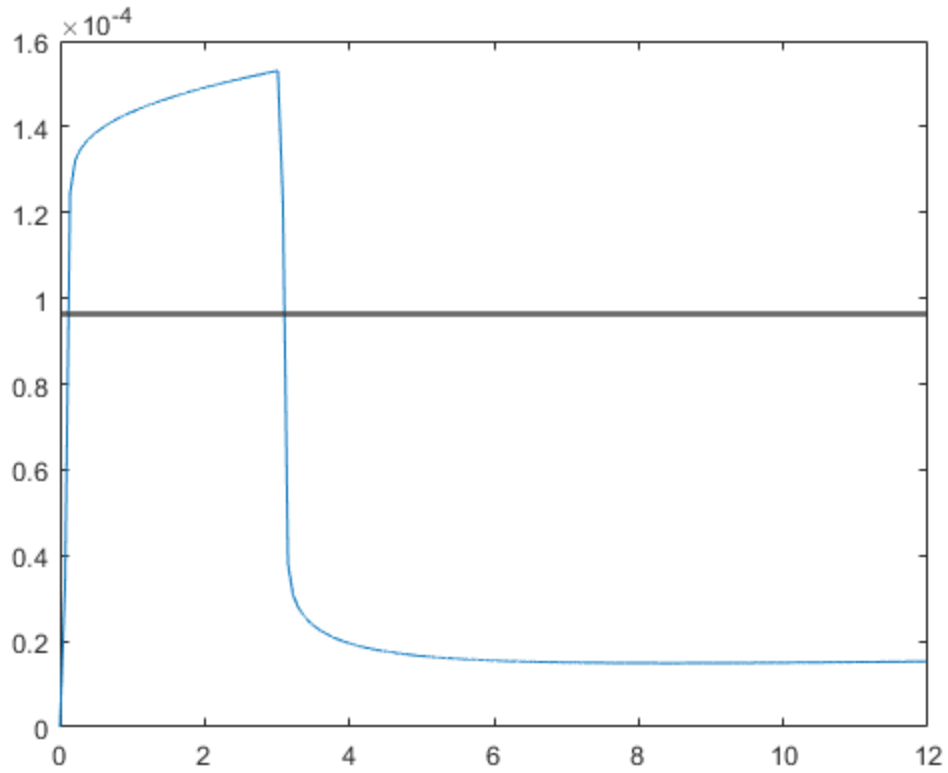
## Resample Data

```
t_res = t_cut(1):0.001:t_cut(end);  
  
I_res = interp1(t_cut, i_cut, t_res);  
  
plot(t_cut, i_cut, 'o', t_res, I_res, ':.');  
title('(Default) Linear Interpolation');
```



## Tau calculation

```
amp = 0.0001526
threshold = (amp/100)*63.2;
plot(t_res, I_res)
% plot(t_cut, i_cut)
hold on
yline(threshold, 'linewidth', 2)
idx = find(abs(I_res-threshold)<=(amp*10^-2));
tau = t_res(idx(1))
```



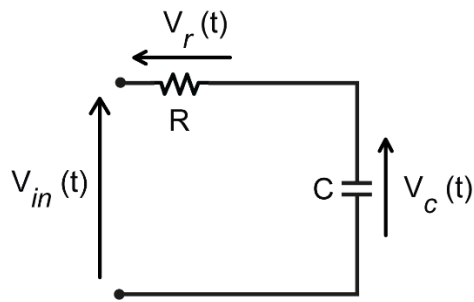
## Final data

```
% tau values
tau = 0.2060    % planar OECT
tau = 0.3520    % top OECT_
tau = 0.7550    % top OECT with SLB
tau = 0.6140    % planar OECT with SLB
```

## Annex F

### Analytical derivation of time constant $\tau$ .

To show the impact of the time constant on an RC circuit, it is possible to consider a resistance and a capacitance connected in series. Applying a voltage input  $V_{in}(t)$  as shown in the following figure, it is possible to compute the voltage fall on the resistance ( $V_r$ ) and on the capacitance ( $V_c$ ), through a voltage divider in the Laplace domain.



Called  $A$  the value of the applied voltage, it results:

$$V_{in}(s) = A * \frac{1}{s}$$

Accounting for:

$$V_r(s) = \frac{sRC}{1+sRC} * A * \frac{1}{s}$$

$$V_c(s) = \frac{1}{1+sRC} * A * \frac{1}{s}$$

By applying the inverse Laplace transform, it is possible to obtain the time domain expression of the above-mentioned voltages. In particular:

$$V_r(t) = A e^{-\frac{t}{RC}}$$

$$V_c(t) = A \left( 1 - e^{-\frac{t}{RC}} \right)$$

These equations are obtained in the case of the charge of the capacitance (*i.e.*,  $V_{in}(t) = 0$  when  $t = 0$ , and  $V_{in}(t) = A \forall t > 0$ ). The equations of the discharge phase can be obtained by switching the expression of the resistance and the capacitance.

Defined  $\tau = RC$ , when  $t = 1\tau$ :

$$V_c(t) = A(1 - e^{-1}) \rightarrow V_c(t) = A\left(1 - \frac{1}{e}\right) \rightarrow V_c(t) = A(0.632) \rightarrow V_c(t) = 63.2\%A$$

Meaning that, after a time interval of  $1\tau$ , the capacitor charges to about 63.2%. Repeating the same operations, with  $t = 5\tau$ :

$$V_c(t) = A(1 - e^{-5}) \rightarrow V_c(t) = A\left(1 - \frac{1}{e^5}\right) \rightarrow V_c(t) = A(0.993) \rightarrow V_c(t) = 99.3\%A$$

Meaning that the capacitance is fully charged after  $t = 5\tau$ .

## **Acknowledgements.**

Ed eccomi a ripensare a tutte le persone che si nascondono dietro questa tesi e questi anni di dottorato... che compito difficile!

Comincio dalla mia famiglia, la mia bellissima e meravigliosa famiglia, da mamma e papà che ci sono sempre stati e ci saranno sempre per me, con mamma sempre pronta ad ascoltare i racconti delle mie giornate in lab e tutti i miei esperimenti falliti e papà pronto con un abbraccio e un vassoio di delizie al limone per affogare i dispiaceri negli zuccheri. Non sarei ciò che sono senza di voi e anche se questo lavoro al momento mi porta lontano da voi so che sarete sempre i miei fan più accaniti. A Sara e Vincenzo, alle nostre pause merenda per consolarci prima di attaccare al PC, siete la mia spalla su cui poter contare sempre anche se ora viviamo in città diverse. Come diciamo sempre siamo una famiglia difficile da lasciare andare ma quelli di cui sento già la mancanza siete voi due.

Anna, Emi, Simo e Giulia, le mie AMICHE il regalo più bello che l'università potesse farmi, sapere di avervi ancora al mio fianco quasi 10 anni dopo mi rende la persona più fortunata del mondo e non smetterò mai di aspettare di aprire il nostro lab tutte insieme.

Viviana, ci supportiamo e sopportiamo da così tanti anni che forse è meglio non contarli ma invece quello che mi piace contare sono i nostri bagni al tramonto, aperitivi in spiaggia, le nostre passeggiate, i weekend fuori, i nostri viaggetti improvvisati dall'altra parte del mondo, non mi davi neanche il tempo di scriverti "Vivi ho una conferenza in California che dici mi raggiungi?" che avevi già preso le ferie e il primo volo disponibile.

Le mie conqui, Federica, Caterina, Virginia e Ottavia (coinquilina acquisita di casa Tarsia), il destino ha voluto che ci conoscessimo ad inizio pandemia e affrontassimo insieme la quarantena e così io ho trovato la mia famiglia acquisita con cui passare i weekend a cucinare l'impossibile, organizzare pasquetta in veranda e trascorrere le serate a fare immagini su illustrator. Siete state le migliori coinquiline che potessi desiderare e sapevo che al termine di una brutta giornata avrei sicuramente trovato qualcuna di voi già fuori in veranda con una birra in mano.

Paris, these years in IIT would have been very sad and lonely without you, your hugs, our lunch breaks, and your sweet messages on the desk, I'm so lucky to call you "my sister" and I can't wait to hug you again.

Amedeo sei arrivato così all'improvviso e inaspettatamente ma non sarei riuscita ad affrontare quest'ultimo anno senza di te, sei il mio posto sicuro e non vedo l'ora di scoprire cosa il futuro ha in serbo per noi.

Ed ora veniamo alla mia "famiglia" lavorativa.

I would like first of all to thank Scott and Setareh for being the best collaborators ever, I loved working with you guys having skype calls day and night and such tough work wouldn't have been so fun without you. I really hope that one day we will have the chance to work together again.

Tutta la mia Tissue-E family, cavolo questa sì che è difficile, non so da dove iniziare per ringraziarvi tutti uno per uno: credo che chiunque faccia questo lavoro sappia l'importanza di avere qualcuno con cui dividere le giornate di lab, con cui sfogarsi di fronte ad un esperimento fallito o urlare di gioia quando qualcosa che si è inseguito per tanto tempo finalmente riesce, e io non avrei potuto immaginare di avere qualcuno migliore di voi con cui condividere questi 4 anni. E in particolare Chiara, il mio dream team, sei stata il miglior braccio destro di sempre con cui dividere le bestemmie e le gioie (poche) dei nostri lipidini, e anche se so per certo che saremo un amazing dream team anche a distanza, una parte di me continuerà ad aspettare che tu la raggiunga in tedeschia; Anna, la mia co-author e co-baker, se siamo arrivate in fondo a quella review è stato solo perché eravamo insieme (e grazie ad Auron ovviamente che ha scritto buona parte del paper), e quando metterai su il tuo gruppo meeting free fammi uno squillo sarò già sul primo volo!

Francesca, che starà già pensando che mi sono dimenticata di lei, la verità è che mettere nero su bianco 4 anni insieme è davvero difficile e riduttivo; questa tesi rappresenta solo la punta dell'iceberg di cosa abbiamo fatto insieme e non so da dove iniziare per ringraziarti di tutto quello che hai fatto per me e mi hai dato in questi anni. Ecco forse comincio dal ringraziarti per la bellissima Tissue-E family che hai creato perché se siamo davvero diventati come e più di una famiglia è perché hai saputo sceglierci "con lo stampino" come dici sempre. Sai io non mi sono mai immaginata a fare qualcosa di diverso da questo lavoro ma le opportunità che mi hai dato tu in questi anni andavano ben oltre la mia immaginazione (mi hai portata a Stanford, STANFORD!!), hai saputo spingermi oltre i miei limiti restando al mio fianco e forse a volte ci vuole un po' per apprezzare tutto quello che fai per noi, ma se guardo indietro non vedo altro che tutto quello che mi hai dato (sì anche le conferenze per cui ti ho fatta dannare ogni volta) e voglio ringraziarti anche per avermi inserita nel progetto del Nature Materials perché non dimenticherò mai le notti passate con i ragazzi cercando di far quadrare quegli esperimenti e la gioia di quando è uscito il paper, mi sono sentita parte di qualcosa di grande e importante e ho sentito che davvero il nostro lavoro potrebbe fare la differenza per qualcuno un giorno. Mi hai sempre detto che dopo il dottorato dovevo andare via ma invece sono contenta di seguirti in tedeschia per una nuova avventura e penso che vorrò sentire i tuoi "not bad" ancora per un paio d'anni.